ASSESSING THE ORTHORECTIFICATION ACCURACY OF RPC SENSOR MODELS USING LIDAR TERRAIN SURFACE HEIGHTS

by

Roger O. Brown

A Thesis
Submitted to the
Graduate Faculty
of
George Mason University
in Partial Fulfillment of
The Requirements for the Degree
of
Master of Science
Geography and Geoinformation Science

Committee:

_____ Dr. Arie Croitoru, Thesis Director

_____ Dr. Matthew T. Rice, Committee Member

_____ Dr. Anthony Stefanidis, Committee Member

_____ Dr. Anthony Stefanidis, Department Chair

_____ Dr. Donna M. Fox, Associate Dean, Office for Student Affairs, College of Science

_____ Dr. Peggy Agouris, Dean, College of Science

Date: _____ Spring Semester 2017
George Mason University
Fairfax, VA

Assessing the Orthorectification Accuracy of RPC Sensor Models Using LiDAR Terrain Surface Heights

A Thesis submitted in partial fulfillment of the requirements for the degree of Master of Science at George Mason University

by

Roger O. Brown
Master of Science
Virginia Tech 1989

Director: Arie Croitoru, Professor
Department of Geography and Geoinformation Science

Spring Semester 2017
George Mason University
Fairfax, VA

Dedication

This is dedicated to my wife Robina plus our children Tyler, Alicia, and Adrian. Where they tolerated many absences from me throughout a continued education during my career of 35 years.

Acknowledgements

Thanks to the US Army Corps of Engineers (USACE) Engineer Research and Development Center (ERDC) Geospatial Research Laboratory (GRL) plus the George Mason University (GMU) for encouraging and subsidizing my graduate coursework. Thanks also toward my graduate committee of Drs. Arie Croitoru, Matthew Rice, and Anthony Stefanidis who supported this thesis. Special thanks toward the providers of the data for this study that included the Army Geospatial Center (AGC) Imagery Office for supplying the WorldView2 data and the Oregon State University for supplying the Oregon Department of Geology and Mineral Industries (DOGAMI) Oregon LiDAR Consortium (OLC) data. Thanks mostly to all colleagues and classmates that encouraged me throughout my continued education.

Table of Contents

Page

List of Tables vii

List of Figures viii

List of Equations x

List of Abbreviations & Symbols xi

ABSTRACT xii

1 CHAPTER ONE 1

1.1 Introduction 1
1.2 Hypothesis 5
1.1 Background 5
1.3 Current Technology 7
1.4 Study Purpose 10

2 CHAPTER TWO 12

2.1 Overview 12
2.2 LiDAR DEM & RPC Sensor Models 12
2.3 Orthorectification Process 20
2.4 Orthoimage Accuracy Assessment 30

3 CHAPTER THREE 32

3.1 Orthorectification Data & Methods 32
3.2 LiDAR Point Cloud 33
3.3 Constructing DEM Raster 37
3.4 Conducting Orthorectification 47

4 CHAPTER FOUR 49

4.1 Assessing Orthoimage Accuracy 49
4.2 Output Rendering Anomalies 49
4.3 Accuracy Assessment Results 54

5 CHAPTER FIVE 65
5.1 Conclusion 65
5.2 Limitations 67
5.3 Current Impacts 69
5.3.1 Relative Positional Inaccuracy Reduction 70
5.3.2 Orthoimage Feature Ghost Removal 70
5.4 Future Efforts 75
Appendix 77
A. Measured Orthoimage Examples 77
B. Input & Output Parameters 89
References 95

List of Tables

Page
Table 1: Point Cloud Input & Output Coordinate Systems..... 18
Table 2: Orthoimage Rooftop Offsets..... 57

List of Figures

Page
Figure 1: MSI Theme Map Orthorectification Process 10
Figure 2: Worldview2 MSI & LiDAR DEM 15
Figure 3: Converting Elevations NAVD 1988 (GRS80) To WGS 1984 19
Figure 4: Orthorectication Process Flowchart 25
Figure 5: University of Oregon Campus West Quadrangle 33
Figure 6: LiDAR Feature Points 34
Figure 7: Perspective View Aerial LiDAR Point Cloud 35
Figure 8: Terrain Height Elevation Discontinuities 36
Figure 9: LiDAR Dataset Properties 38
Figure 10: DEM Point Cloud Feature Extents 39
Figure 11: Finding Matched Dimensions For Output Orthoimage & Input DEM Raster 40
Figure 12: The MSI Orthoimage Where All Z Values Equal 126 meters 41
Figure 13: Raster & Fishnet Dataset Properties 43
Figure 14: (A) Image Of DEM Raster & (B) Orthoimage From Z=126 Meters 44
Figure 15:Converting Point Cloud To DEM Raster Of Maximum Z Values 45
Figure 16: Shifting LiDAR Elevations Between Vertical Datums 46
Figure 17: Orthorectification Input & Output Parameters 47
Figure 18: (A) Output Orthoimage & (B) Input DEM Raster 48
Figure 19: (A) Orthoimage Rooftop Ghost & (B) DEM Raster Z Values 51
Figure 20: Sensor LOS Occlusion & DEM Feature Ghosts 53
Figure 21: Original Unrectified MSI Building 55
Figure 22: Comparing (A) DEM Raster & (B) Output Orthoimage 56
Figure 23: Produced Orthoimage From Shifted DEM 58
Figure 24: (A) Orthoimage From Shifted DEM Compared To (B) Original Orthoimage 60
Figure 25: (A) New Orthoimage After Counterposed Shift Back To (B) DEM Raster 62
Figure 26:Matched Refined Orthophoto (Case A-K) &DEM Raster 64
Figure 27: MSI & LiDAR Data Spans 69
Figure 28: DEM Raster Cell XYZ Centroids Sorted By Descending Z Values 72
Figure 29: Comparing DEM & Orthoimage (Case A) 78
Figure 30: Comparing DEM & Orthoimage (Case B) 79
Figure 31: Comparing DEM & Orthoimage (Case C) 80
Figure 32: Comparing DEM & Orthoimage (Case D) 81
Figure 33: Comparing DEM & Orthoimage (Case E) 82
Figure 34: Comparing DEM & Orthoimage (Case F) 83
Figure 35: Comparing DEM & Orthoimage (Case G) 84

Figure 36: Comparing DEM & Orthoimage (Case H)..... 85
Figure 37: Comparing DEM & Orthoimage (Case I)..... 86
Figure 38: Comparing DEM & Orthoimage (Case J)..... 87
Figure 39: Comparing DEM & Orthoimage (Case K)..... 88
Figure 40: LiDAR Point Cloud Joined With DEM Lattice..... 90
Figure 41:Convert DEM Grid Lattice To Rectangle Centroids..... 91
Figure 42: DEM Horizontal Dimensions..... 92
Figure 43: Convert DEM Raster Z Values..... 93
Figure 44: Produce Orthoimage From WGS84 DEM Raster..... 94

List of Equations

Page
Equation 1: DEM to MSI Projection 21
Equation 2: $(x',y')_{MSI} = f(x,y,z)_{DEM}$ 22
Equation 3: Coordinates $(x,y,z)_{DEM}$ 23
Equation 4: Coordinates $(x',y')_{MSI}$ 23
Equation 5: Collinearity Perspective Projection 24
Equation 6: Orthoimage Produced From Coordinate List Sorted By Z Values 73

List of Abbreviations & Symbols

ACSM ..... American Congress of Surveying and Mapping
ASCE ..... American Society of Civil Engineers
ASPRS ..... American Society for Photogrammetry and Remote Sensing
CONUS ..... Continental United States
DEM ..... Digital Elevation Model
DSM ..... Digital Surface Model
DTM ..... Digital Terrain Model
DOGAMI ..... Oregon Department of Geodesy and Mineral Industries
ERDAS ..... Earth Resources Data Analysis System
ESRI ..... Environmental Sciences Research Institute
GIS ..... Geographic Information System
GPS ..... Global Positioning System
GRS80 ..... Geodetic Reference System 1980
GSD ..... Ground Sample Distance
HARN ..... High Accuracy Registration Network
LiDAR ..... Light Distance and Ranging
LAS ..... LiDAR Laser Data Format
LOS ..... Line-of-Sight
MSI ..... Multi-Spectral Imagery
NAD83 ..... North American Datum 1983
NAVD88 ..... North American Vertical Datum1988
NITF ..... National Imagery Transmission Format
NOAA ..... National Oceanic and Atmospheric Administration
OLC ..... Oregon LiDAR Consortium
RPC ..... Rational Polynomial Coefficients
STOMP ..... Spatial Thematic Observation Modeling Process
US ..... United States
WorldView2 ..... Commercial Satellite MSI

$\rightarrow$ ..... DEM to MSI Projection Transform
$[x,y,z]_{DEM}$ ..... DEM Coordinates
$[x',y',b_i]_{MSI}$ ..... MSI Coordinates
$[x,y,z,b_i]_{Ortho}$ ..... Orthoimage Coordinates
$(a_{ijk})_p(x^i)(y^j)(z^k)$ ..... Polynomial P Coefficient Showing xyz Exponents

ABSTRACT

ASSESSING THE ORTHORECTIFICATION ACCURACY OF RPC SENSOR MODELS USING LIDAR TERRAIN SURFACE HEIGHTS

Roger O. Brown

George Mason University, 2017

Thesis Director: Dr. Arie Croitoru

This thesis describes the orthorectification process for commercial satellite Worldview2 Multi-Spectral Imagery (MSI) with a Rational Polynomial Coefficient (RPC) sensor model by using a Digital Elevation Model (DEM) raster of terrain heights from Light Distance and Ranging (LiDAR) data. The orthorectification process is presented that uses a LiDAR DEM raster with Ground Sample Distance (GSD) that matches the nearly 0.5 meters nominal GSD of the panchromatic overall spectral brightness, and about 2 meters nominal GSD of each spectral band, for the pixel footprint of the Worldview2 unrectified MSI. It presents a process to encourage adding extra DEM layers such as slope and aspect into the MSI feature extraction process. This study tests a hypothesis to see if the orthorectification process produces adequate registration of the DEM and orthoimage for combined spectral and terrain reasoning, by measuring the offsets between the input DEM and the output orthoimage.

The accuracy assessment is directed within an urbanized landscape that contains numerous elevation discontinuities, where the vertical sidewalls of buildings cause cliffs within the terrain surface. Rendering anomalies of feature ghosts from the elevation discontinuities are described along with a suggested solution to the problem. A method also is presented that measures positional inaccuracy between conjugate features within the image of the terrain surface heights and within the initial orthoimage, and then it entails removal of the measured systematic error (shift) within a reproduced orthoimage. This study suggests or provides solutions to identified problems within conventional orthorectification processing regardless of the sensor model. This affirms the alternative hypothesis that the conventional orthorectification process can be adjusted to produce sufficient registration of the DEM and orthoimage for combined spectral and terrain reasoning, if the suggestions from this thesis are implemented.

CHAPTER ONE

1.1 Introduction

This chapter introduces how overhead aerial and satellite imagery can be corrected by removing its combined displacements plus geometric distortions through an "orthorectification" process that produces a graphically rectified "orthoimage" (sometimes it might be called something else with the "ortho" prefix and other suffixes). The orthoimage is a product "prepared from a perspective photograph" to remove "displacement of points caused by tilt, relief and central projection" that portrays terrain exposed by the Multi-Spectral Imagery (MSI) sensor within the coordinate system of a planimetric photomap for interpretation and analysis. Other terms such as "orthorectified MSI" and "orthorectifying MSI" or "orthorectification" (by itself as a noun, verb, or object within a sentence) are also used frequently (Campbell & Wynne, 2011, pp. 88-90, 130-153; ASCE, ACSM, ASPRS, 2011; Muehrcke, 1978, pp. 51-60).

Orthorectification is a complex process that requires (1) a Digital Elevation Model (DEM) that depicts the terrain surface heights and (2) a model for projective equations between the exposed terrain surface and the sensor image. It also requires integration of geographic information and image processing systems (Worboys & Duckham, 2004) to apply the sensor model for the projection of points between the DEM raster and the original unrectified (raw) MSI that passively records the energy reflected from the

illuminated terrain surface. The passive MSI sensor records energy reflected from the terrain surface illuminated by sunlight. The MSI sensor has shadows where sun angles cause poor illumination within the shaded area. But the active LiDAR sensor sends pulses of energy to the terrain surface, then it records the waveform of the pulse when it is reflected from the terrain surface back to the sensor. Both the LiDAR and MSI sensors cannot see some portions of the terrain surface, because the terrain surface itself might occlude or obstruct the sensor Line-of-Sight (LOS) before it gets to another spot with a lower elevation. This means that some portions of the terrain surface remain unexposed within the image regardless of the sensor type.

The DEM can be in the formats of a point cloud, raster, wireframes consisting of polygonal facets for terrain features such as buildings, and a Triangulated Irregular Network (TIN). The conventional orthorectification process requires a DEM raster, where the mixed DEM formats need to be combined and converted into singular uniform grid lattice of raster cells before the orthorectification process starts. The Digital Surface Model (DSM) is a DEM for drawing contours of the “bare” terrain surface without features or objects such as construction (buildings) or vegetation (trees and crops). The Digital Terrain Model (DTM) includes all features that form the surface of the terrain regardless of their formats. These models refer to a collection of points, lines, and polygonal facets. Where each point has XY positions in a horizontal coordinate system and with Z values of terrain heights in a vertical coordinate system (aerometrex, 2011).

The conventional orthorectification process uses a singular uniform DEM raster with the maximum Z value, placed at the centroid of each raster cell, to represent one or more

terrain heights that exist within the cell. The maximum Z value is chosen as the "highest hit" to depict the reflective terrain surface when more than one terrain surface height exists within a single cell of the DEM raster. The orthorectification process casts the brightness values, recorded by the MSI sensor while exposing the terrain, onto the DEM raster of maximum Z values that depicts the reflective terrain surface.

The orthorectification process requires a sensor model and a DEM with terrain heights. But other methods besides the orthorectification process might exist for relative positional adjustments between image and terrain data if a sensor model or DEM is unavailable to register, conflate, and rectify separate images or topographic data (Lewis, et al., 2010; Wang, et al., 2007; Stefanidis, et al., 2006; Chen, et al., 2003; Brown, 2000; Rice, 1998; Brown, 1995). This study only is concerned with assessing the accuracy of the orthorectification process, but future studies could compare the spatial accuracy results from the orthorectification process to other methods for matching the original unrectified MSI with the image of the DEM.

This study conducts the orthorectification process for commercial satellite WorldView2 MSI (Satellite Imaging Corporation, 2013; LANDinfo Worldwide Mapping LLC, n.d.) by using a DEM that has a uniform raster of terrain heights derived from the Light Distance and Ranging (LiDAR) point cloud. The DEM construction starts with a cloud of points within the LiDAR Laser (LAS) data format that measures terrain height at sharply defined maximums (spikes) of return intensity along the slant range of a waveform for each pulse from the LiDAR sensor (Brown, 2014, pp. 51-52; Toth & May, 2013; Pack, et al., 2012; Graham, 2012).

The Rational Polynomial Coefficient (RPC) sensor model is supplied along with the original unrectified MSI by whomever is providing the data. The utility of the RPC sensor is that it replaces the actual sensor model without revealing its interior and exterior orientations for proprietary or classification reasons, and it bypasses the costly development of a physical model for the sensor. The RPC sensor model expects a DEM raster of Z values for the terrain surface heights to produce an orthoimage. The next chapter describes the RPC sensor model with more detail. The results from conventional orthorectification also are described within later chapters in this study.

Elevation discontinuities occur when there is a large difference between the maximum and minimum elevations within any DEM raster cell, and when extra terrain surfaces might appear along the waveform of a LiDAR pulse. The magnitude and frequency of elevation discontinuities from cityscape terrain features with vertical facets (cliffs from sidewalls of buildings or other construction) is typically greater compared to what is found in natural terrain. This study uses the urbanized landscape, with a relatively high frequency and amplitude of elevation discontinuities compared to the natural terrain used within many past studies, that might increase inaccuracy from the orthorectification process during orthoimage accuracy assessment. The relative accuracy between the image of the input DEM raster compared to the output orthoimage will be assessed by this study, so this study will determine how well the DEM and orthoimage products become registered between themselves for combined spectral and terrain reasoning methods.

1.2 Hypothesis

This research tests the hypothesis that the "MSI orthorectification produces adequate registration of the input DEM raster with the output orthoimage that is sufficient for combined spectral and terrain reasoning." The evolving improvement of the spatial resolution for the LiDAR DEM and for the commercial satellite MSI also suggests that current orthorectification process and standards should be reviewed or altered, to reflect the evolving increased spatial precision and accuracy of the DEM and MSI data that is becoming available (Young, 2016). Some common expectations and current practices regarding the orthorectification process, that includes the existing utility of orthoimage products, might be revised after completing this study pending the accuracy assessment results for the orthorectification process.

1.1 Background

WorldView2 data has the best spatial and spectral resolution of current commercial satellite MSI (Ehlers, et al., 2009, pp. 727-731). The reasons for producing orthorimages are described throughout the literature for the current state of the art (Miller, 2013; Scarpace, 2013; Agouris, et al., 2004). Spots on the terrain surface from the DEM raster are projected into the MSI through the sensor model, where each DEM spot includes an estimated terrain height for each grid cell from the DEM raster during MSI orthorectification. This study therefore assesses the accuracy results from the orthorectification process that minimizes interpolation from the improved spatial resolution of the LiDAR DEM Ground Sample Distance (GSD), and from the improved nominal GSD for the pixel footprint from the input original unrectified MSI, within the

produced orthoimage. It also develops a new process where the input DEM raster and output orthoimage are aligned better to enhance both the accuracy assessment and the MSI feature extraction.

The DEM data is preprocessed by the ESRI ArcGIS product (ESRI, 2012) to prepare it for the MSI orthorectification process that is conducted by the ERDAS Imagine image processing system (DigitalGlobe, 2013; Earth Resources Data Analysis System, 2013; DigitalGlobe, n.d.). Then the spatial accuracy of the MSI orthorectification is assessed by using both products to measure or correct the apparent relative spatial inaccuracy between the image of the input DEM raster and the output orthoimage. Combined usage of these products throughout the entire orthorectification process allows you to leverage the vector processing power of GIS, and the raster processing power of the image processing system.[1]

The ESRI ArcGIS software converts a LiDAR point cloud into a DEM raster, despite the existence the highest terrain height from the first return within a DEM raster that already is provided as a standard product with the LiDAR data but with 3 feet GSD, compared to the 1.7 feet GSD that is used for this study. But the LiDAR DEM raster is in a different spatial reference of another XY and Z coordinate system compared to what is expected in the Worldview2 RPC sensor model. It also is highly unlikely that the LiDAR DEM raster of terrain heights is directly used to derive the RPC sensor model provided

[1] Using these geographic information and image processing products only reflects their availability for this study, but that cannot be construed as preferences to use these products employed in this study. A market survey to compare other products with the same functionality should be done elsewhere, because other companies maintain and distribute similar products.

with each MSI frame, which might contribute inaccuracy to the output orthoimage during the orthorectification process. The MSI and its RPC for the sensor model are provided without explaining how the coefficients were formed. This makes is difficult within the study to determine how the RPC sensor model contributes to orthoimage inaccuracy.

The pixels of conjugate features that can be found both on the image of the DEM raster for terrain heights and on the orthorectified MSI will be used to assess the output orthoimage accuracy. The LiDAR DEM and MSI data for this study includes urbanized landscapes (cityscapes) with many elevation discontinuities from abrupt changes in terrain height at the edges of rooftops for buildings and other structures, so the data is likely to cause pronounced error from interpolation for the accuracy assessment of the orthorectification process. These types of features with permanent construction also are better for assessing relative accuracy between the DEM and orthorectified MSI because other features may shift when there is a large time lag between the collection of the LiDAR DEM and the exposure of the same terrain by the MSI sensor. The MSI might expose moving or parked vehicles that are in different positions when the DEM is collected. Tree canopies also will change within the time lag between MSI exposure and DEM collection, say between seasons for leaves on or off, so that might adversely affect the accuracy assessment because horizontal and vertical positions of many features might change and shift during time lags between DEM collection and MSI exposure.

1.3 Current Technology

Current studies focus on directly using the LiDAR data by itself to describe the terrain shape including its slope for analysis such as landslide susceptibility, movement

and mobility, plus hydrology that includes drainage or shallow water mapping (Mahalingam, et al., 2016; Rodgers, 2015; Cleveland, 2015). Thematic maps describing the surface material from the MSI feature extraction might compliment the terrain analysis. The descriptions of the terrain shape from the LiDAR DEM also might compliment the direct extraction of features from the MSI.

There are mapping technologies that are ranked by their temporal currency of (1) tracking or crowdsourced data streams, (2) original rectified current MSI, and (3) compiled and authenticated topographic data. Orthoimage backdrops can provide a current, robust, and perhaps accurate backdrop within geographic information mapping applications. The reduction of positional inaccuracy within orthoimages themselves therefore has significant benefits for the most current tracking and crowdsourced data, and for less current topographic data. This because tracking and crowdsourced data might rely on accurate orthoimages for position validation and adjustment of reports coming from mobile collection devices with diminished location services (Rice, et al., 2016; Rice, et al., 2013). That means current accurately orthorectified MSI provides valuable spatial and temporal context for all features including actors and events to describe geographic behavior.

It is possible to perform the unsupervised classification within the original unrectified MSI to form a thematic image layer, then to conduct orthorectification of its thematic image from spectral feature extraction, to allow an ensuing Spatial Thematic Observation Modeling Process (STOMP), which compares feature classes within the thematic orthoimage and within the terrain surface descriptions derived from the DEM raster

(Homer, et al., 2004; Brown, 2000; Brown, 1998) or other existing landform thematic maps (USGS Land Cover Institute, 2012). This is another advantage to having the output orthoimage GSD match the GSD of the DEM used for the orthorectification process during MSI feature extraction (Brown, 2013). The alignment combined with the registration of the input DEM raster and the output orthoimage will assist future research to find relationships between the thematic map classes and descriptions of the terrain surface including slope, aspect, and roughness.

Figure 1 shows the orthorectification process of a theme map from MSI feature extraction to prepare for STOMP that allows direct comparison of MSI feature classes and the terrain surface descriptions derived from the DEM raster. This improves the MSI feature extraction results compared to extracting features from the orthorectified MSI. It is therefore advised that the image of the thematic map should be extracted from the original unrectified MSI first, without extracting features from the orthoimage which perturbs the spectral and spatial properties of the original unrectified MSI. The pixel connectivity, for linear features such as roads that are only one pixel wide, also can be disturbed by the orthorectification process when it samples the original unrectified MSI.

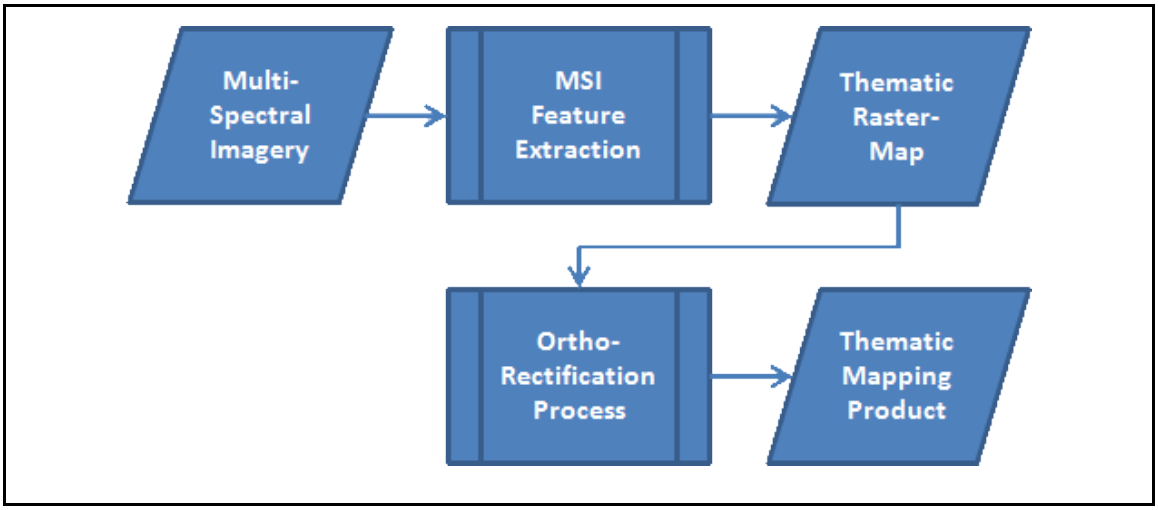

Figure 1: MSI Theme Map Orthorectification Process

1.4 Study Purpose

The research objective is to describe and assess the spatial accuracy of orthorectified MSI when the input DEM raster GSD matches the nominal input GSD from the MSI. The orthorectification process also is a practical method to register the MSI to the DEM, for describing the terrain surface from derivatives of DEM such as slope and aspect. There also is a single terrain height value for each MSI orthoimage pixel when aligning output orthoimage GSD (and its XY axis origin) with the input DEM raster GSD that could enhance the accuracy assessment and the MSI feature extraction process. This research finds how the input GSD from the DEM raster, when it matches the input nominal GSD of the original unrectified MSI, affects the spatial accuracy of the output orthoimage. This study presumes that the:

- LiDAR DEM raster vertical accuracy is better than a half-meter, the
- GSD of the DEM matches or betters the nominal GSD of the MSI, and the
- MSI orthorectification process has a defined sensor model.

The terrain shape affects MSI geometric response to specular and diffuse reflectance of energy (Campbell & Wynne, 2011, pp. 48-56; Lillesand, et al., 2008, pp. 24-29) where multi-angle and multi-spectral reflectance can clarify Worldview2 MSI feature extraction results (Longbotham, et al., 2012) if the MSI is adequately registered to the DEM**.** Knowing the terrain geometry from the DEM can reduce spectral confusion within shaded terrain during MSI feature extraction (Hoshikawa & Umezaki, 2014). The DEM can improve the MSI classifier performance, because the DEM describes the terrain of complex landscapes that challenges the spectral classifiers (Lu & Weng, 2007). Note that the effects of terrain on spectral classifiers are ignored in this study, because it is only concerned with the spatial accuracy of the orthorectification process.

CHAPTER TWO

2.1 Overview

This chapter describes the current state of the art for the orthorectification process, along with its concepts and data structures, with enough detail to later assess the accuracy of the output orthoimage from Multi-Spectral Imagery (MSI). It describes prior related efforts, including some expected outcomes from this study. The methods and results of the orthorectification process used for this study are described in later chapters with more detail.

2.2 LiDAR DEM & RPC Sensor Models

The entire dataset spans the southern Willamette Valley watershed in the Pacific Northwest of the United States. The Willamette river and valley is the product from 150 million years of geologic history in Oregon that is described elsewhere (Madin, 2009). The confluence of the Willamette and McKenzie Rivers at the south end of the valley is located within the Census Bureau urbanized area of Eugene-Springfield Oregon. Eugene is on the west side of Interstate-5 and Springfield is on the east side of Interstate-5, where the highway goes north-south through the center of Willamette Valley within Oregon. There is a large variety of natural and urbanized terrain within this chosen area to assess the accuracy during the orthorectification process.

The data is located within Lane County of Oregon. This Eugene-Springfield urban zone has a 2013 total population of 159,190 people for 708 persons per square kilometer of land (US Census Bureau - Population Estimates, 2014; US Census Bureau - Geography, 2014).[2] The Eugene-Springfield urban area, identified by the US Census Bureau, within the southern Willamette Valley of Oregon contains the study sites.

The Light Detection and Ranging (LiDAR) Digital Elevation Model (DEM) data was provided by the Oregon State University (Oregon State University Spatial Data Management Group, 2013) that shares the LiDAR data from the Oregon LiDAR Consortium (OLC) of the Oregon Department of Geodesy and Mineral Industries (DOGAMI).[3] The Oregon DOGAMI describes this LiDAR data further (Oregon Department of Geodesy and Mineral Industries - DOGAMI, n.d.). The commercial satellite Worldview2 MSI has the National Imagery Transmission Format (NITF) with a Rational Polynomial Coefficients (RPC) sensor model to apply the orthorectification process (National Imagery Transmission Format Standard Technical Board, n.d.). The gathered MSI spans the same area as the acquired LiDAR DEM. The Worldview2 with RPC was attained from the DigitalGlobe Foundation (DigitalGlobe, 2013; DigitalGlobe - GeoFUSE Search & Discovery Platform, 2013; DigitalGlobe - ImageFinder, 2013) by the

---

[2] Found population density from values provided by US Census Bureau. 2013 Population Estimate for "Eugene city, United States" from "PEPANNRSIP.US12A.xls" table, and land area in square meters (ALAND10) from "cb_2013_us_ua10_500k.dbf" table. Population Estimate for city divided by ALAND10 (square meters of land for that city) times 10^6 for people per square kilometer. This calculation presumes that city shapes match urbanized area where population is estimated.

[3] Light Distance and Ranging (LiDAR) Digital Elevation Model (DEM) data was provided from the Oregon LiDAR Consortium (OLC) <http://www.oregongeology.org/sub/projects/olc/> to the Oregon State University (OSU) with permission from OSU to use it for this study and other projects.

Army Geospatial Center (AGC) Imagery Office of the US Army Corps of Engineers (Army Geospatial Center, n.d.).[4]

Figure 2 shows the outlines of the LiDAR DEM raster and Worldview2 MSI data gathered for this study, that combines the WorldView2 and LiDAR DEM datasets together for the accuracy assessment, where the sample image for the "MSI 20_01_P007" frame is shown there. This description for the gathered data provides the overall context for the accuracy assessment of the orthorectification process.

[4] WorldView-2 MSI data was provided from the Army Geospatial Center (AGC) Imagery Office <http://www.agc.army.mil/Media/FactSheets/FactSheetArticleView/tabid/11913/Article/10149/agc-imagery-office.aspx> with permission from the AGC Imagery Office to use it for this study.

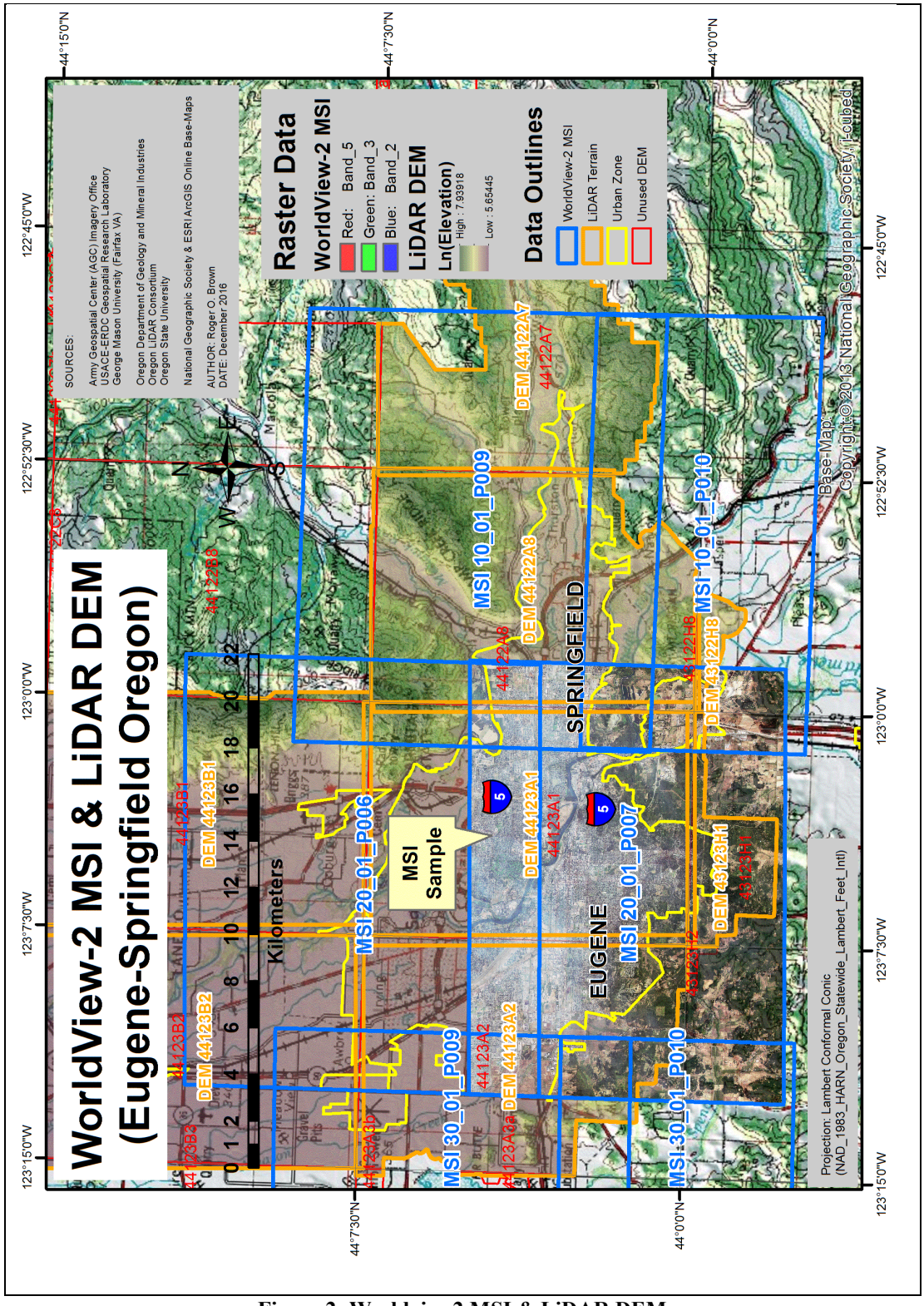

Figure 2: Worldview2 MSI & LiDAR DEM

The point cloud of LiDAR data includes a DEM raster of the terrain heights with a Ground Sample Distance (GSD) of three feet, where it is derived from the DEM point cloud by the OLC. The LiDAR point cloud data is converted to a DEM raster given OLC standards for high resolution data in the Pacific Northwest (English, 2010; English, 2010; Watershed Sciences, 2009; Madden & English, 2009). The delivery acceptance reports include more detail about the format and the content of the LiDAR elevations (what the OLC calls the "highest hit" terrain heights) and intensity data, including a description of the Oregon statewide Lambert Conformal projection and North American Datum 1983 (NAD83) for the DEM raster with horizontal and vertical units of feet. The provided DEM is registered to a network of survey points by the OLC.[5]

The entire LiDAR point cloud is converted to a WGS84 datum with horizontal units of decimal degrees for longitude (X) and latitude (Y) before forming a DEM raster of terrain heights (Z) that is used for the orthorectification process for MSI with the RPC sensor model, where the unit of the terrain heights also is converted from feet to meters that is expected by the RPC sensor model. Another report describes the current usage of the LiDAR DEM raster to support the orthorectification process for MSI with a RPC sensor model, where this orthorectification process also requires a DEM within a World Geodetic System (WGS 84) geographic coordinate system with a longitude-latitude projection and datum (with horizontal units of decimal degrees and with vertical units of

[5] The OLC data apparently was collected for reasons besides producing orthoimages, but that LiDAR was readily available for reuse within this and other studies.

meters) expected by the RPC sensor model regardless of the projection and datum for the available LiDAR DEM (Brown, 2014).

Table 1 shows that the input spatial reference for the LiDAR DEM raster that has a horizontal XY coordinate system of the 1983 North American Datum (NAD83) High Accuracy Registration Network (HARN) Oregon Statewide Lambert Conformal projection (International Feet) with 3-feet horizontal resolution, and with the units of feet for terrain heights of the 1988 North American Vertical Datum (NAVD88). Where the LiDAR data format and contents are described several reports to or from the Department of Geology and Mineral Industries (DOGAMI) Oregon LiDAR Consortium (OLC) (Watershed Sciences, 2009; Madden & English, 2009). The vertical datum transforms are described elsewhere (Briney, 2016; National Oceanic and Atmospheric Administration - NOAA, 2016; Doyle, n.d.; National Geodetic Survey, n.d.).

Table 1: Point Cloud Input & Output Coordinate Systems

Input Spatial Reference	
Projection	NAD_1983_HARN_Oregon_Statewide_Lambert_Feet_Intl
Linear_Unit	Foot (0.304800 Meters)
Angular_Unit	Degree (0.0174532925199433)
False_Easting	1312335.95800524 (Feet)
False_Northing	0.0 (Feet)
Central_Meridan	-120.50 (Degrees)
Standard_Parallel_1	43.00 (Degrees)
Standard_Parallel_2	45.50 (Degrees)
Latitude_of_Origin	41.75 (Degrees)
XY_Datum	NAD_1983
XY_Spheroid	GRS_1980
Z_Datum	ArcGIS: NAVD_1988
Z_Datum	Imagine: NAVD_88_GEOID…
XY_Units	Feet
Z_Units	Feet
Output Spatial Reference	
Projection	D_WGS_1984
Datum & Spheroid	D_WGS_1984
XY_Units	Decimal Degrees (0.0174532925199433 Radians)
Z_Units	Meters

Figure 3 shows the XY coordinate system for the LiDAR point cloud and Z value of the NAVD 1988 (NAVD88) datum for the DEM Z values. The NAVD88 datum is one of many geoids for measurement and representation of the Earth including its gravitational field that is related to Global Positioning Systems (GPS) from satellites and mean sea level (Campbell & Wynne, 2011, pp. 392-397; Lemoine, et al., 1998). The NAVD88 Z values are converted by the image processing system toward the WGS84 Z values to cause a vertical shift of the terrain heights contained within the DEM raster before the

orthorectification process begins. This vertical shift will shift features horizontally within the output orthophoto regardless of the actual Z values used by the orthorectification process. Vertical error within the DEM raster will likewise cause horizontal error within the produced orthophoto.

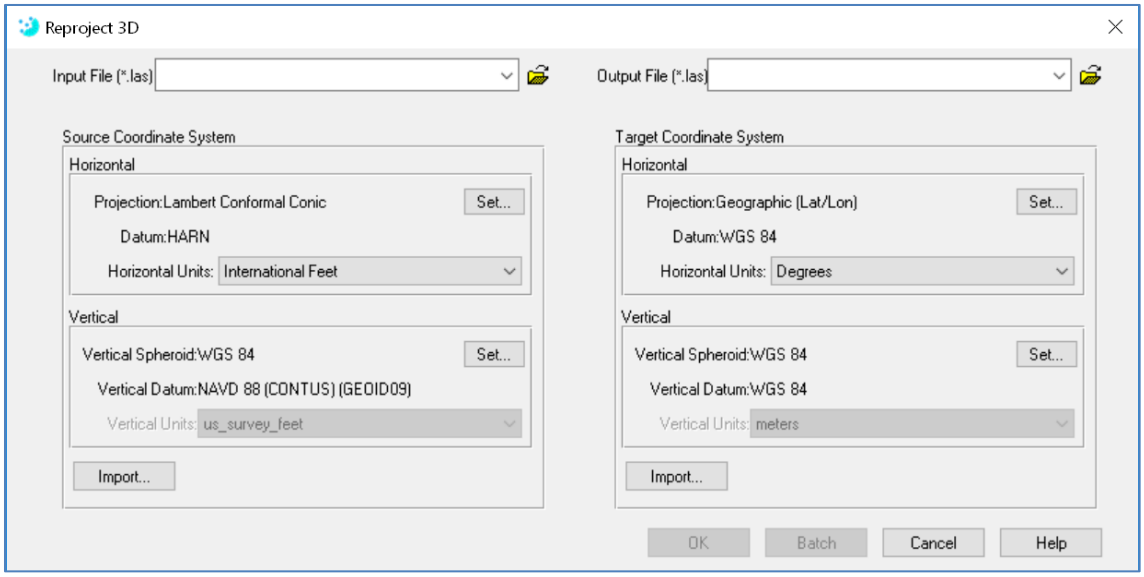

Figure 3: Converting Elevations NAVD 1988 (GRS80) To WGS 1984

The commercial satellite Worldview2 product includes a sensor model of RPC for the MSI orthorectification process. The RPC of this sensor model is provided along with the MSI, and the orthorectification process expects the LiDAR DEM raster to be in the horizontal and vertical WGS 84 geographic coordinate system. This RPC sensor model projects the DEM raster into the sensor image to find brightness values from the MSI regardless if the sensor has perspective, panoramic, or line-scanner geometry (Ehlers, et al., 2009; Jacobson, 2008; Croitoru, et al., 2004; Hu, et al., 2004; Tao & Hu, 2001).

2.3 Orthorectification Process

The orthorectification process removes most geometrical distortions and displacements within satellite or aerial original MSI regarding the positional accuracy of its measured coordinates (Mugnier, et al., 2013; Forstner & Wrobel, 2004; Burtch, n.d.). This allows better geometry for accurately measuring horizontal dimensions of features after conducting the MSI orthorectification process. The process also prepares for converting the MSI between projections and datum of photomaps with other features graphically overlaid onto the image. These orthoimage products are used for tactical decision aids and situational awareness that benefit military operations and emergency response, by allowing the user to see imagery context beneath the map symbols (US Army Infantry School, 2001; United States Army Corps of Engineers, July 2002).

The sensor model uses the X and Y values where the Z value is presumed to be located exactly at the centroid of each DEM raster cell. The maximum Z value throughout each cell is assigned to each centroid within the DEM raster to depict the reflective terrain surface (skin). It is uncertain how choosing the highest hit for the Z value within each DEM raster cell will affect the results, instead of using the Z value from the point that is nearest to each centroid point in the raster. It depends on where the elevation discontinuity occurs within each raster cell that reflects a cliff or sidewall of a vertical terrain facet. An average Z value of all points from the cloud could also be used as the expected terrain height within each raster cell. Interpolating the terrain height values from the DEM raster contributes to MSI orthoimage spatial error (1) when the mode of the height values from the DEM raster is used that presumes a flat terrain

throughout the entire area and (2) when minimal interpolation of terrain height value occurs from the DEM raster GSD matching the original unrectified MSI nominal GSD The following cases are considered within this study.

Equation 1 shows how the RPC are applied to project the DEM raster into the MSI for finding the pixel with a corresponding brightness value of $\boldsymbol{b_i}$ in from each $\boldsymbol{i^{th}}$ band (National Imagery and Mapping Agency, November 2011; Open Source Geospatial Foundation (OSGeo), n.d.).

$$[\boldsymbol{x, y, z, b}_i]_{\boldsymbol{Ortho}} = [\boldsymbol{x, y, z}]_{\boldsymbol{DEM}} \rightarrow [\boldsymbol{x'}, \boldsymbol{y'}, \boldsymbol{b}_i]_{\boldsymbol{MSI}} \qquad \textbf{Equation 1: DEM to MSI Projection}$$

Equation 2 shows how current commercial image processing software projects each grid cell for the output orthoimage, with a terrain height value ($\boldsymbol{z}$) that is found from the DEM raster, by using the RPC (Ehlers, et al., 2009, pp. 733-738; Tao & Hu, 2001; Hu, et al., 2004). The equations replace the actual sensor model to produce a MSI orthoimage with geometric spatial distortions removed from the original unrectified MSI. This pair of equations forms two quotients, each with a ratio of two polynomials called rational functions for multiple variables, including DEM raster cells $(\boldsymbol{x, y, z})$ transformed to pixels in image space $(\boldsymbol{x', y'})$.[6]

[6] This mathematical notation was developed to clarify how each RPC relate to the exponential powers of the $\boldsymbol{x}$, $\boldsymbol{y}$, and $\boldsymbol{z}$ DEM.

$$x' = \frac{\boldsymbol{P}(\boldsymbol{x},\boldsymbol{y},\boldsymbol{z})}{\boldsymbol{Q}(\boldsymbol{x},\boldsymbol{y},\boldsymbol{z})} = \frac{\sum_k \sum_j \sum_i (\boldsymbol{a}_{ijk})_p (\boldsymbol{x}^i)(\boldsymbol{y}^j)(\boldsymbol{z}^k)}{\sum_k \sum_j \sum_i (\boldsymbol{a}_{ijk})_q (\boldsymbol{x}^i)(\boldsymbol{y}^j)(\boldsymbol{z}^k)}$$

$$y' = \frac{\boldsymbol{R}(\boldsymbol{x},\boldsymbol{y},\boldsymbol{z})}{\boldsymbol{S}(\boldsymbol{x},\boldsymbol{y},\boldsymbol{z})} = \frac{\sum_k \sum_j \sum_i (\boldsymbol{a}_{ijk})_r (\boldsymbol{x}^i)(\boldsymbol{y}^j)(\boldsymbol{z}^k)}{\sum_k \sum_j \sum_i (\boldsymbol{a}_{ijk})_s (\boldsymbol{x}^i)(\boldsymbol{y}^j)(\boldsymbol{z}^k)}$$

Equation 2: $(x',y')_{MSI} = f\,(x,y,z)_{DEM}$

Where

$\boldsymbol{a}_{ijk}$ = the RPC delivered along with the MSI, for example the $(\alpha_{221})_p$ coefficient in polynomial "$\boldsymbol{p}$" for its $(\boldsymbol{a}_{221})_p(\boldsymbol{x}^2)(\boldsymbol{y}^2)(\boldsymbol{z}^1)$ term.

$\boldsymbol{P}$ and $\boldsymbol{R}$ = functions in the numerators for the equations

$\boldsymbol{Q}$ and $\boldsymbol{S}$ = functions in the denominators for the equations

$\boldsymbol{P}$, $\boldsymbol{Q}$, $\boldsymbol{R}$, and $\boldsymbol{S}$ each have a different set of 20 unique coefficients, say $\{\boldsymbol{P}:(\boldsymbol{a}_{ijk})_p\}$ for example, where there is a different coefficient for each product of $\boldsymbol{x}$ raised to the $\boldsymbol{i}^{th}$ power, $\boldsymbol{y}$ raised to the $\boldsymbol{j}^{th}$ power, and $\boldsymbol{z}$ raised to the $\boldsymbol{k}^{th}$ power.

Equation 3 and Equation 4 show how the $[\boldsymbol{x},\boldsymbol{y},\boldsymbol{z}]$ coordinates of the DEM and the $[\boldsymbol{x}',\boldsymbol{y}']$ coordinates of the MSI are offsets from each of the defined origin of both coordinate systems for the RPC model that also are scaled into values without units that range between -1 and +1. The origin for each coordinate system is contained in the NITF metadata along with the RPC, so these coordinates become components of the projective vector from the DEM to the MSI.

$$x = \frac{(x - x_0)}{S_x}$$
$$y = \frac{(y - y_0)}{S_y}$$
$$z = \frac{(z - z_0)}{S_z}$$

Equation 3: Coordinates $(x,y,z)_{DEM}$

$$x' = (x' - x'_0) \Big/ S_{x'}$$
$$y' = (y' - y'_0) \Big/ S_{y'}$$

Equation 4: Coordinates $(x',y')_{MSI}$

Equation 5 shows the collinearity perspective projection geometry of the vertical aerial photograph (Moffitt & Mikhail, 1980, pp. 133-170; Lillesand, et al., 2008, pp. 123-188) by using the same notation as for the RPC equations. Where the first order RPC might describe the exterior and interior orientations of sensor model for perspective projection of the aerial vertical frame image. The denominators are equal ($S=Q$) within the collinearity equations, but they might be unequal within the RPC equations, and the order for each polynomial is more limited to the first order compared to the higher orders of the RPC. Where and $S_x = S_y = S_z = 1.0$ within Equation 3, and there is a focal length (f) that equals $S_{x'}$ and $S_{y'}$ within Equation 4. This reduces a more complex RPC sensor model to a smaller set of parameters for the collinearity equations to allow approximate distance measurements along the slant range of the sensor Line-of-Sight (LOS), within perspectives when the sensor LOS might intersect the terrain surface more than once.

$$(x' - x'_0)/f = \frac{P(x,y,z)}{Q(x,y,z)}$$

$$= \frac{(a_{000})_p + (a_{100})_p(x) + (a_{010})_p(y) + (a_{001})_p(x)}{(a_{000})_q + (a_{100})_q(x) + (a_{010})_q(y) + (a_{001})_q(z)}$$

$$(y' - y'_0)/f = \frac{R(x,y,z)}{S(x,y,z)}$$

$$= \frac{(a_{000})_r + (a_{100})_r(x) + (a_{010})_r(y) + (a_{001})_r(z)}{(a_{000})_s + (a_{100})_s(x) + (a_{010})_s(y) + (a_{001})_s(z)}$$

Equation 5: Collinearity Perspective Projection

Figure 4 describes the steps that convert the coordinate system of the LiDAR DEM raster as input required by the orthorectification process. Constructing the DEM raster of Z values for terrain heights, to prepare for the RPC orthorectification process, was the most complex aspect of this study. This process was developed to start with a LiDAR point cloud of terrain heights for the MSI orthorectification process, after the point cloud is converted to DEM raster of Z values for the terrain heights with the units and projection expected by the RPC sensor model. Then the constructed DEM raster is input into the orthorectification process.

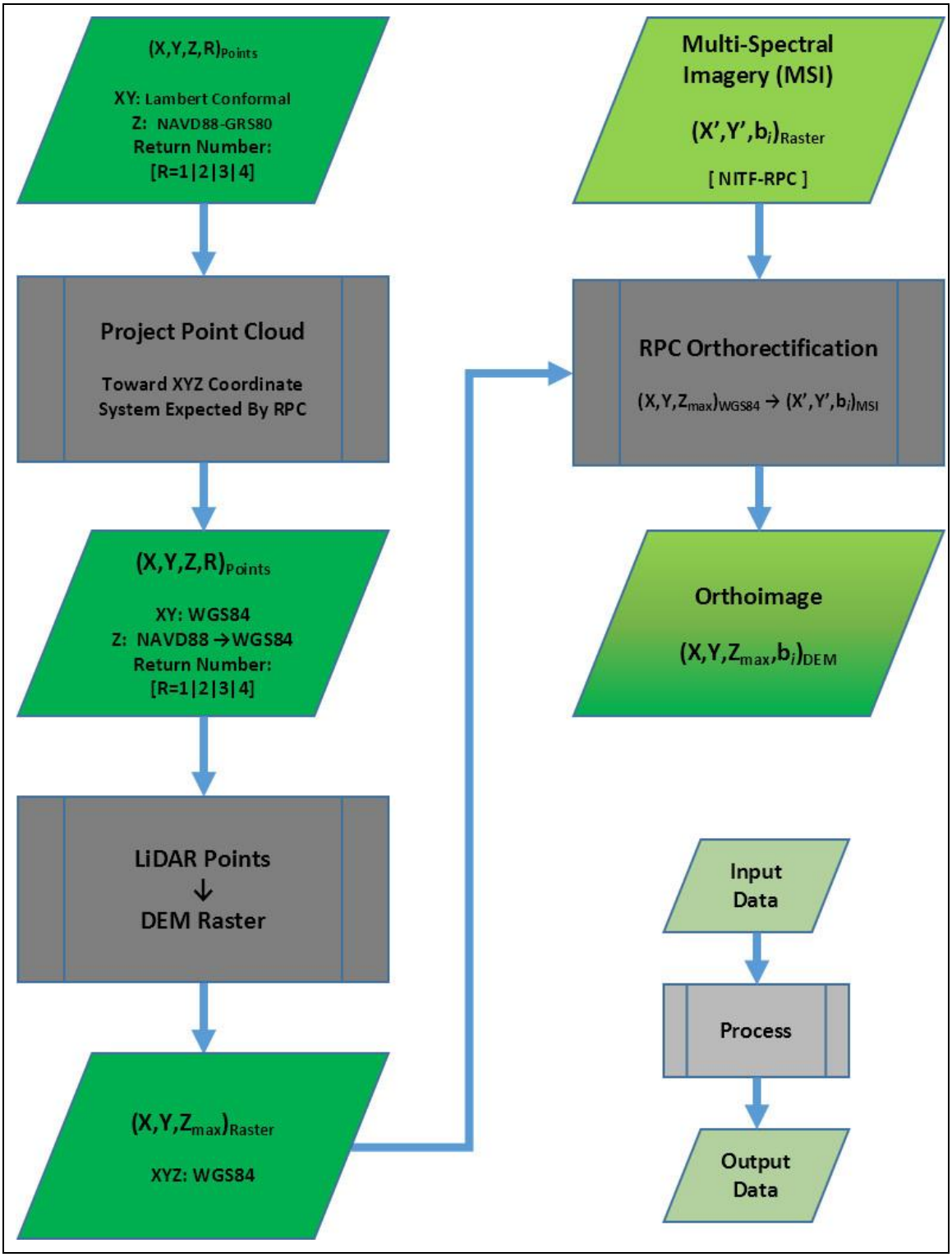

Figure 4: Orthorectication Process Flowchart

The orthorectification process requires converting the LiDAR point cloud from its original horizontal (XY) and vertical (Z) coordinate systems into the 1984 World Geodetic System (WGS84) horizontal XY coordinate systems of geographic longitude-latitude and WGS84 vertical Z elevation values for terrain heights. The process of directly converting the LiDAR DEM raster to the heights across the terrain surface adds an additional interpolation error into the XY that is expected by the RPC sensor model, unless the point cloud is converted into the spatial reference expected by the RPC sensor model before it is used to produce the LiDAR DEM raster for the orthorectification process. Any steps to directly convert a DEM raster into the projection and datum expected by the RPC only exists if the point cloud of LiDAR terrain heights is unavailable for the orthorectification process, perhaps because the volume of the point cloud exceeds the data storage capacity where it might be discarded after conversion to a DEM raster of terrain heights by producers and consumers of LiDAR products. Converting the point cloud to a raster might require excessive computer resources, but a desktop computer can process the LiDAR point cloud within limited data spans if needed.

The current production practice attains the DEM raster after others converted the LiDAR point-cloud into a grid of terrain heights, for a Cartesian coordinate system (of orthogonal X and Y axes) with a conformal projection of the mapping surface that minimizes distortions of measured horizontal dimensions (Pearson, 1984). This introduces some error when the DEM raster is directly converted from another XY coordinate system to what expected by the RPC. Because the XYZ coordinate system of the LiDAR point cloud normally is a planar projection, but the XYZ coordinate system

required by the RPC for satellite imagery has a WGS84 geographic coordinate system with a spherical projection and datum (Dale, 2005, pp. 4-8). This means that the coordinate systems X and Y axes are skewed between each other with different X and Y scales, because one projection is planar and the other is spherical shown in in Figure 6. This also might mean an affine angle exists for non-perpendicularity between the X and Y axis of the spherical coordinate system (Moffitt & Mikhail, 1980, pp. 589-603).

The 6-parameter affine transformation of a 2-dimensional XY coordinate system causes a square raster cell within the planar projection to have a parallelogram shape within a spherical projection, but each parallelogram shape will have the same area for every raster cell throughout the entire new coordinate system. It will introduce interpolation error into DEM raster, used for the orthorectification process, to directly convert the raster with a planar Cartesian coordinate system (with perpendicular X and Y axes) of linear units into a raster with a spherical projection of X-Longitude (East) and Y-Latitude (North) of angular units (on the datum from an ellipsoid of revolution with unequal semi-major and semi-minor axes) that is reduced to the flat plane of a DEM raster. But the process for directly converting between the raster of two different projections is described elsewhere, if the LiDAR point cloud is unavailable (Brown, 2014, pp. 25-35).

This study describes the method for producing the DEM raster directly from the LiDAR point clouds with terrain surface heights, when the LiDAR point cloud is available, instead of using another DEM raster of terrain heights provided by somebody else that might be in a projection and datum besides what is expected by the RPC sensor

model. Where directly converting the preprocessed DEM raster from another projection and datum with different units besides WGS 84 longitude (X) and latitude (Y) in decimal degrees and terrain elevations (Z) in meters of the coordinate system expected from the RPC might be undesirable, when the coordinate axes between different projections might be skewed to each other that causes error by directly converting the DEM raster from one projection to another. The approach that directly converts the point cloud from one coordinate system to another therefore improves the accuracy of the DEM, because it reduces error from the converting between DEM grid lattices with axes that are skewed between the different coordinate systems, before the DEM raster of terrain heights is used by the RPC sensor model during the orthorectification process. It also allows the orthorectification process to output an orthoimage with the same dimensions as the input DEM raster, where this provides a single DEM terrain height value located at the centroid for each orthoimage pixel.

The LiDAR DEM raster likely has horizontal XY and vertical Z coordinate systems that need conversion into the units, projection, plus horizontal and vertical datum of WGS 84 meters expected by the RPC sensor model (Brown, 2014). The orthorectification process then projects spots with estimated terrain height values from the DEM raster into the original MSI by using the provided RPC sensor model, after converting the LiDAR point cloud of elevation values within the WGS 84 coordinate system into the DEM raster of terrain heights. The process to directly convert the point cloud from its spatial reference into the XYZ coordinate system expected by the RPC sensor was developed for this thesis, because the WGS 84 point-cloud should be directly converted to the WGS 84

DEM raster before producing the orthoimage to reduce interpolation error. This new development therefore replaces a current orthorectification process to reduce the interpolation error from directly converting the LiDAR raster with heights of the terrain surface into the projection and datum of the DEM expected by the RPC sensor model (Brown, 2014, pp. 42-48).

The horizontal spatial resolution of the DEM raster can match the nominal GSD for the original unrectified MSI, after it is converted from the point cloud to the XYZ coordinate system expected by the RPC sensor model that will be used within this study, because it shows how using DEM raster spatial resolution that matches the nominal MSI resolution affects the orthorectification results. The nearest neighbor interpolation will be used throughout every case of the entire orthorectification process regardless of the nominal GSD for the input MSI, without using any bilinear or cubic interpolation because of their potential to contribute error from averaging MSI brightness values within urbanized areas with a high frequency of elevation discontinuities.

Feature extraction within the original MSI is advised, instead of doing it within the produced orthoimage, to avoid changing the spectral and spatial patterns of the exposed terrain within the original unrectified MSI exposure. So orthorectification of the thematic image for features extracted by spectral patterns within the original unrectified MSI is recommended. This prevents feature extraction from the orthoimage that has perturbed spectral and spatial patterns compared to the unrectified MSI.

This study uses a LiDAR DEM raster with XY and Z WGS 84 coordinate system that is directly derived from its LiDAR point cloud of terrain heights (Z) with the

orthorectification process for commercial satellite Worldview2 MSI. It also provides a design for employing the orthorectification process by other geographic information and image processing software besides the systems and data used for this thesis, if the point cloud is dense enough to provide a DEM raster has GSD comparable with the nominal spatial resolution of the original unrectified MSI. The spectral and spatial artifacts from feature extraction within the orthoimage, instead of from the unrectified MSI, are beyond the scope of this study however.

2.4 Orthoimage Accuracy Assessment

A unique method is applied for numeric and visual assessment of the MSI orthorectification process regarding the relative horizontal accuracy from using the LiDAR DEM raster, that is different from previous efforts to assess orthoimage accuracy (Hobi & Ginzler, 2012; Nowak Da Costa & Walczynska, 2011; Elaksher, 2009; Liu, et al., 2007; Toutin, 2003). Geographic information and image processing products are used to produce orthoimages and to measure relative positional differences between the input DEM raster and the output orthoimage.

Some rendering anomalies from the orthorectification process occur, besides measured offsets between the image of the input DEM raster and the output orthoimage, because the perspective view from the sensor LOS might intersect the urbanized terrain surface more than once because of sharp elevation discontinuities. That can cause a doubly exposed feature “ghost” within the output orthoimage of the rooftop texture within the output orthoimage, unless the orthorectification process is adjusted to replace the double exposure with null pixels farther along the sensor LOS projection between the

DEM raster of the terrain surface, that is also described in previous literature (Zhou, et al., 2005; Thorpe, 2001). These problems are described with more detail in later chapters.

CHAPTER THREE

3.1 Orthorectification Data & Methods

This chapter describes the data and methods for the orthorectification process, that uses the Light Detection and Ranging (LiDAR) Digital Elevation Model (DEM) including commercial satellite Worldview2 Multi-Spectral Imagery (MSI) with a Rational Polynomial Coefficient (RPC) sensor model. The sensor model delivered with the MSI is used for this study, without any adjustment of the RPC from the LiDAR DEM, despite existing tools that could adjust the RPC from the same DEM before it is used for the orthorectification process. This orthorectification process also results in a single terrain height from the DEM raster for each orthoimage pixel to assist the accuracy assessment, and to support use of the DEM as an extra layer that might enhance MSI feature extraction.

Figure 5 shows the study site where the orthorectification process is applied. The accuracy assessment of its output orthoimage is done after processing the quadrangle of LiDAR data and the Worldview2 MSI data that spans the 7.5 by 7.5 arc-minutes for the 44123A1309 western quadrangle for the University of Oregon in Eugene OR.

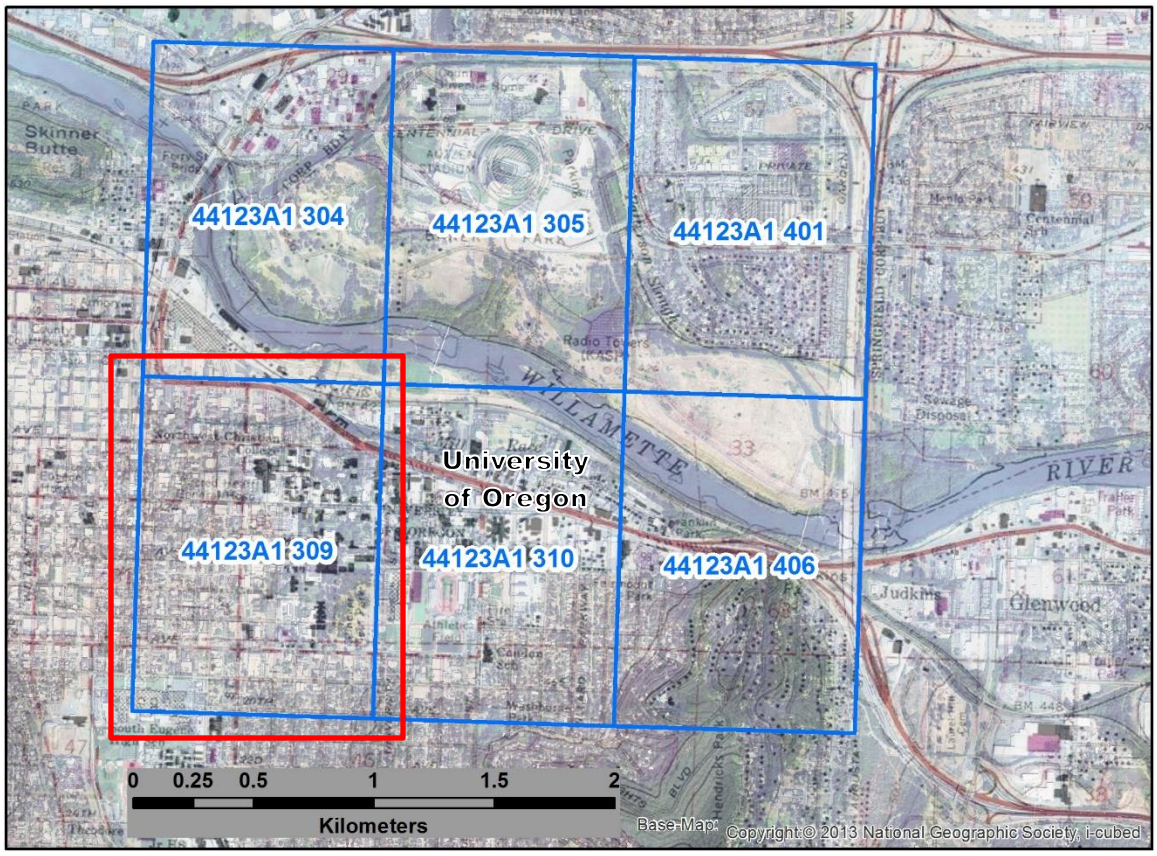

Figure 5: University of Oregon Campus West Quadrangle

3.2 LiDAR Point Cloud

The LiDAR data is provided in a LiDAR laser format (LAS). This data is converted to a list of points with XYZ coordinates before constructing a DEM raster of terrain heights from it. Each point in the cloud has several attributes that at least includes the:

- Return Number (which ranges from 1st - 4th return of each laser pulse),
- Returns (total number of returns for each laser pulse), and
- Intensity (brightness of the return of each laser pulse).

Figure 6 shows the overhead view of the site. The green points for Trees show where each laser shot has more than a single return, and gray point for Buildings (their rooftops)

or other points where there only is a single return for each laser pulse. Notice also how the blue gridlines for the longitude and latitude of the WGS84 coordinate system compares to the red gridlines every 400 yards for the Lambert Conformal Conic XY coordinate system. This shows how the axis of each coordinate system are skewed to each other, with a possibly different angle between the blue parallel of latitude and the Lambert X axis compared to the angle between the blue meridian of longitude and the Lambert Y axis. This implies that the conversion between the two coordinate systems requires at least a 6-parameter affine transformation between both coordinate systems.

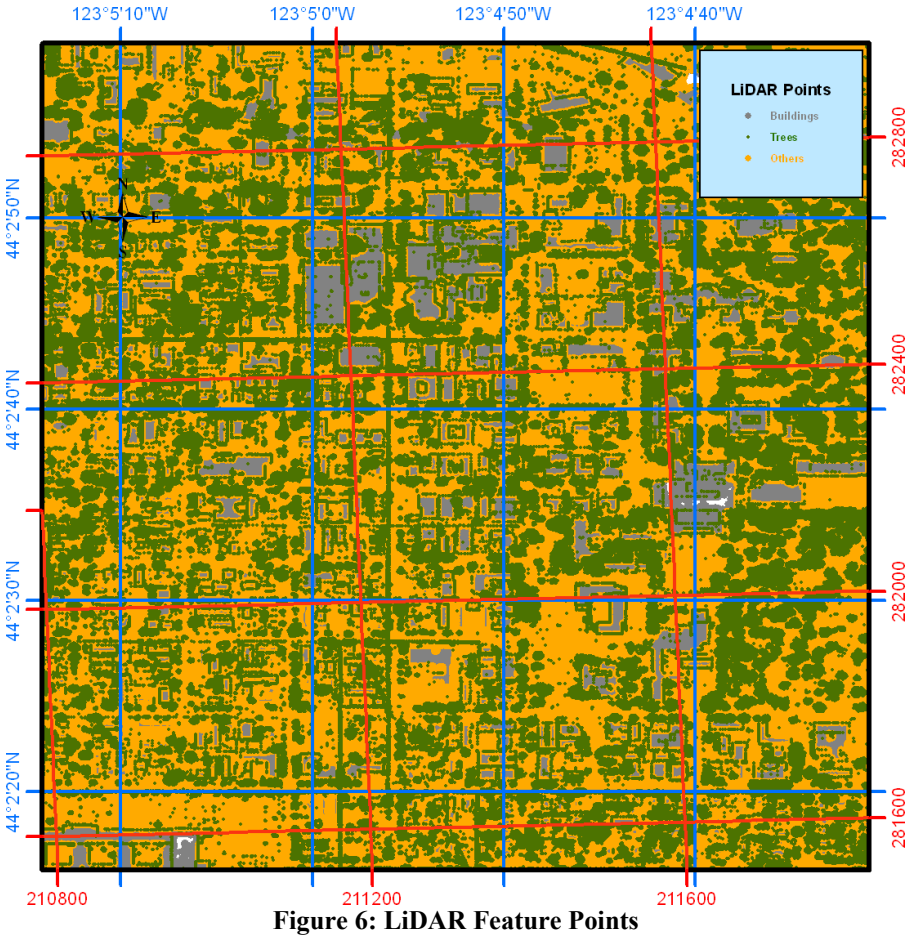

Figure 6: LiDAR Feature Points

Figure 7 shows the perspective view of the site when looking from the lower left hand corner of it, that is looking southward from the north toward the upper right hand corner. The gray points are from just a single return from each laser pulse, mostly points for the ground (bare terrain) and the rooftops of buildings. The green points are from laser shots that have more than a single return, with the green point getting dimmer for later 2nd-4th returns. The rooftops appear to float above the ground because sides of building are mostly unexposed to the overhead LiDAR sensor. More points that portray the sides of buildings could be collected by a LiDAR sensor on the ground, and this point cloud from the terrestrial viewpoint could be combined with the point cloud from the aerial collection, to show the walls of building with the perspective view of both combined point clouds. The gray and green points that appear on the sidewalls of buildings might introduce error if any of them become the maximum Z value of a DEM raster cell.

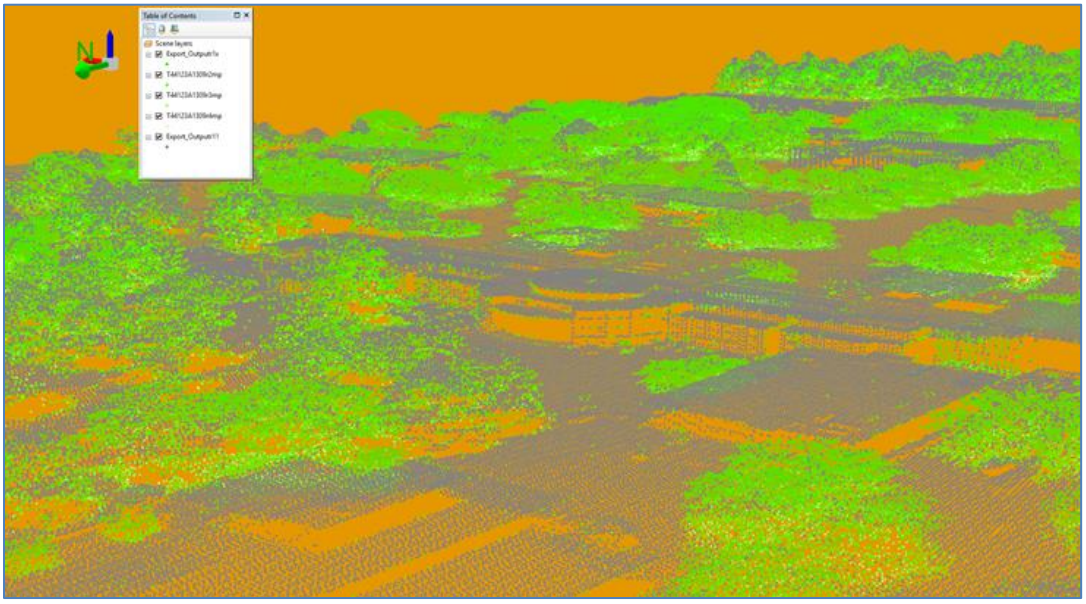

Figure 7: Perspective View Aerial LiDAR Point Cloud

Figure 8 shows how elevation discontinuities can be used for feature extraction directly from the LiDAR DEM raster, where that caused rooftops to float above the ground in the previous Figure 7. These portray the depth of tree canopies or the sidewalls of buildings at the edges of their rooftops. These elevation discontinuities with a large range of DEM raster cell Z values also might assist direct extraction of feature classes for vegetation and buildings. The terrain surface discontinuities are derived from subtracting the minimum Z value from the maximum Z value within each DEM raster cell.

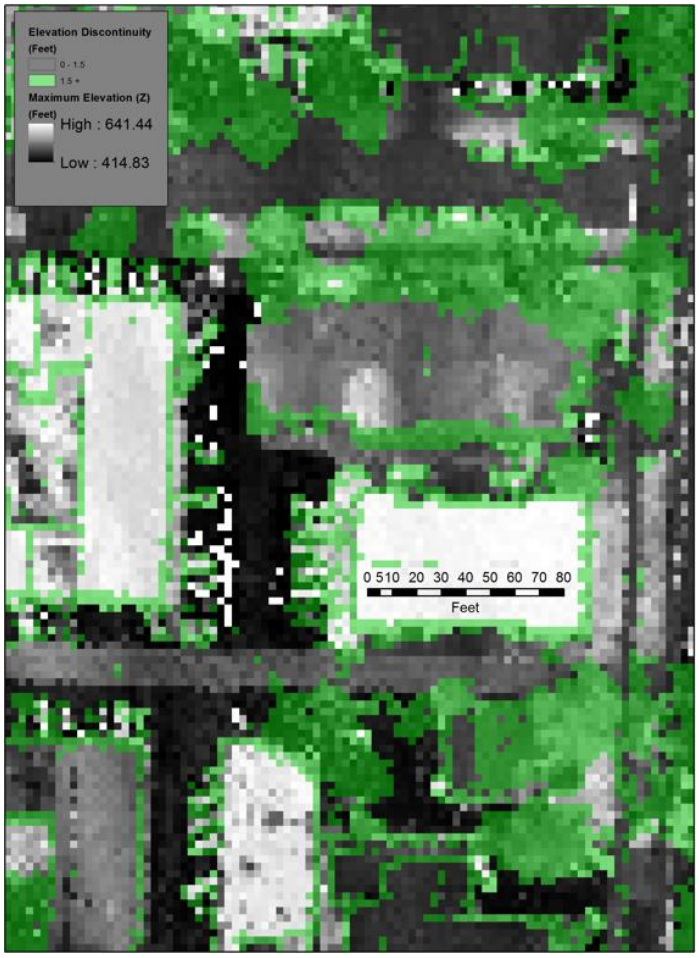

Figure 8: Terrain Height Elevation Discontinuities

3.3 Constructing DEM Raster

The LiDAR point cloud is converted to a DEM raster of terrain heights next. The DEM raster is used by the orthorectification process when forming an orthoimage from the MSI. A DEM raster of terrain heights that has matching dimensions with the output orthoimage is constructed, so that there is a single maximum Z value for each output orthoimage pixel. Constructing the DEM raster is the most complex aspect of the orthorectification process, and that is described next.

A DEM raster, from site "44123A1 309" with ¾ by ¾ arcminute dimensions, where it contains approximately 340 acres with 1663398 cells of 9 square feet located in the western quadrangle of the University of Oregon campus, is provided by the Oregon LiDAR Consortium (OLC) along with the LiDAR point clouds in the same projection and coordinate system that spans the area. The OLC DEM raster is a grid lattice of conjugate square cells with 3-feet width. But a new DEM raster derived from the point clouds for this study has 1.7 feet width that matches the 20.4 inches nominal pixel width of the original unrectified MSI to minimize interpolation error throughout the orthorectification process.

Figure 9 describes the properties of the OLC LiDAR data that consists of 11,436,019 points that were collected and processed over the site of 340 acres. Where the attributes in the LAS Dataset Properties are attached to each multipart point of the cloud when it is projected to other coordinate systems for the DEM raster. The "highest hit" of terrain height of all first returns within each DEM raster Z value are used by the RPC sensor model during the orthorectification process, because that maximum Z value represents

the reflective terrain surface exposed by the MSI sensor. The highlighted parts of the LAS dataset shows statistics for the number of points each of the 1st through 4th, First of Many, and Last of Many attribute regarding the Return that is the relative position of points along each waveform returned to the sensor.

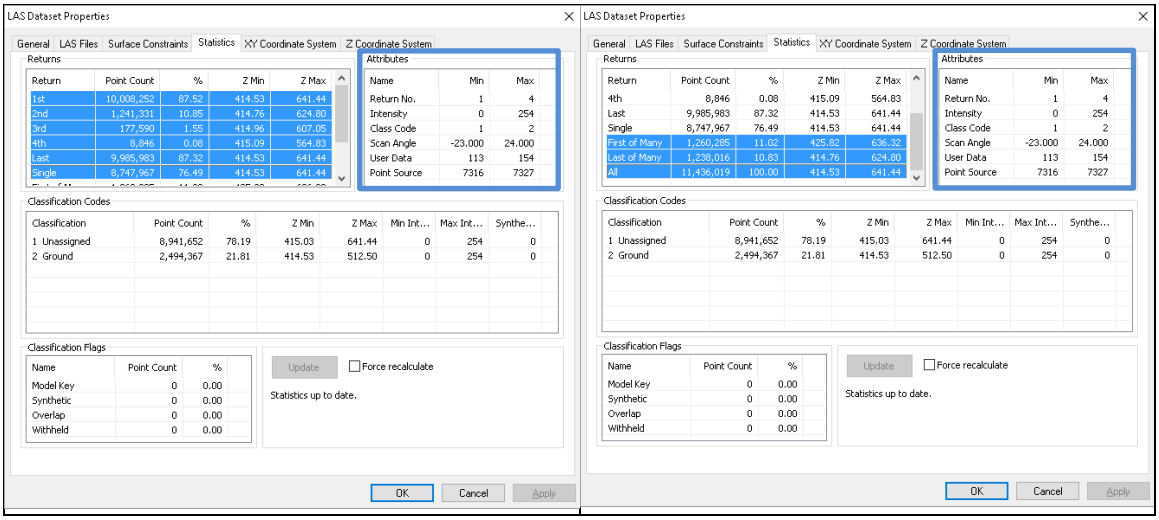

Figure 9: LiDAR Dataset Properties

Figure 10 shows the different feature extents of the point cloud with different units for the Lambert NAD83 HARN coordinate system and for the WGS84 geographic coordinate system. The RPC sensor model requires a XYZ coordinate system with the same horizontal and vertical datum of WGS84 for the DEM raster. Where the RPC use the WGS84 datum because the orbit of the satellite platform carrying the MSI sensor is tracked from there (The University of Texas At San Antonio - UTSA, 2006; Beer & Johnston, 1984; Mueller, 1969).

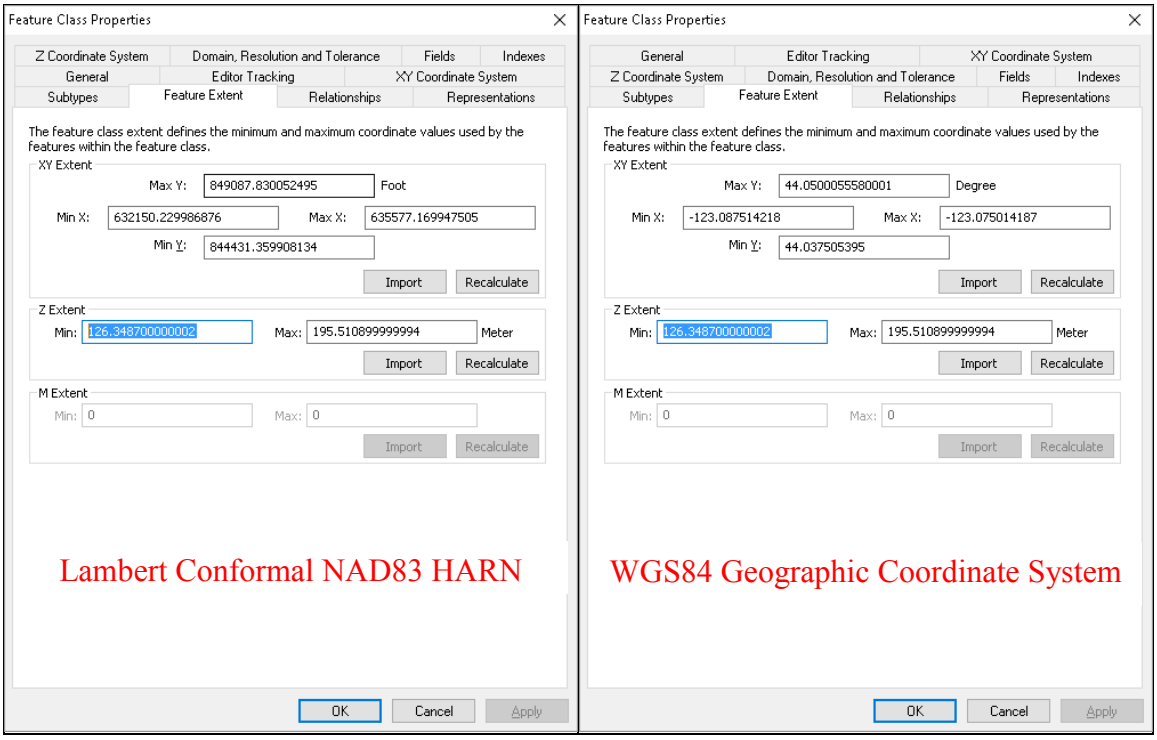

Figure 10: DEM Point Cloud Feature Extents

Figure 11 shows how to use the orthorectification process from a DEM with the constant Z value for terrain heights to determine the horizontal dimensions of the output orthoimage. This is done with the orthorectification function to determine the dimensions for the DEM fishnet-raster that will match with the output orthoimage dimensions, by inputting the WGS84 point cloud extent and then letting the function itself convert the cell sizes from input nominal GSD of 1.7 feet for the original unrectified MSI to decimal degree units. That prepares for spatially joining the LiDAR point cloud with the fishnet that is later converted to a DEM raster for producing the orthoimage with actual Z values. The results ensure a one-to-one match between a DEM raster Z value and a pixel from the original unrectified MSI that is cast to the output orthoimage, presuming the nominal

GSD expressed in the metadata is accurate. Equating the size of input DEM raster cell and output orthoimage pixels with the nominal GSD of the original unrectified MSI should minimize adverse results from interpolation in the orthorectification process.

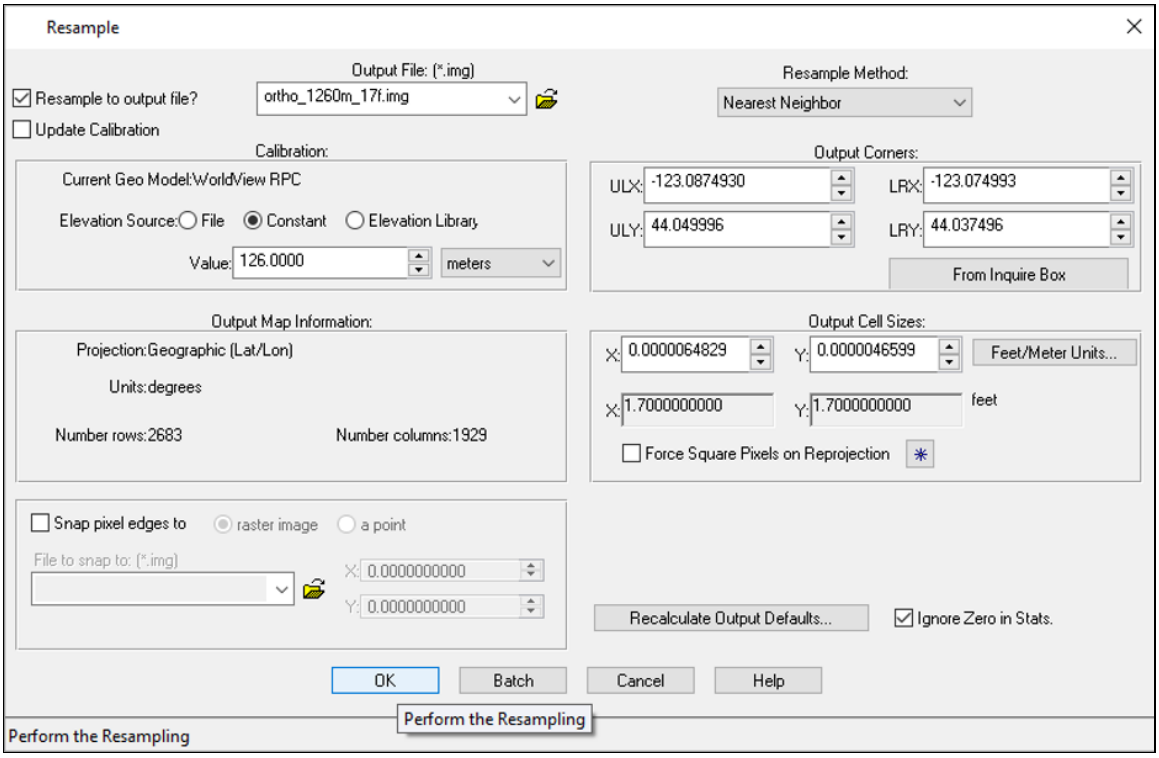

Figure 11: Finding Matched Dimensions For Output Orthoimage & Input DEM Raster

Figure 12 shows the output orthoimage resulting from the orthorectification process when using a constant elevation value. It aligns any subsequent DEM raster with the output orthoimage produced from the orthorectification process. The output orthoimage also portrays the result of using a DEM raster for flat terrain with all Z values equaling a single terrain height in meters, The constant Z values show how the orthorectification process still forms a coherent but inaccurate output orthoimage. Any subsequent DEM

rasters formed from the orthorectication process will be aligned with this output orthoimage that results in one terrain height Z value for each output orthoimage.[7]

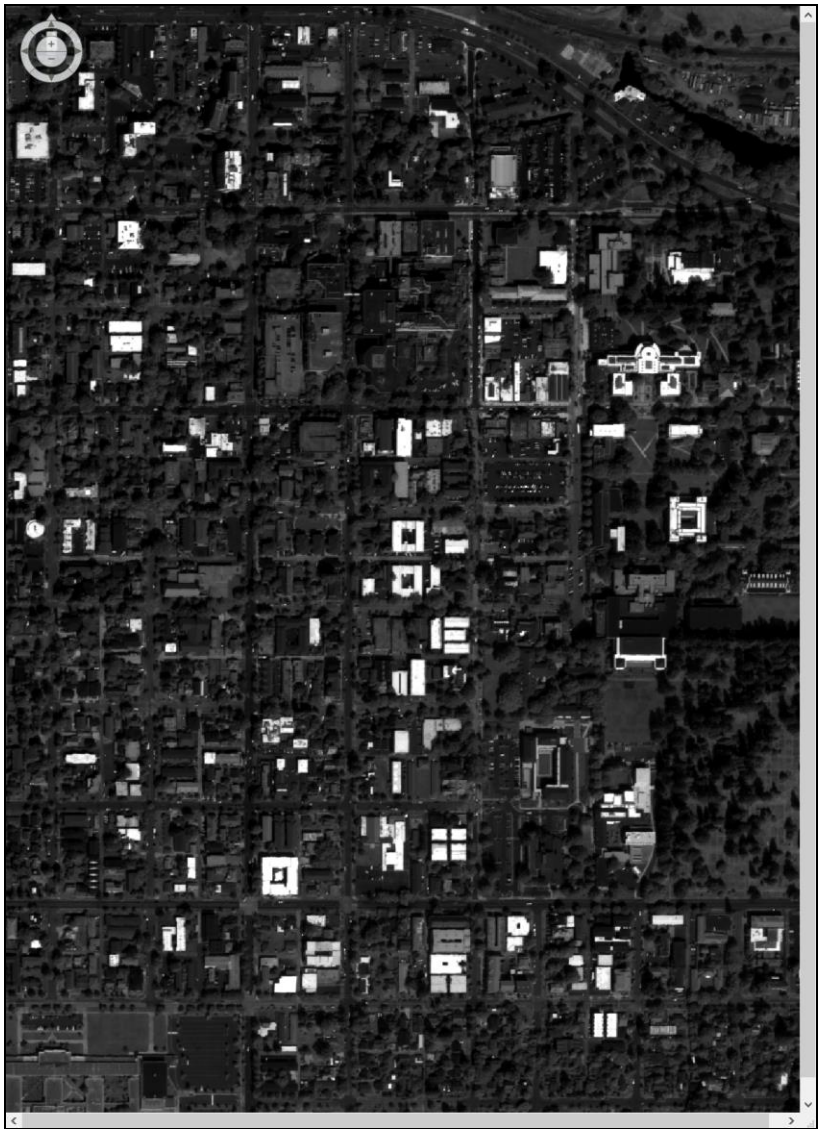

Figure 12: The MSI Orthoimage Where All Z Values Equal 126 meters

[7] Pixels brightness portrays features with different surface material. Shadows from illumination of the scene by sunlight are seen within MSI, but they are absent from the DEM raster of LiDAR terrain heights.

Figure 13 shows the Raster Dataset Properties, for the orthoimage formed from constant elevation values, that are used to form a fishnet of uniform conjugate polygon shapes for each cell of both the input DEM raster and the output orthoimage. The fishnet is then spatially joined with the LiDAR terrain heights to find the maximum Z value from the points within each polygon shape that represents a cell of the DEM raster. The orthorectification process uses a single Z value located at the centroids of the fishnet for the DEM raster cells. This means that a set of Z value within each DEM raster cell needs to be reduced into a single point with a maximum Z value as a terrain height, and with the XY position at each centroid in the horizontal coordinate system, for the orthorectification process. The maximum Z value within each DEM raster cell is used to portray the reflective surface of the terrain that is exposed by the MSI sensor. The centroids of each shape or cell are then converted to a DEM raster with the same dimensions as the fishnet. This provides the input DEM raster and output orthoimage that have identical dimensions during any subsequent orthorectification process.

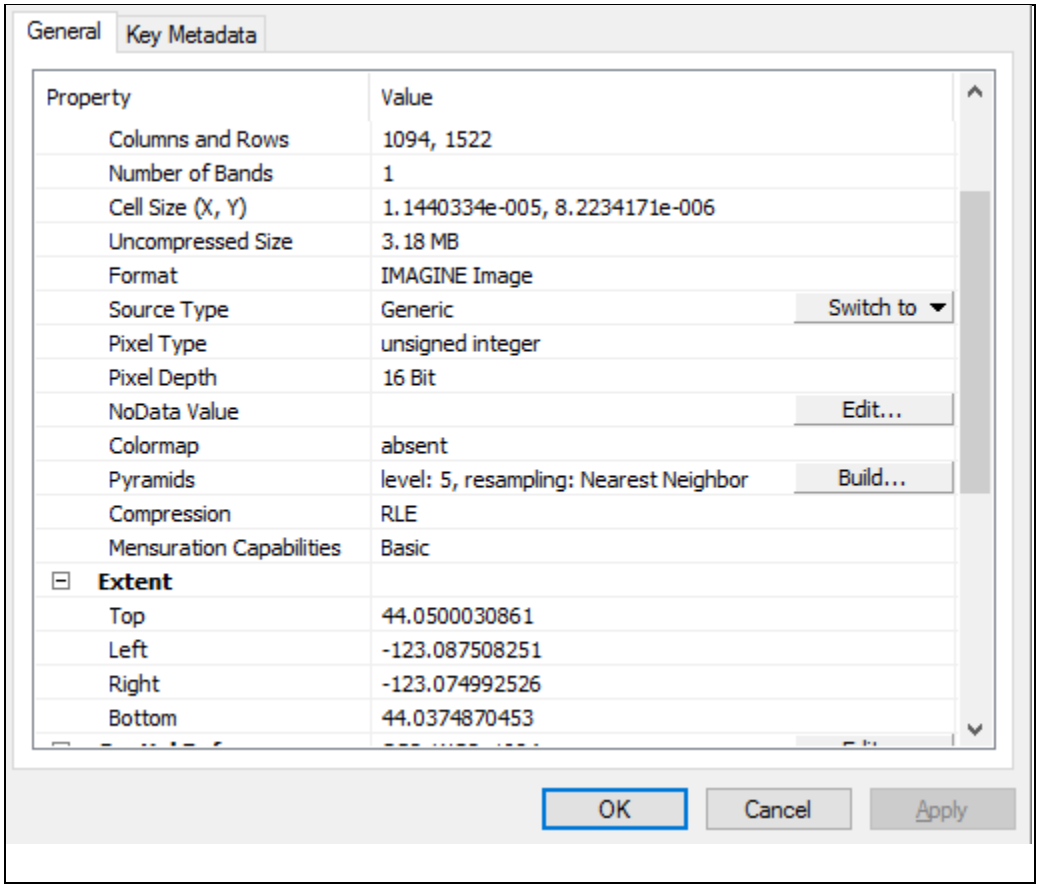

Figure 13: Raster & Fishnet Dataset Properties

Figure 14 shows the formed fishnet overlaid onto an image subset of the DEM raster and the orthoimage formed from a constant terrain height, where each cell for the image of the DEM raster of terrain heights matches a pixel for the orthoimage that was formed presuming flat terrain with a constant DEM raster Z value of 126 meters, so the Z value for most locations in the orthoimage is inaccurate because it is something else besides 126 meters. This causes the subsequent orthorectification processing to have one single terrain height for each pixel of the output orthoimage regardless of DEM raster Z values contained within it. Scattered DEM raster cells lack a Z value because the first return

from a LiDAR is absent from it.[8] The vertical West and South sidewalls to the shown building are visible because they are in the exposed MSI. But it still shows the result of the spatial join between the LiDAR point cloud of terrain heights and the DEM raster fishnet, where each cell contains the maximum Z value of all LiDAR terrain heights within itself.[9] This is an image of the DEM raster that is used to produce the orthoimage from the orthorectification process. And it shows the fishnet of the partially rectified orthoimage from flat terrain with a DEM for a constant Z value of terrain heights.

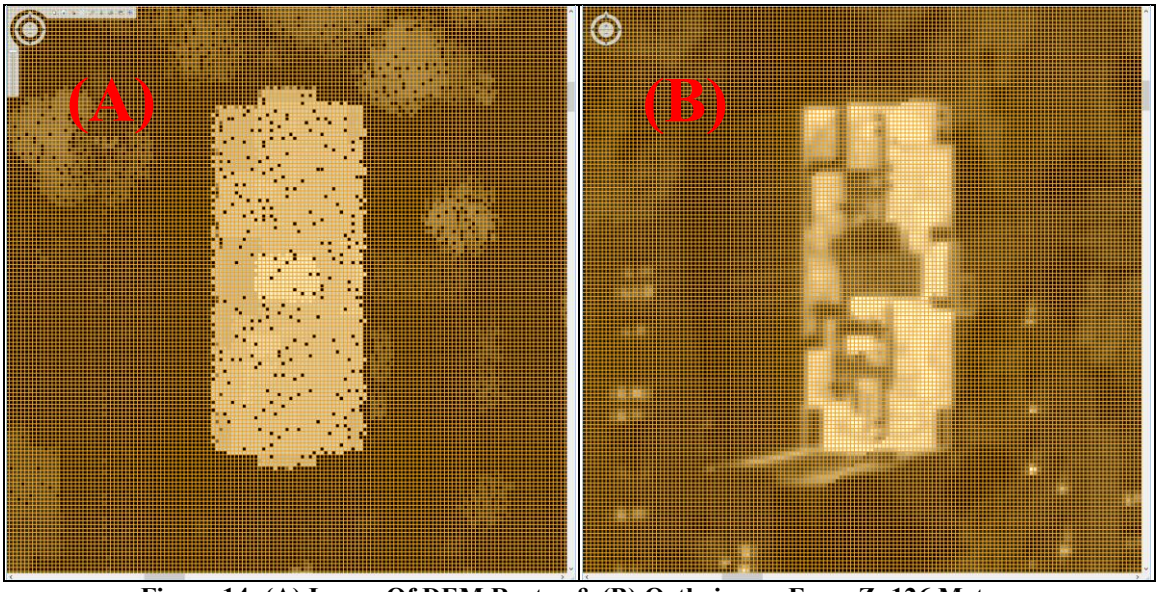

Figure 14: (A) Image Of DEM Raster & (B) Orthoimage From Z=126 Meters

[8] The LiDAR data was originally collected to satisfy a OLC requirement for a DEM raster with 3 feet cells. The cells without a Z value can remain within the DEM raster unless they are filled from a TIN of the surface that has terrain heights, but this is unnecessary for the accuracy assessment of the orthorectification process in this study,

[9] Brighter cells within the image of the DEM raster have higher terrain height Z values compared to the darker cells with lower terrain height.

Figure 15 shows the combined view of the point cloud, where each point has a Z value that depicts terrain height and the fishnet. A spatial join of the point cloud and fishnet forms the DEM raster that has maximum Z value placed at the centroid of each cell. A black dot is placed within a spot from the 2nd-4th return from a LiDAR pulse, where these mostly occur from tree canopies. Only the 1st return spots which are used to find the maximum Z value within each DEM contained within each DEM raster cell. The maximum Z value for each DEM raster cell is misplaced at the centroid of each raster cell instead of it actual position where it was found.

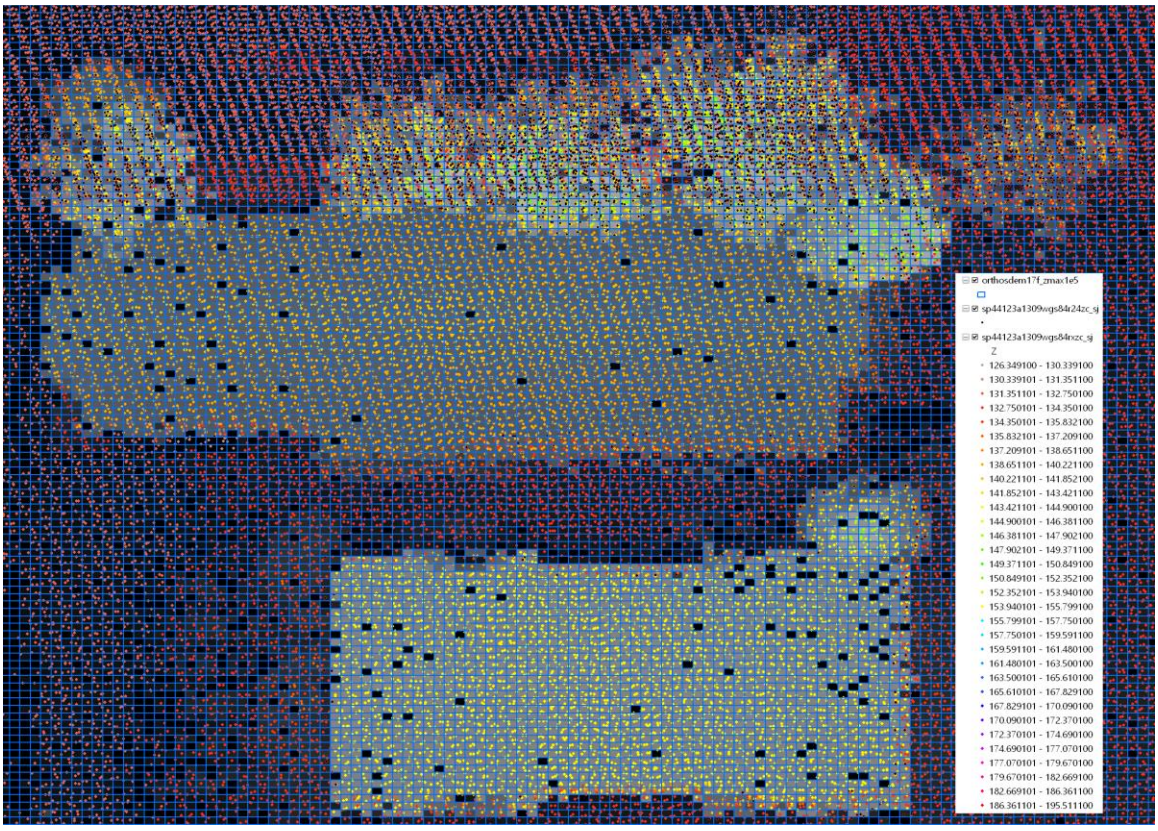

Figure 15:Converting Point Cloud To DEM Raster Of Maximum Z Values

Figure 16 shows where the DEM raster elevation values are finally shifted from the NAVD83-GRS80 Geoid to the WGS84 datum to complete the construction of the DEM raster. Where the orthometric terrain height above the geoid (**H**) equals the ellipsoidal height (h) from Geodetic Positioning Systems(GPS) minus the geoid undulation (**N**) of its separation from the ellipsoid to adjust the Z values between Datums (National Oceanic and Atmospheric Administration - NOAA, 2016). This causes the DEM raster terrain height that is reduced by a constant value of approximately 23 meters for getting the WGS84 ellipsoid height (from GPS) in the orthorectification process, where the range of elevations within the DEM changes from 126-195 meters to 103-172 meters.

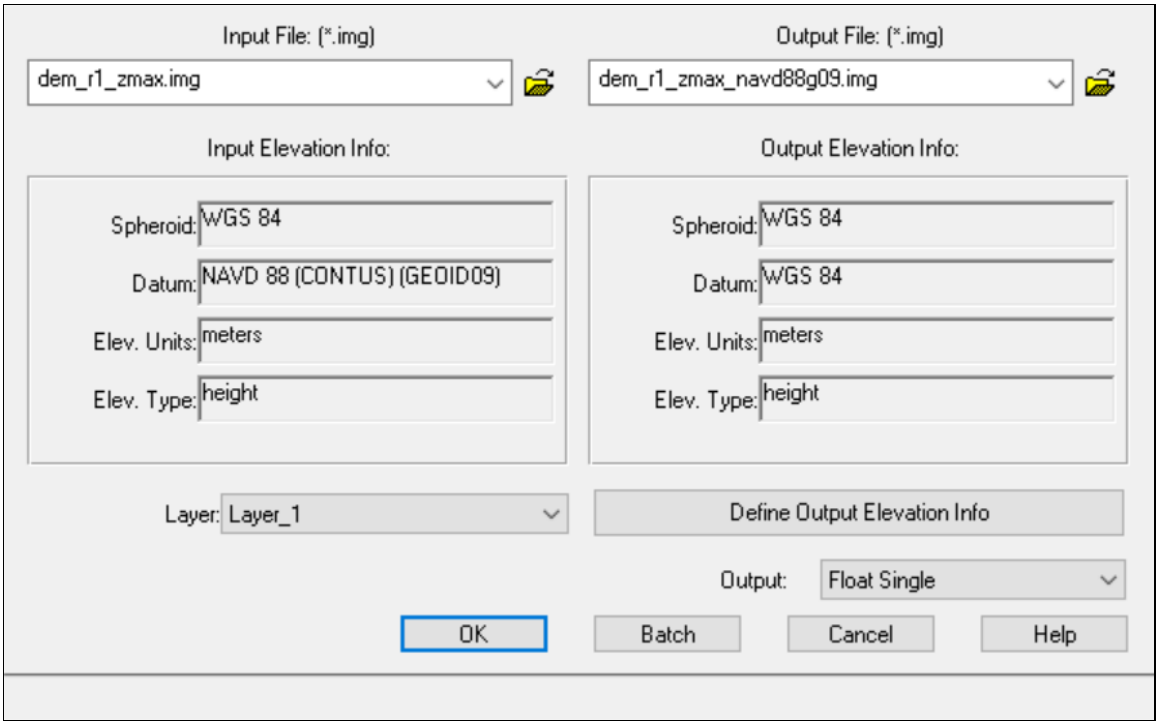

Figure 16: Shifting LiDAR Elevations Between Vertical Datums

The input DEM raster of terrain heights with maximum Z values was therefore constructed so that it can be used as input to the orthorectification process, where it is combined with the input MSI to produce the output orthoimage.

3.4 Conducting Orthorectification

Figure 17 shows the input DEM raster and MSI, that are used for conducting the orthorectification process with Worldview RPC sensor model to produce the output orthoimage.

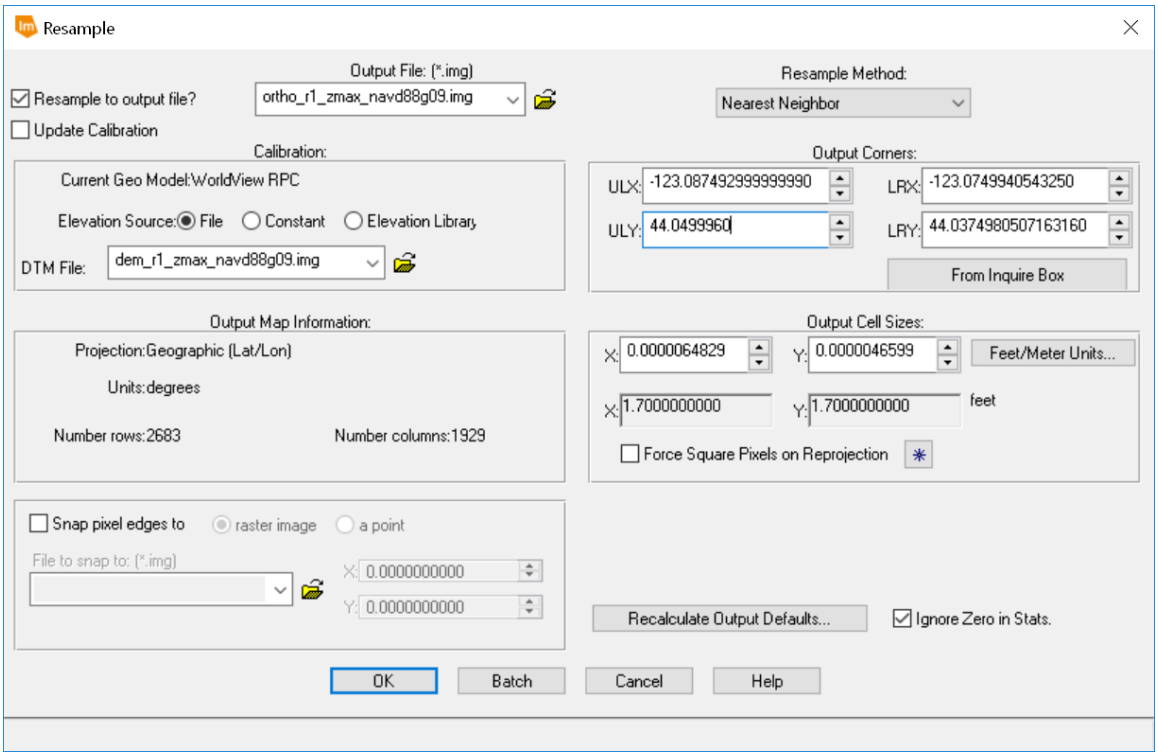

Figure 17: Orthorectification Input & Output Parameters

Figure 18 shows the top (A) MSI orthophoto produced from the bottom (B) DEM raster for the whole study area.

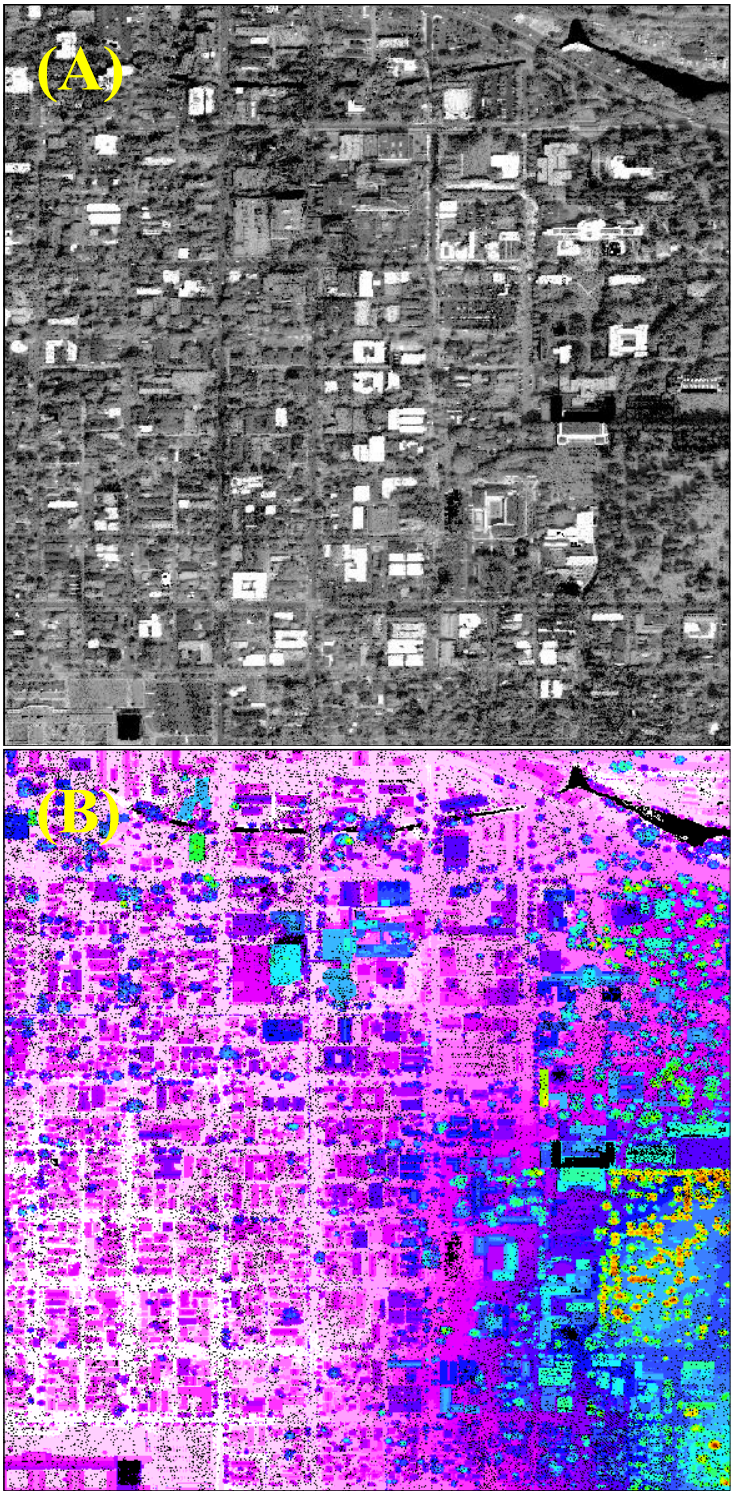

Figure 18: (A) Output Orthoimage & (B) Input DEM Raster

CHAPTER FOUR

4.1 Assessing Orthoimage Accuracy

The accuracy of the output orthoimage is affected by the error from both the DEM raster and sensor model that is propagated throughout the orthorectification process. One approach for assessing the accuracy of the orthorectification process is to measure relative positional offsets between conjugate features within the image of the Digital Elevation Model (DEM) raster and from the output orthoimage. An additional approach is to recognize undesirable rendering anomalies that might occur during the orthorectification process. The measurements of relative positional inaccuracy error are made after ignoring the rendering anomalies, then the systematic and random error throughout the scene is described. Much of this error from the relative positional inaccuracy finally will be measured then reduced between the image of the DEM raster and the orthoimage.

4.2 Output Rendering Anomalies

Undesirable rendering anomalies are visible within the orthoimage produced from the orthorectification process that uses the entire DEM raster of LiDAR terrain heights for Z values, because there is double exposure of rooftops that are called a feature ghost which appear in the output orthoimage nearby elevation discontinuities within the DEM raster. Manmade construction such as sidewalls of buildings cause these cliffs in the terrain

surface that occlude or obstruct the perspective view of the sensor LOS from exposing some portions of the terrain surface. Feature ghosts appear within the output orthoimage when the orthorectification process is unaware when the sensor Line-of-Sight (LOS) intersects the surface of terrain heights more than once, wherein that the same group of pixels from the original unrectified Multi-Spectral Imagery (MSI) cast onto the orthoimage becomes a double image of a feature instead of it being labeled as an area that is unseen because the sensor LOS due to occlusion found that pixel at a higher terrain height in the DEM raster. Related concerns were expressed in the literature at least 10 years ago, so the feature ghost and occlusion problems are overdue for resolution within conventional orthorectification processing (Gunay, et al., 2007; Zhou, et al., 2005; Thorpe, 2001; Jensen, 1995; Ager, n.d.).

Figure 19Figure 19 shows the orthoimage in the top frame (A) and the image of the DEM raster in color to enhance its contrast in the bottom frame (B) produced through the same orthorectification process applied to the original unrectified MSI. This for one of several cases throughout the entire site, when there are abrupt elevation discontinuities along the edge of this rooftop for the building that is 30 meters tall. The orthoimage of the real rooftop is within the outline of it from within the DEM raster, but a portion of the rooftop reappears as a feature ghost nearby in the orthoimage. The smaller rectangle extending from the east side of the building is covered by the ghost feature, but it was unexposed in the original unrectified MSI anyway. The study site was chosen to include an urbanized landscape that typically contains a larger frequency and magnitude of elevation discontinuities compared to natural terrain.

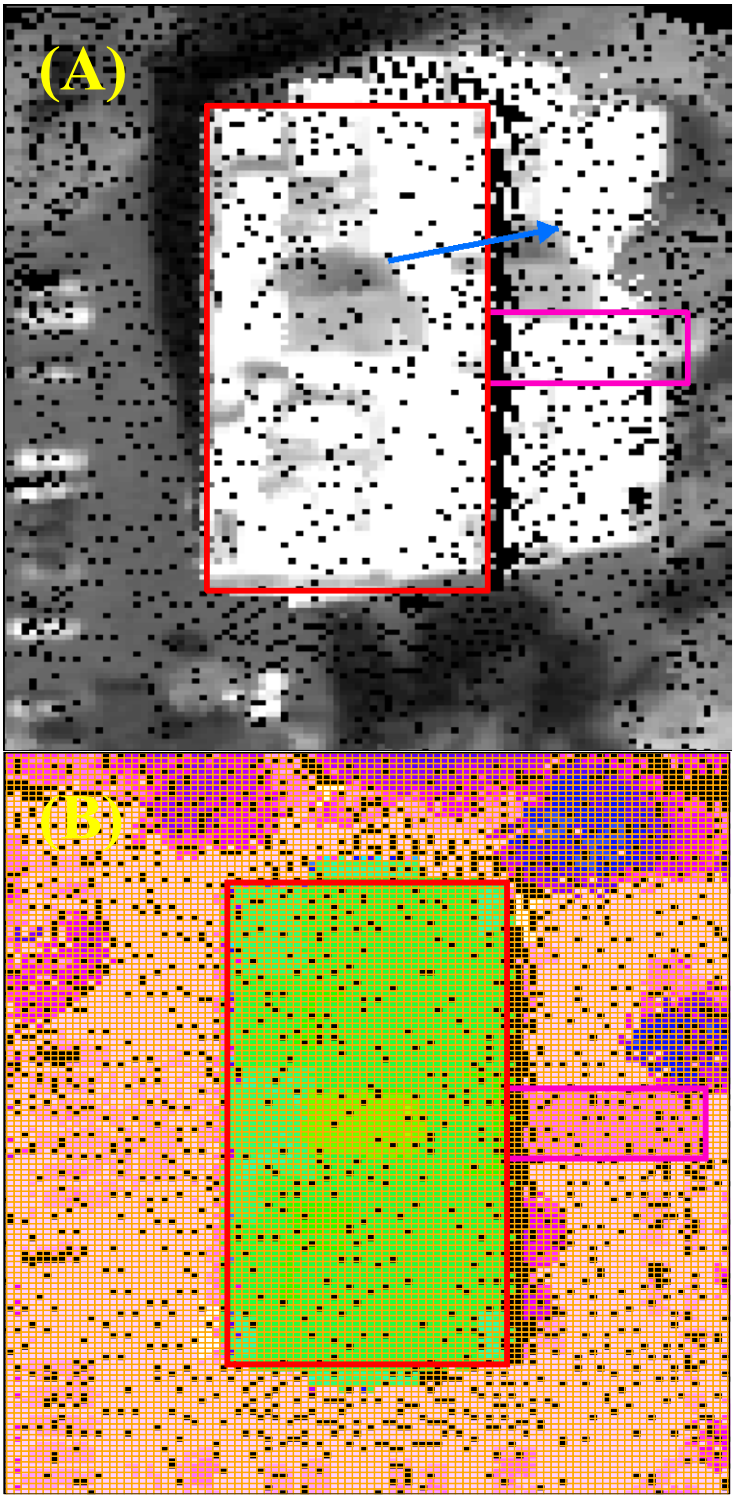

Figure 19: (A) Orthoimage Rooftop Ghost & (B) DEM Raster Z Values

More cases of the feature ghosts are present in the scene even though the actual feature already is placed within the output orthoimage. These feature ghosts are nearby the edges of actual rooftops where significant elevation discontinuities exist. More examples of these rooftop feature ghosts are shown in the appendix. These rooftop ghosts reflect gross inaccuracy from current conventional orthorectification practices. They are a distraction to the orthoimage accuracy assessment when trying to determine the relative positional error between a conjugate feature that is within both the image of the DEM raster and the output orthoimage

Figure 20 shows the perspective projection geometry along the coplanar triangles with radial bases in three-dimensional space from the perspective view of the sensor Line-of-Sight (LOS). The sensor LOS frequently cannot see all facets of the terrain surface within the exposed image, when there is a large elevation discontinuity of Elevation ($\mathbf{E_1}$) minus Elevation ($\mathbf{E_0}$). It is called "occlusion" when facets of the terrain surface are unexposed within the sensor image. The red and green bar are exposed on the image plane, but blue bar is unseen on the image plane. The solid green bar for the terrain surface is the only desirable feature to be seen in the orthoimage. The blue bar cannot be seen on the sensor image plane, so the conventional orthorectification process that remains unaware of the occlusion can put a green and blue dashed of the feature ghost into the output orthoimage.

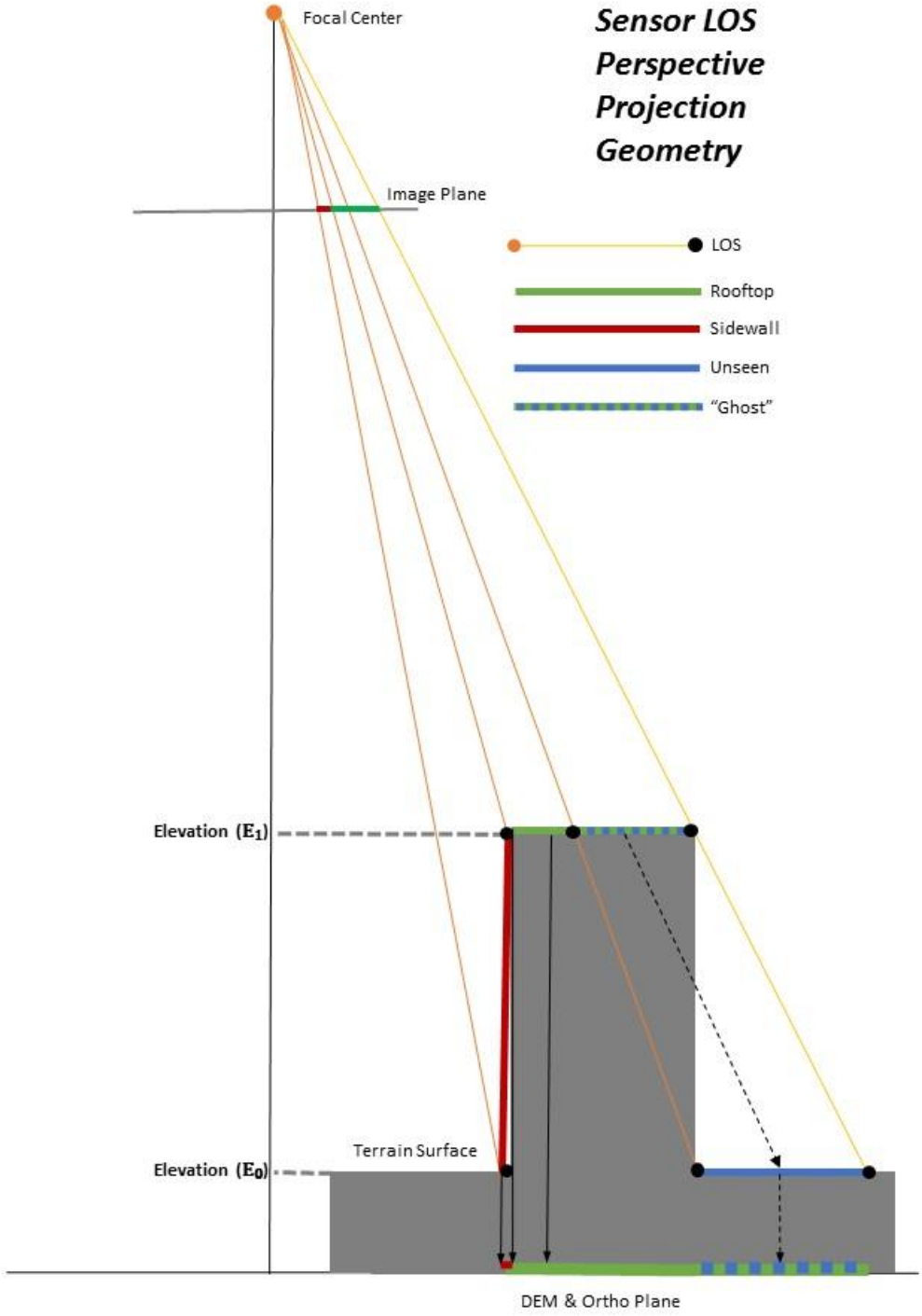

Figure 20: Sensor LOS Occlusion & DEM Feature Ghosts

The cliffs shown earlier within Figure 20 could be vertical sidewalls of buildings getting exposed within the sensor image plane, and these some trace of these vertical cliffs might be cast into the output orthoimage as an indistinct object. These cliffs exist when there is a large range of elevations values throughout a DEM rater cell, except that a completely vertical cliff cannot exist within DEM raster due to the higher elevation $\mathbf{E_1}$ being in one pixel but the lower elevation value is in an adjacent pixel, where the elevation discontinuity exists somewhere unknown within the DEM raster cell with the highest $\mathbf{E_1}$ value. This also means that the acute angle of the vertical cliff to the ground plane is $\boldsymbol{tan}^{-1}\left({}^{\mathbf{E_1}-\mathbf{E_0}}/_{\mathbf{GSD}}\right)$ instead of the actual 90-degrees for this example in Figure 20Figure 1, and for most vertical sidewalls of buildings.

A simple method to remove feature ghosts from the output orthoimage, that can be fit into retrofitted existing software of current image processing systems, is described in the next chapter. But implementing it is beyond the scope of this thesis.

4.3 Accuracy Assessment Results

The results from the measured relative positional inaccuracy between conjugate features found within both the DEM raster and orthoimage are described next. Rooftop objects will be measured when assessing the accuracy of the orthorectified MSI within this study, partly because they are more easily recognized within the image of the DEM raster and the output orthoimage because of elevation discontinuities along building sidewalls. Other applications exist to segment both the DEM or MSI into objects for measuring relative positional inaccuracy but they are beyond the scope of this study (Heidemann, et al., 2012; Gonzalez & Woods, 2008) Only rooftops are measured for this

accuracy assessment because they also are construction that are more permanent landscape features compared to seasonal objects in natural terrain. The feature ghosts of rooftops cast into the output orthoimage are ignored during the accuracy assessment. Further measured rooftops are shown in the Appendix, including the example that is shown next where its feature ghost was shown earlier.

Figure 21 shows the original unrectified building that was shown earlier in Figure 14. Except that the image of the DEM raster is shown underneath it, where it obvious that the original unrectified rooftop is misplaced because a constant Z value was used to produce the image.

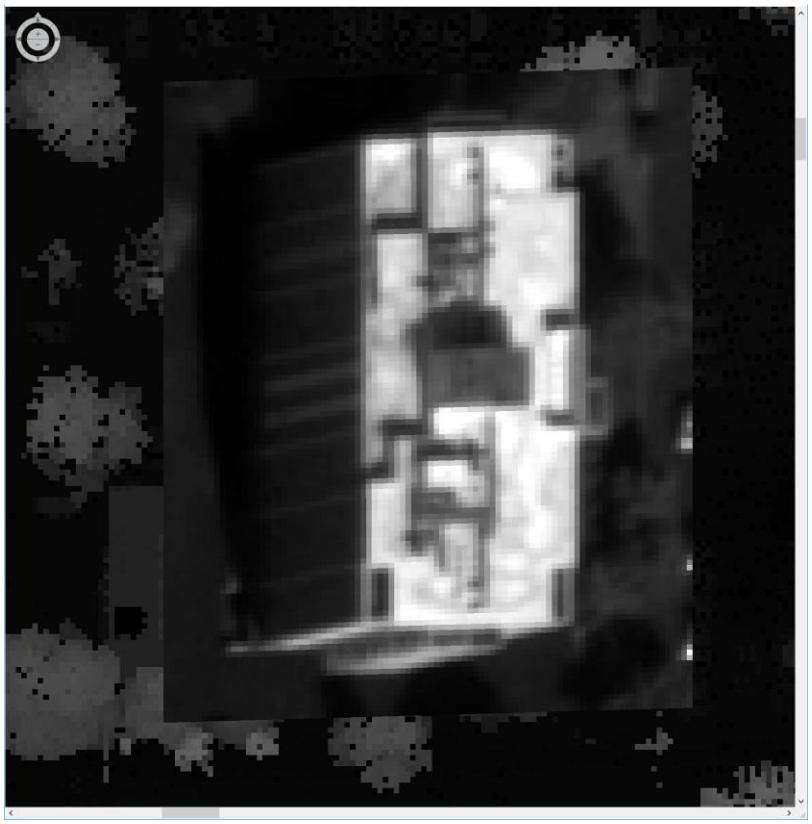

Figure 21: Original Unrectified MSI Building

Figure 22 shows the (A) image of the DEM raster and the (B) output orthophoto. The outline of orthoimage pixels is visible on both images, then only the DEM raster Z value within that outline can be used to assist the measuring of shifts between conjugate features within the image of the DEM raster and within the output orthophoto. Matched points between the conjugate images, and each DEM raster cell outline, allow distinct counting of the pixel offsets between the DEM raster and the orthoimage across the rooftop. It appears to be a constant northerly (Y direction) offset of four pixels (+6.8 feet) and easterly (X direction) offset of one pixel (+1.7 feet) from the DEM to the output orthoimage throughout this entire rooftop. More than a trace of south sidewall for the building still exists within the orthoimage.

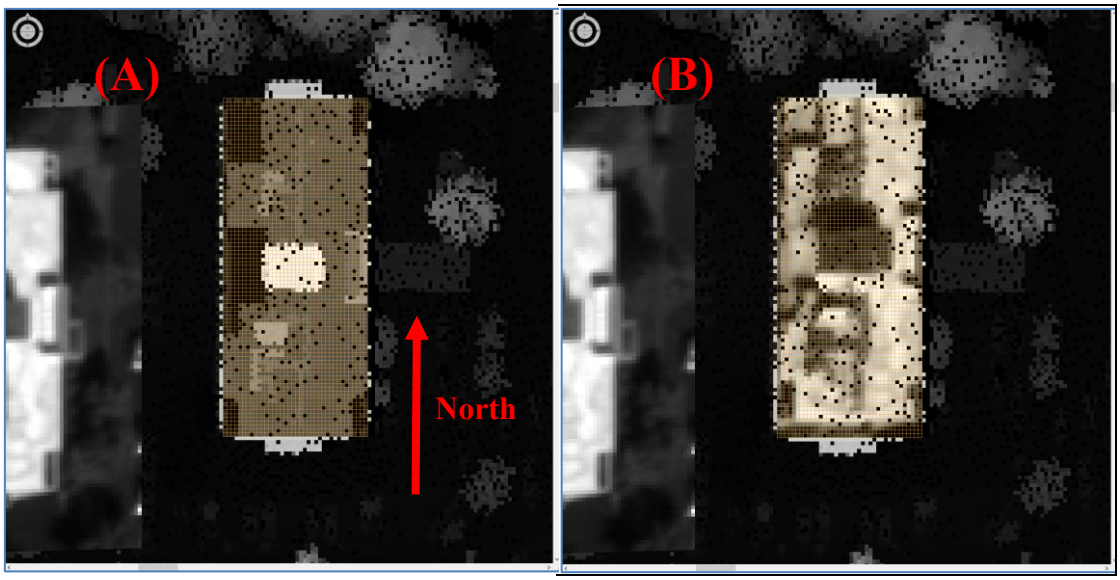

Figure 22: Comparing (A) DEM Raster & (B) Output Orthoimage

Table 2 shows the results from measuring the offsets between the image of the DEM raster and the orthoimage for additional building rooftops throughout the study area, while ignoring the feature ghosts. This includes Rooftop ID Case A shown earlier. The value of pixel offsets (shift) in the X and Y directions is a consistent predominate offset of a 1-pixel shift in the X direction and a 4-pixel shift in the Y direction when showing the mode of the measurements regardless of the building height.

Table 2: Orthoimage Rooftop Offsets

Rooftop ID (Case)	Building Height (meters)	X Shift (pixels)	Y Shift (pixels)	X Shift (feet)	Y Shift (feet)
0820 (A)	30	1	4	1.7	6.8
0150 (B)	9	0	4	0.0	6.8
0170 (C)	11	1	4	1.7	6.8
0180 (D)	8	1	5	1.7	8.5
0190 (E)	10	1	5	1.7	8.5
0200 (F)	6	1	4	1.7	6.8
0360 (G)	1	0	4	0.0	6.8
0520 (H)	5	1	5	1.7	8.5
0570 (I)	9	1	4	1.7	6.8
0642 (J)	14	1	4	1.7	6.8
0860 (K)	12	1	5	1.7	8.5
Mode		1	4	1.7	6.8

The shift of the orthoimage rooftops happens along with the sidewall being placed on the West and South sidewalls of all buildings within this study area. But shifting the orthoimage instead of the DEM raster would retain the unwanted images of the sidewalls for the buildings. The alternative was to first shift the DEM, another new orthoimage was

produced from the shifted DEM, and then the produced orthoimage was shifted back to where the original DEM raster stood before shifting.

Figure 23 shows how a new orthoimage was produced again by using the same DEM raster that was shifted the same amount and directions as the mode of the measured offsets between the DEM raster, to see if the sidewalls of buildings were removed from the new orthoimage produced from the shifted raster.

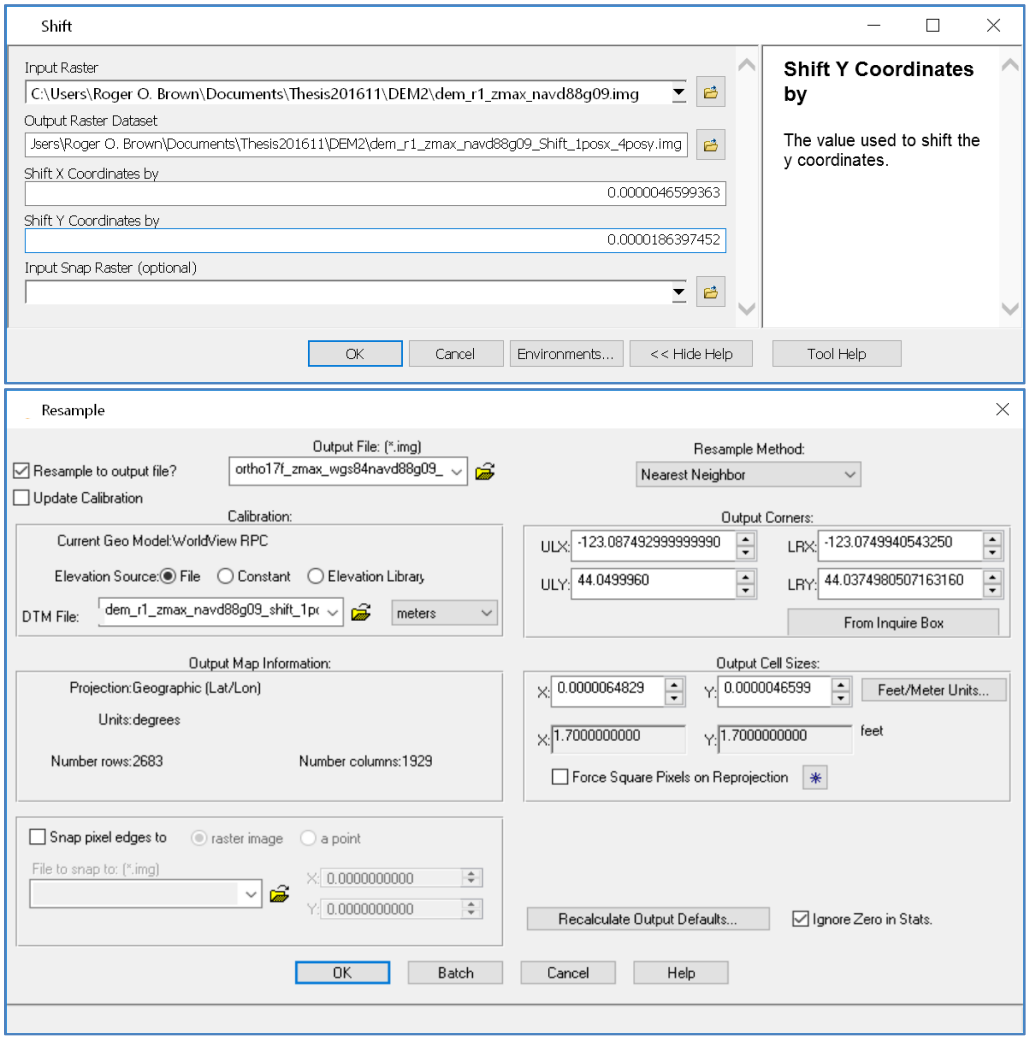

Figure 23: Produced Orthoimage From Shifted DEM

Figure 24 shows that the (A) new orthoimage that is produced by using the shifted DEM raster compared to the (B) old orthoimage produced from the original DEM raster. The new orthoimage removed the south and west sidewalls visible in the lower original orthoimage. But the new orthoimage needs to be shifted back to where the (B) original DEM raster is. This DEM shift beforehand seems to have shifted the sensor LOS just enough to keep it from finding sidewalls again that were exposed in the original unrectified MSI. And the new orthoimage now captures the north side of the rooftop that is missing from the original orthoimage produced from the unmoved DEM, without visible sidewalls.

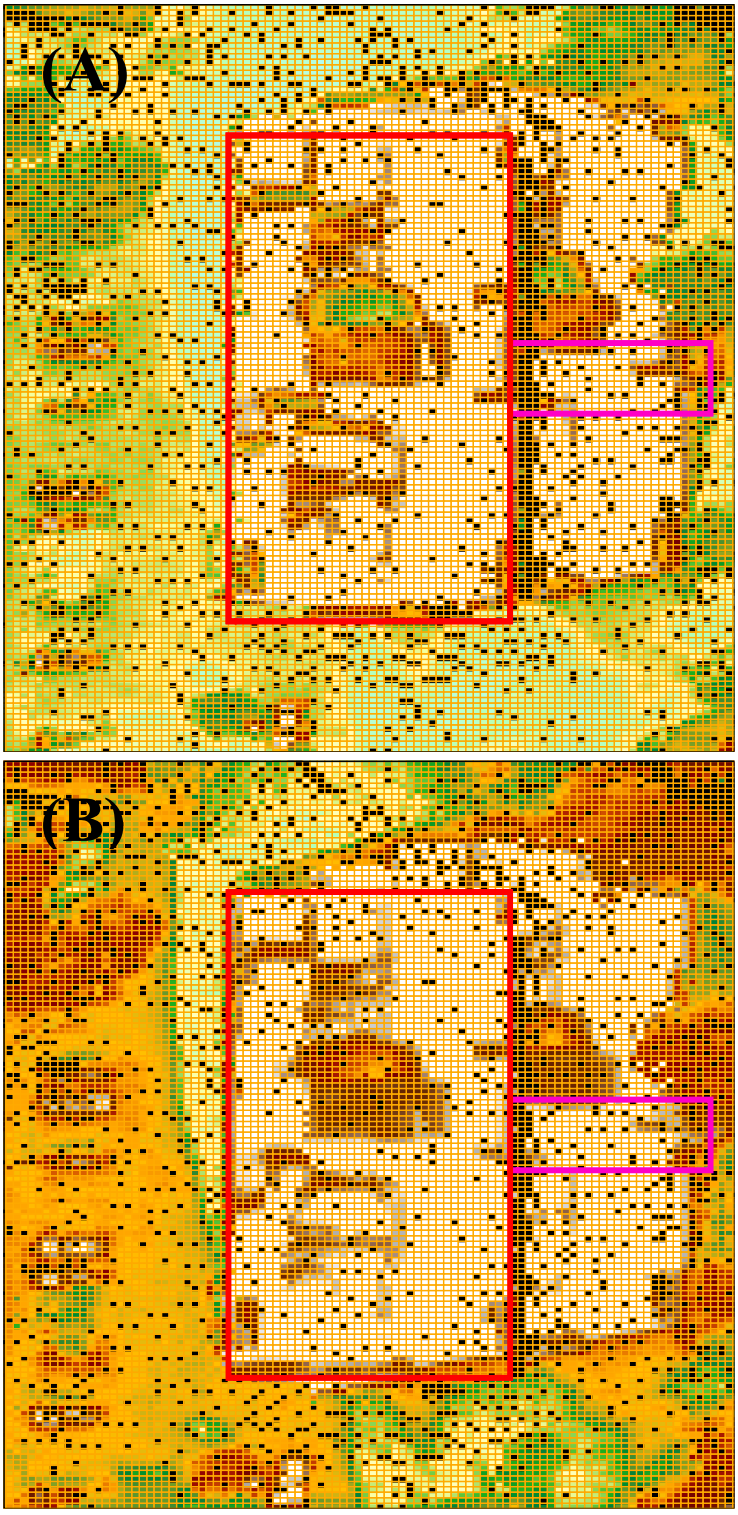

Figure 24: (A) Orthoimage From Shifted DEM Compared To (B) Original Orthoimage

Figure 25 shows how the new orthoimage matches the image of the unmoved DEM raster after the sidewalls were removed from it by using the shifted DEM raster, then the new orthoimage was shifted back to where the DEM was shifted from. This new orthoimage was produced with the shifted DEM from the measured relative positional error previously, then it was shifted back to the old DEM position that now matches the image of the DEM raster better. The entire orthorectified rooftop now matches the DEM raster, without the building sidewalls exposed in the original unrectified DEM in the next example.

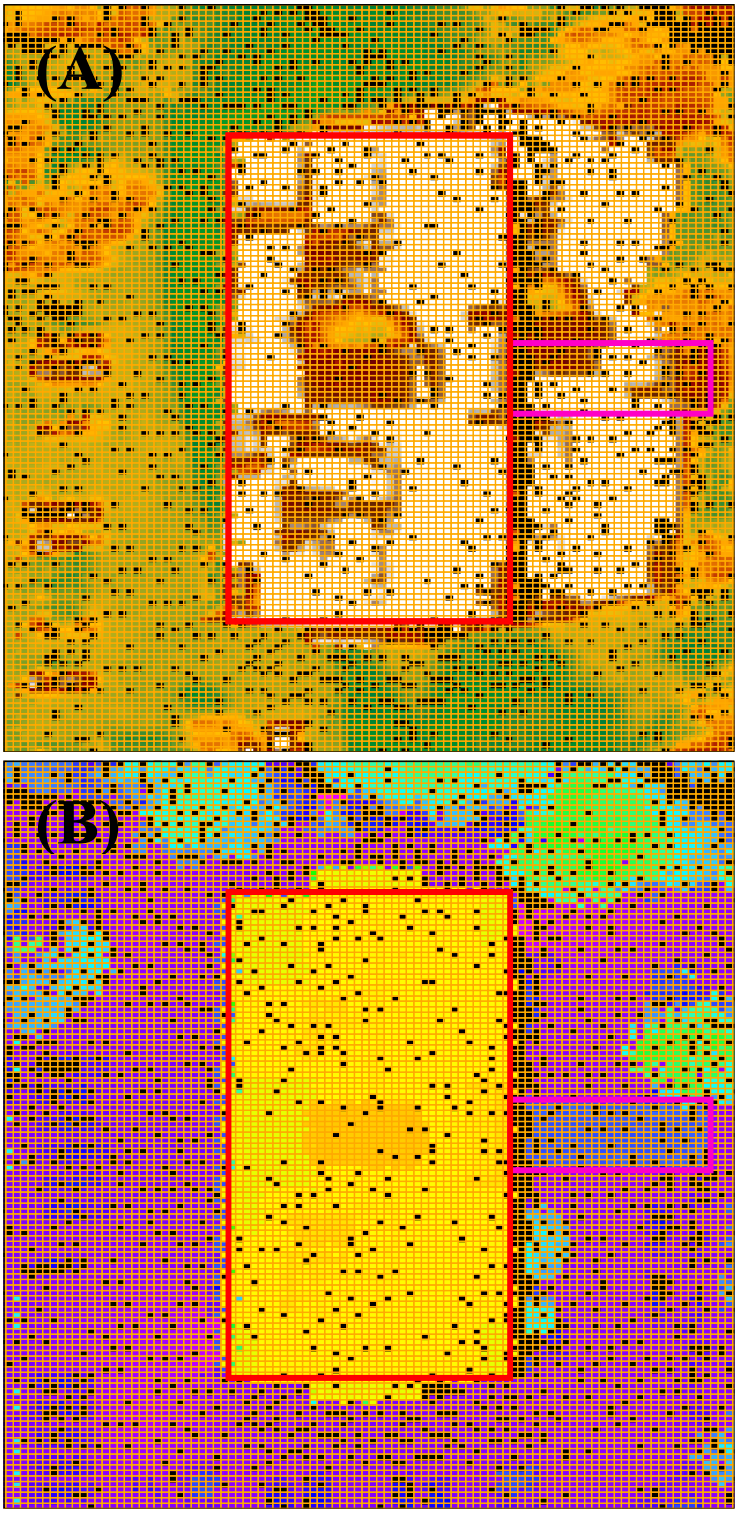

Figure 25: (A) New Orthoimage After Counterposed Shift Back To (B) DEM Raster

Figure 26 shows the results within the overall final orthoimage between the image of the DEM raster and the final orthoimage produced from it, after the counter posed shift of the new orthoimage back to the position of the original DEM before it was shifted. The ghost features remained within the orthoimage, and they were ignored anyway when measuring rooftop offsets between their actual outlines seen within the image of the DEM raster and the orthoimage. There were edges within the outlined area of every rooftop the segmented each image into bright and dark regions, for example peaks of rooftops or additional features on the rooftop to match the two image together. The shifts between the orthoimage and the image of the DEM were measured by zooming into each rooftop case highlighted with a red outline to see the resulting shift between the image of the DEM raster and the orthoimage produced from the orthorectification process. A review of the overall new orthoimage shows that the offsets between the rooftop outlines in image of the DEM and in the final orthoimage have disappeared along with the sidewalls for their buildings, but the feature ghosts remained.

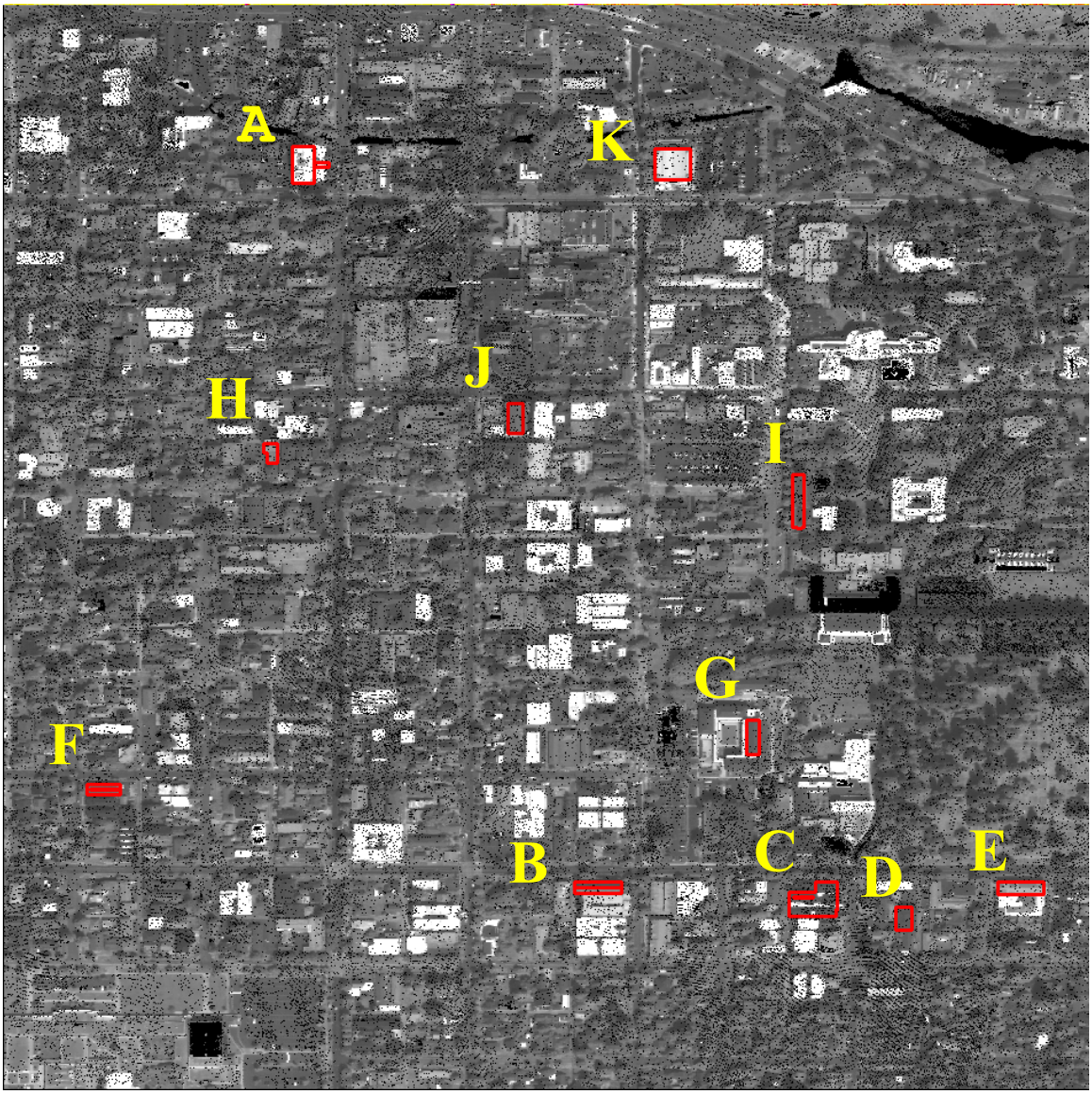

Figure 26:Matched Refined Orthophoto (Case A-K) &DEM Raster

A method to remove the relative positional shifts between the LiDAR DEM and the output orthoimage was developed. This additional effort to refit a refined orthoimage to the original image of the DEM raster, after completing the conventional orthorectification process, should ensure better registration between both datasets that benefits further combined spectral and terrain reasoning methods.

CHAPTER FIVE

5.1 Conclusion

This conclusion follows from the accuracy assessment in the previous chapters for the orthorectification process that uses a LiDAR Digital Elevation Model (DEM) of terrain heights to produce the Multi-Spectral Imagery (MSI) orthoimage with a Rational Polynomial Coefficients (RPC) sensor model. The overall bearing of this study was that conventional orthorectification processes should be adjusted to compensate for the increased spatial resolution of the DEM and the MSI especially in urbanized landscapes. This accuracy assessment that compares the image of the input DEM and the output orthoimage rejects the hypothesis of this study where the "MSI orthorectification produces adequate registration of the input DEM raster with the output orthoimage that is sufficient for combined spectral and terrain reasoning" research in the future. This hypothesis is rejected unless feature ghosts are removed from the orthoimage, and until the relative positional inaccuracy (that might remain after completing the initial orthorectification process) is reduced between the DEM raster and output orthoimage.

This study discovered two major sources of error during the orthorectification process. The primary contribution of this thesis was that it successfully developed a method to measure and correct systematic relative positional inaccuracy that is found after producing the initial orthoimage, without dwelling on the sources of error before

and during the orthorectification process. It recognizes relative positional inaccuracy of systematic displacement between conjugate features in the LiDAR DEM and the output orthoimage. This inaccuracy is produced by the conventional orthorectification process regardless of the sensor model. This method was successful to assess and correct for relative positional inaccuracy between the DEM and initially produced orthoimage after completing the orthorectification process. This can be implemented immediately to monitor the results of any orthorectification process. It describes and corrects for systematic error without explaining why the relative positional inaccuracy exists, but it is a prudent practice of quality control for orthoimage production presuming that the raster of terrain heights is correct except for systematic error that exists within it. The second contribution of this study is that it identifies the feature ghosts produced within the output orthoimage from the conventional orthorectification process.

Employing the suggested solutions from this study should improve current orthorectification practices, by resolving the described potential orthoimage inaccuracy within current geographic information and image processing systems. This study discovered a method to refit the DEM and a reproduced orthoimage back together after the initial orthorectification process completes. It also proposes using a list of point XYZ coordinates, with Z values sorted from higher to lower terrain heights during the orthorectification process, to remove feature ghosts from the output orthoimage. Where this is proposed and described later in this chapter. Resolving this projective and perspective geometry dilemma of feature ghosts during the orthorectification process is beyond the scope of this study however.

Using the first solution now, and implementing the second solution later, should then further inspire emerging efforts for combined spectral and terrain reasoning by accepting instead of rejecting the hypothesis for this study. The limitations of this study follow. Then the current and future advantages to implementing the solutions described within this thesis concludes this study.

5.2 Limitations

This study described two major sources of error during the orthorectification process. The successful reduction of the relative positional inaccuracy between the refined orthoimage and the horizontally shifted DEM raster used to produce it, and that solution can be implemented immediately. But the practice to remove relative positional inaccuracy presumes that feature ghosts already are absent from the output orthoimage This study also describes the feature ghosts, then it only proposes a method to prevent the problem during the orthorectification process. A method proposed later in this chapter to prevent rendering anomalies of orthoimage feature ghosts requires implementation elsewhere.

Another limitation of this research is that the DEM raster GSD should match the nominal GSD of the MSI pixel footprint to minimize the spatial and spectral difficulties when sampling the original unrectified MSI. The other limitation is that there could be a large temporal difference between the DEM and the MSI, where the terrain surface can change during the time lag between DEM collection and MSI exposure. The LiDAR data was collected two years before the original unrectified MSI was exposed in the Summer of 2011. Moving or parked vehicle positions will change, and a vegetation canopy from

trees or crops might change seasonally or annually regardless of the time lag for example. The DEM and MSI could be collected concurrently from the same aerial platform that is required for collecting the LiDAR. But the simultaneous collection of the LiDAR DEM and the MSI might be impractical or too expensive, unless the project demands simultaneous collection of the DEM and MSI. The uncertainty about the source data used to compute the RPC provided with the MSI was another limitation of this study.

Feature ghosts remained within the reproduced output orthoimage, even after removing the systematic relative positional inaccuracy from the initial orthoimage. This study might discourage using the orthoimage for combined spectral and terrain reasoning, until the current undesirable output rendering anomalies of feature ghosts are removed from output orthoimages produced by existing geographic information and image processing systems that employ conventional orthorectification processing methods. This leads to a proposed solution to remove feature ghosts from the output orthoimage that is described later within this chapter.

Figure 27 shows that the MSI chosen for this study spanned 208 partial or complete sites with 0.75 by 0.75 arc-degree dimensions (0.0125 decimal degrees). Each complete site contains approximately 10 million LiDAR points. A single site was chosen for this study that is highlighted with a blue outline, because the massive data volume strained limited desktop computer resources available for this study. Parallel processing machines, or a software script, might be able to handle more than one sample site at a time for statistical comparison of accuracy assessment results throughout the entire image frame that contains various types of terrain.

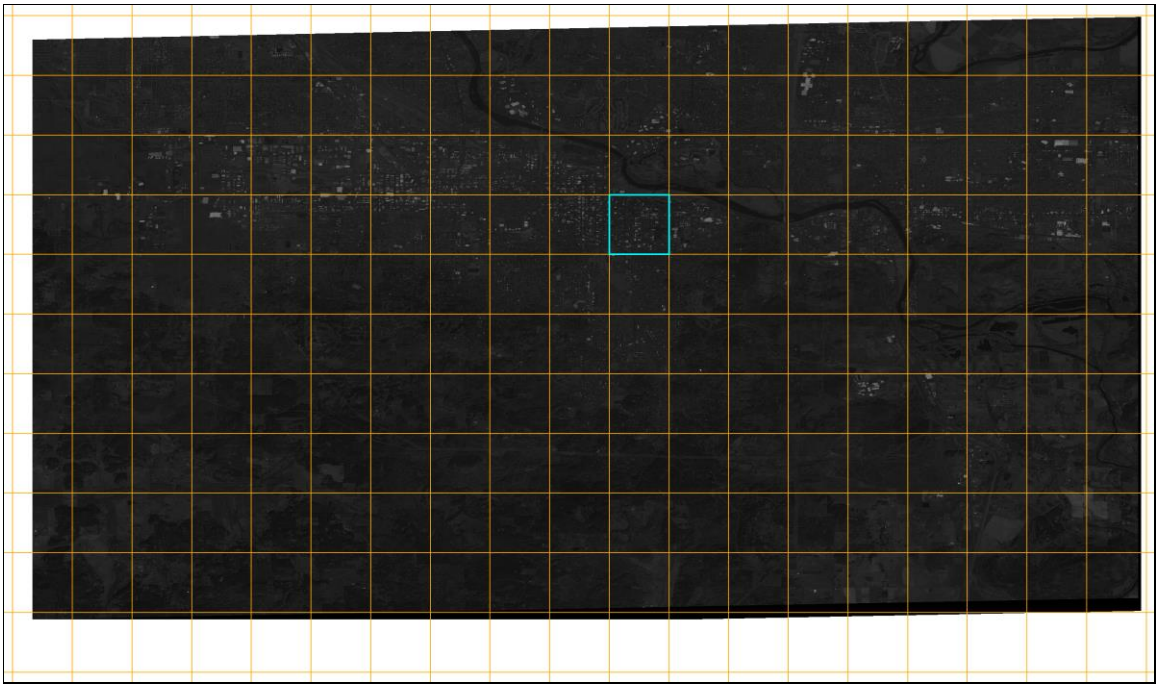

Figure 27: MSI & LiDAR Data Spans

Further studies could expand the scope of this thesis to give a more robust accuracy assessment of the orthorectification process.

5.3 Current Impacts

The work presented within this thesis identifies inaccuracy within the conventional orthorectification process, particularly when orthoimages are produced with reduced interpolation of terrain height values within urbanized landscapes (cityscapes) that contain a pronounced frequency and amplitude of elevation discontinuities along the reflective terrain surface. The problems become more apparent as the spatial resolution continually increases for the DEM and the MSI technology. The production practice for relative positional inaccuracy reduction can be implemented immediately, but the proposed solution orthoimage feature ghost removal must be accepted first, and then it

can be implemented later. Both producers and consumers should exercise caution given the potential problems within orthoimage products that were identified in this thesis.

5.3.1 Relative Positional Inaccuracy Reduction

A method was developed and described within the previous chapter to successfully measure and reduce relational positional inaccuracy between the DEM and output orthoimage. This was done as follows:

(1) Shifted DEM horizontally by same magnitude and direction of measured relative positional inaccuracy of the initial orthoimage.

(2) Reproduced a new orthoimage that was formed from the newly shifted original DEM raster.

(3) Performed a counterpoising shift of new orthoimage back to the original DEM raster.

This successful method to measure and remove relative positional inaccuracy between the image of the DEM raster and the initial orthoimage can be easily implemented now. It should become a normal practice regardless of the orthorectification process that is used to produce the output orthoimage.

5.3.2 Orthoimage Feature Ghost Removal

Current image processing systems that use conventional orthorectification processes might produce feature ghosts within the output orthoimage that were described with more detail in the previous chapter, because the product employing the orthorectification process might ignore instances when multiple points in the DEM raster project onto the same MSI pixel. This study suggests the following simple software retrofit that produces the orthoimage one DEM raster cell at time directly from the list of points sorted by

descending Z values, instead of using a DEM raster. This solution is described next, but implementing it is beyond the scope of this study.

The orthorectification process by itself should recognize where feature ghosts might appear within the output orthoimage. These undesirable rendered anomalies should be absent from orthoimages produced by current orthorectification processes. The image processing system that is conducting the orthorectification process should notice when two or more spots in the DEM project into the same MSI pixel, so that the closest spot along the Line-of-Sight (LOS) projective ray is given the pixel brightness value for each MSI layer. This misplacement of feature ghost onto the wrong spot in the DEM can happen because of perspective geometry from the sensor LOS when making an orthoimage regardless of the sensor model that was described earlier in Figure 20, where this adversely affects the spatial accuracy of the orthorectification process. The solution entails recognizing when these feature ghosts might occur, and thereby remove them during the orthorectification process.

Figure 28 shows how the feature ghosts appearing in an orthoimage can be prevented by using a list of XYZ coordinates for centroid points from the DEM raster, when these points are sorted from the highest to the lowest elevation Z value. Where the Z values where later reduced by 23 meters from NAVD88 to reflect the WGS84 vertical datum values.

FID	Shape	Join_Count	TARGET_FID	z1e5	ORIG_FID	POINT_X	POINT_Y	POINT_Z
0	Point ZM	4	420437	19551110	420437	-123.075539	44.038509	195.5111
1	Point ZM	1	422367	19547110	422367	-123.075532	44.038514	195.4711
2	Point ZM	2	420439	19497110	420439	-123.075526	44.038509	194.9711
3	Point ZM	3	418510	19491010	418510	-123.075526	44.038505	194.9101
4	Point ZM	1	418509	19488010	418509	-123.075532	44.038505	194.8801
5	Point ZM	2	422366	19477010	422366	-123.075539	44.038514	194.7701
6	Point ZM	2	422368	19476110	422368	-123.075526	44.038514	194.7611
7	Point ZM	4	418508	19424910	418508	-123.075539	44.038505	194.2491
8	Point ZM	2	420440	19406910	420440	-123.075519	44.038509	194.0691
9	Point ZM	5	424296	19403810	424296	-123.075532	44.038519	194.0381
10	Point ZM	3	2197111	19395010	2197111	-123.075117	44.042801	193.9501
11	Point ZM	7	2199042	19394110	2199042	-123.075104	44.042806	193.9411
12	Point ZM	3	2199040	19392010	2199040	-123.075117	44.042806	193.9201
13	Point ZM	1	2199041	19392010	2199041	-123.075111	44.042806	193.9201
14	Point ZM	1	2197113	19391010	2197113	-123.075104	44.042801	193.9101
15	Point ZM	1	416579	19383110	416579	-123.075539	44.0385	193.8311
16	Point ZM	3	1519809	19381910	1519809	-123.076563	44.041165	193.8191
17	Point ZM	2	1527507	19374010	1527507	-123.07668	44.041184	193.7401
18	Point ZM	1	2200970	19364810	2200970	-123.075111	44.04281	193.6481
19	Point ZM	4	2202898	19363910	2202898	-123.075117	44.042815	193.6391
20	Point ZM	1	1519805	19360010	1519805	-123.076589	44.041165	193.6001
21	Point ZM	1	2202899	19357810	2202899	-123.075111	44.042815	193.5781
22	Point ZM	1	1882661	19357810	1882661	-123.075266	44.042041	193.5781
23	Point ZM	3	1519806	19355110	1519806	-123.076582	44.041165	193.5511
24	Point ZM	3	1880731	19351110	1880731	-123.075273	44.042037	193.5111
25	Point ZM	4	2200969	19349010	2200969	-123.075117	44.04281	193.4901
26	Point ZM	3	416580	19346810	416580	-123.075532	44.0385	193.4681
27	Point ZM	2	416578	19346810	416578	-123.075545	44.0385	193.4681
28	Point ZM	6	1523663	19345010	1523663	-123.076589	44.041175	193.4501
29	Point ZM	4	2200971	19344110	2200971	-123.075104	44.04281	193.4411
30	Point ZM	1	2202897	19341110	2202897	-123.075124	44.042815	193.4111
31	Point ZM	4	1527508	19338910	1527508	-123.076673	44.041184	193.3891
32	Point ZM	3	1519808	19338010	1519808	-123.076569	44.041165	193.3801
33	Point ZM	3	414650	19337110	414650	-123.075539	44.038495	193.3711
34	Point ZM	2	422369	19337110	422369	-123.075519	44.038514	193.3711

Figure 28: DEM Raster Cell XYZ Centroids Sorted By Descending Z Values

Producing the orthoimage from the centroids entails the processing of the DEM raster in the sorted descending order of its “buffered” Z values, instead of from a raster that is sorted in X-columns or Y-rows order, while marking the image pixel with a null value within a copy of the original unrectified MSI after it is cast to the output orthoimage for the first time. That will cause later DEM raster locations with lower Z values from the sensor LOS intersecting the terrain surface to be given that new null value for the marked

MSI pixel, instead using the earlier brightness of the pixel to produce a feature ghost. This process should work when the sensor LOS is nearly vertical because the higher Z values will only be exposed first, instead of needing to measure the slant distances farther along the sensor LOS after it first intersects the terrain surface.

Equation 6 shows this process by using the pseudo code and notation from Equation 1 that was shown in an earlier chapter for going advancing through list of $[\boldsymbol{x}, \boldsymbol{y}, \boldsymbol{z}]_{\boldsymbol{DEM}}$ coordinates that are sorted by descending Z values.

$$\boldsymbol{Sort}\left[\boldsymbol{j}, \boldsymbol{x}, \boldsymbol{y}, \boldsymbol{z}, \left(\boldsymbol{z_j} \geq \boldsymbol{z_{j+1}}\right)\right]$$

$$for\ \boldsymbol{j}$$

$$[\boldsymbol{x}, \boldsymbol{y}, \boldsymbol{z}, \boldsymbol{b_i}]_{\boldsymbol{Ortho}} = \left[\boldsymbol{x_j}, \boldsymbol{y_j}, \boldsymbol{z_j}\right]_{\boldsymbol{DEM}} \rightarrow [\boldsymbol{x'}, \boldsymbol{y'}, \boldsymbol{b_i}]_{\boldsymbol{MSI}}$$

$$if\ \boldsymbol{b_i} \neq \boldsymbol{null}\ then\ \boldsymbol{set}(\boldsymbol{x'}, \boldsymbol{y'}, \boldsymbol{b_i} = \boldsymbol{null})$$

$$\boldsymbol{j} = \boldsymbol{j} + \boldsymbol{1}$$

$$end\ for$$

Equation 6: Orthoimage Produced From Coordinate List Sorted By Z Values

The current conventional orthorectification process can be adjusted in the future by forming the orthoimage using one MSI pixel at a time from the list of centroids for each DEM raster cell sorted by descending Z values, and by replacing pixels in a copy of the original unrectified MSI with a null value immediately after it is first placed into the output orthoimage.

There are many cases of feature ghosts that were shown in the appendix for the edges of rooftops where there are significant elevation discontinuities. The image analyst who is assessing the spatial accuracy of the orthorectification process needs to recognize these

feature ghosts. They need to notice when a conjugate feature in the image of the DEM raster is missing from the output orthoimage because the MSI sensor cannot see it, when the projective LOS between the MSI sensor and DEM raster intersects the terrain more than once. Small traces from a portion of the building sidewalls exposed within original unrectified MSI also might remain within the orthoimage despite the accuracy of the DEM and sensor model during the orthorectification process.

The rooftop ghosts reflect gross inaccuracy from current conventional orthorectification practices. These feature ghosts also are a distraction to the orthoimage accuracy assessment when trying to determine the relative positional inaccuracy between conjugate features within both the image of the DEM raster and the output orthoimage. This misplacement of the MSI groups of pixels onto the wrong spot in the DEM can happen when making an orthoimage, where this adversely affects the spatial accuracy of the orthorectification process. This gross inaccuracy also might cause image misinterpretation or confusion by the producers and consumers of orthoimage products, so the feature ghosts should be removed during the orthorectification process. Orthoimage producers should be wary when using geographic information and image processing systems that ignore these placements of feature ghosts, because they portray gross inaccuracies within the output orthoimage of cityscapes.

This orthoimage inaccuracy with the perspective and projective geometry given the MSI sensor LOS should be removed from the orthorectification process, if only because it confounds the accuracy assessment of the orthoimage. The producers of orthoimage products should remove these rendering anomalies before unaware consumers misuse

them. That would produce more accurate orthoimages. This also could support future research for combined spectral and terrain reasoning methods with accurately registered extra layers or channels that portray terrain surface features such as slope, aspect, roughness, and others during MSI feature extraction that is encouraged from past literature (Campbell & Wynne, 2011, pp. 335-381; Brown, 2013)

5.4 Future Efforts

Future research and development efforts for combined spectral and terrain reasoning methods were introduced in the context of assessing and improving the registration between orthoimages and the DEM raster that produced them. The study within this thesis presents accuracy considerations and recommendations (with a limited volume of data) to enhance continued research about relationships between MSI feature extraction and terrain surface shape descriptions such as slope, aspect, roughness, and others.

Additional efforts to better register the DEM raster and Rational Polynomial Coefficients (RPC) sensor model control points could further reduce the misfits between the DEM and the produced orthoimage. This might include (1) adjusting the point cloud to fit a network of existing control points that perhaps were used to derive the RPC anyway, and (2) refining the RPC using points from the DEM raster, using these resolutions before the orthorectification process begins. These additional efforts might further improve the accuracy assessment when using current technology along with the improvements suggested by this study for the orthorectification process, for anybody dissatisfied about removing latent unexplained error afterwards.

This thesis was done within the context of better registering the thematic map for the landscape, that can be orthorectified from feature extraction within the original unrectified MSI, together with the DEM terrain surface. The gap between conventional orthorectification capabilities and the technology of increasing spatial resolution for both the DEM and the MSI will continue to grow, unless the orthorectification process refined by suggestions within this study. Orthorectification processes and practices should continually evolve to accommodate the increasing spatial resolution for both the DEM and the MSI, regardless if it is the RPC sensor model along with a LiDAR DEM or otherwise.

Appendix

A. Measured Orthoimage Examples

Figure 29 through Figure 39show eleven cases of measured shifts offset the Digital Elevation Model (DEM) raster to the Multi-Spectral Imagery (MSI) orthoimage, including the single case discussed in Chapter Four. The lower part of each figure shows the elevation heights, and the upper part shows the orthoimage brightness, for eleven cases of measured rooftops. False color is used within each image, also different spectrums for the elevations and orthoimage, to clarify their image segmentation for comparing themselves. Each pair of images are a basis for the accuracy assessment by measuring the offset or shift from the DEM raster to the orthoimage. The measurement results are placed within Table 2 previously. These measured cases were used to successfully remove the relative positional error between the refined orthoimage, produced by a shifted DEM, then the refined orthoimage was shifted back to the original DEM raster. This caused good registration between the final orthoimage and the DEM raster with little if any relative positional differences between them.

Figure 29: Comparing DEM & Orthoimage (Case A)

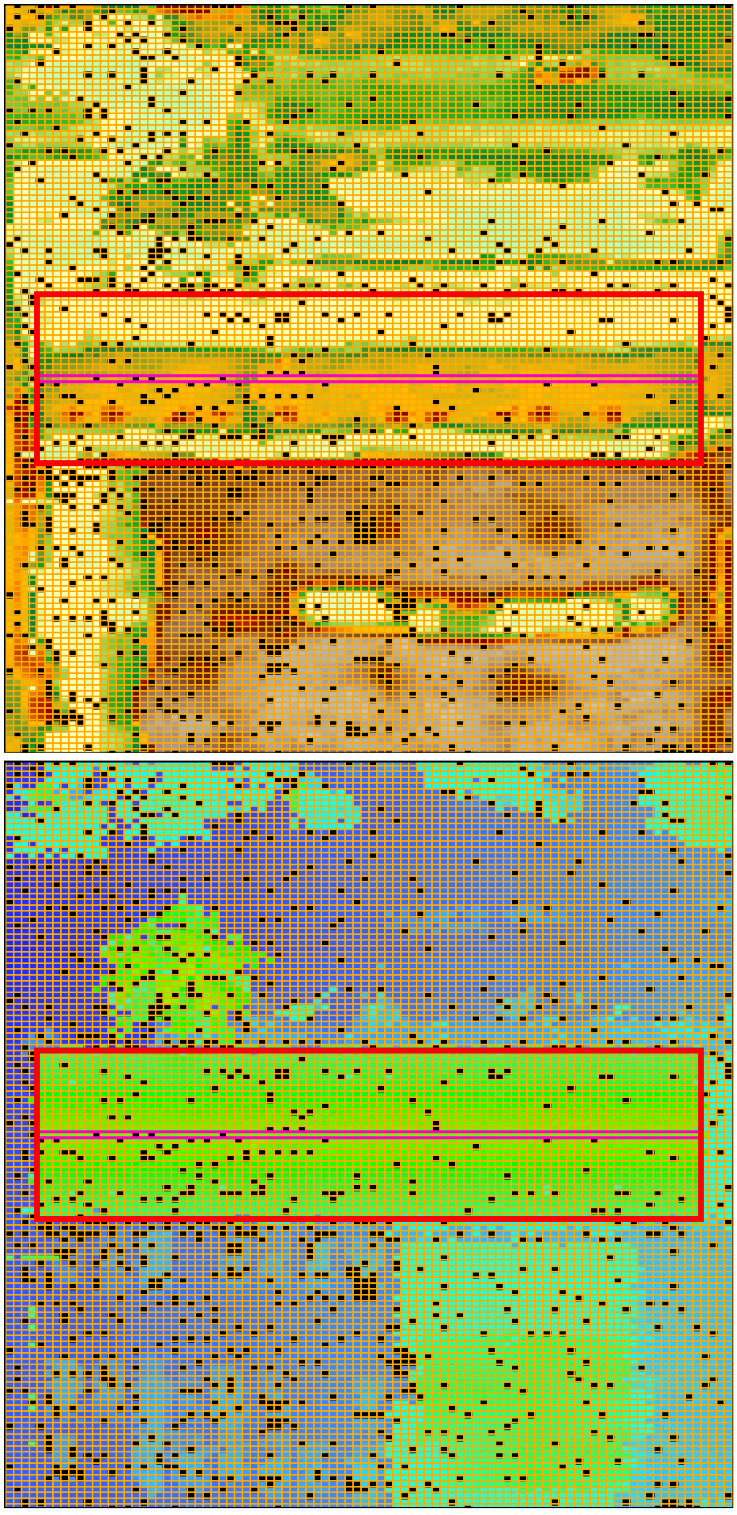

Figure 30: Comparing DEM & Orthoimage (Case B)

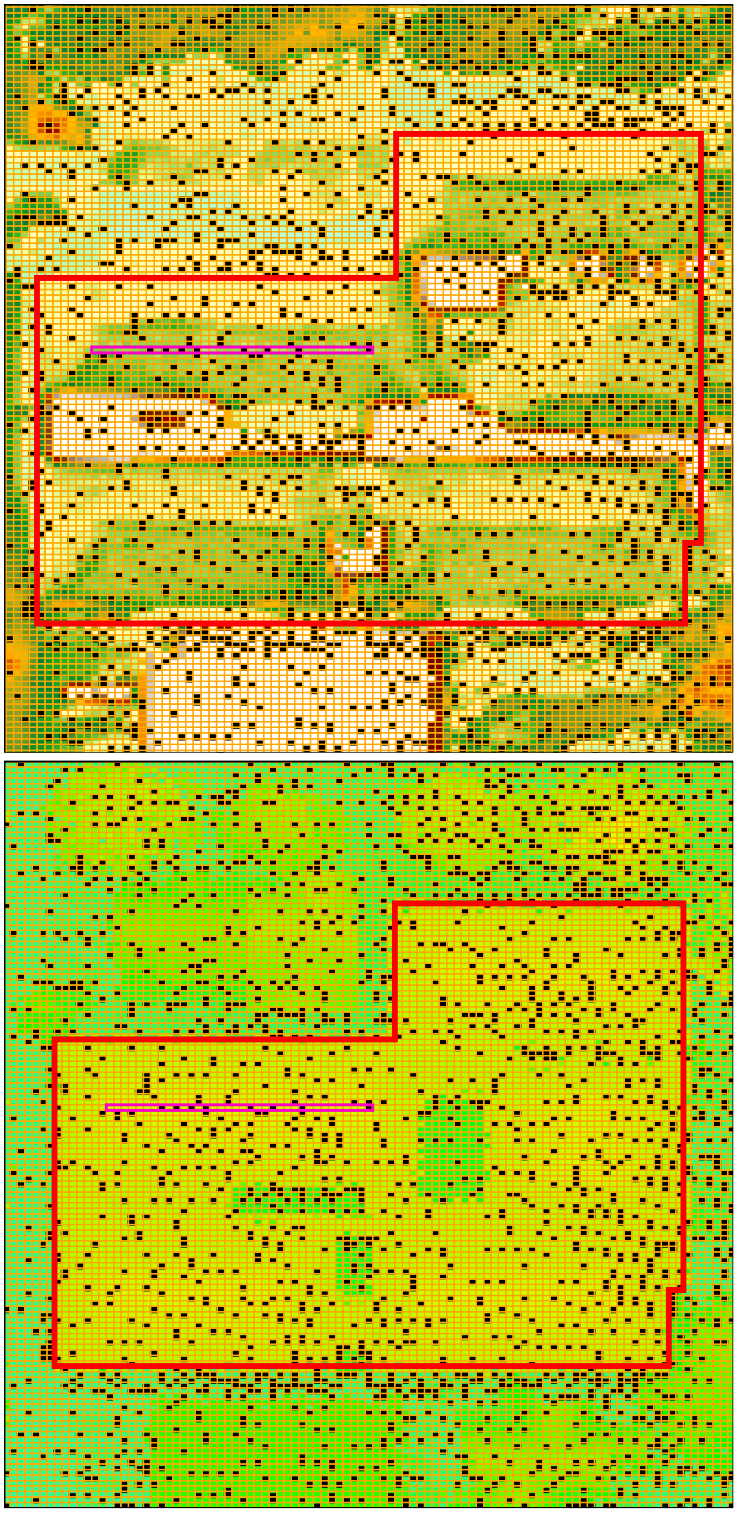

Figure 31: Comparing DEM & Orthoimage (Case C)

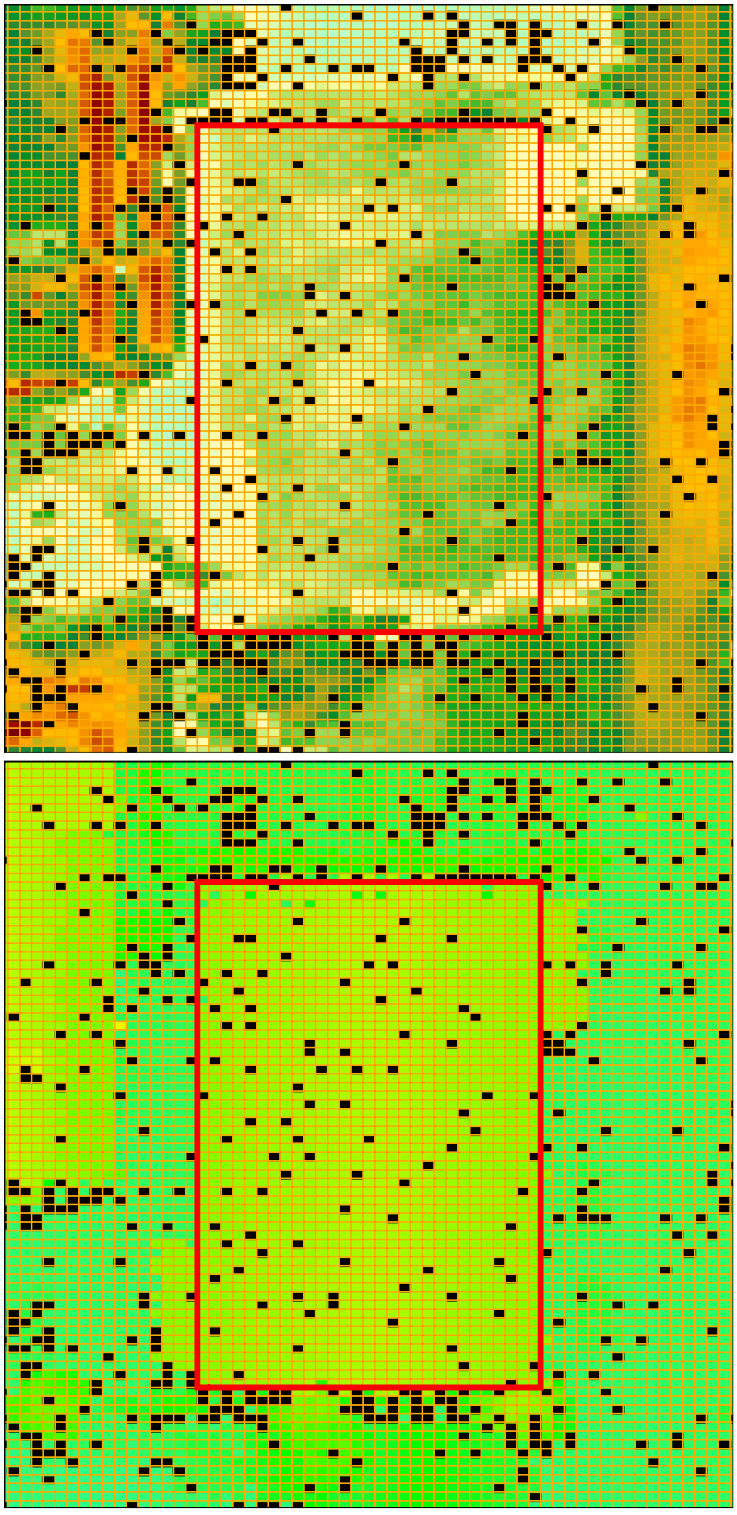

Figure 32: Comparing DEM & Orthoimage (Case D)

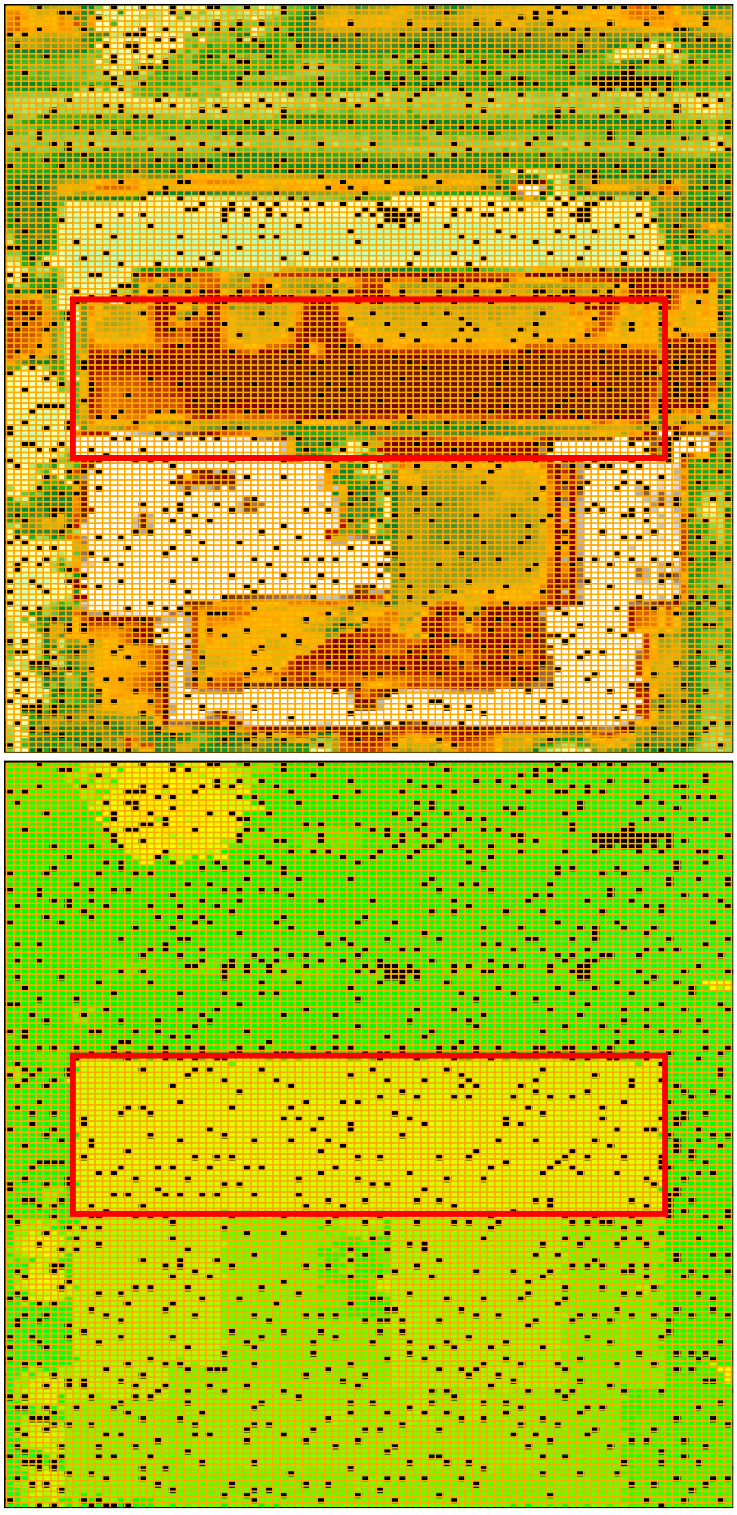

Figure 33: Comparing DEM & Orthoimage (Case E)

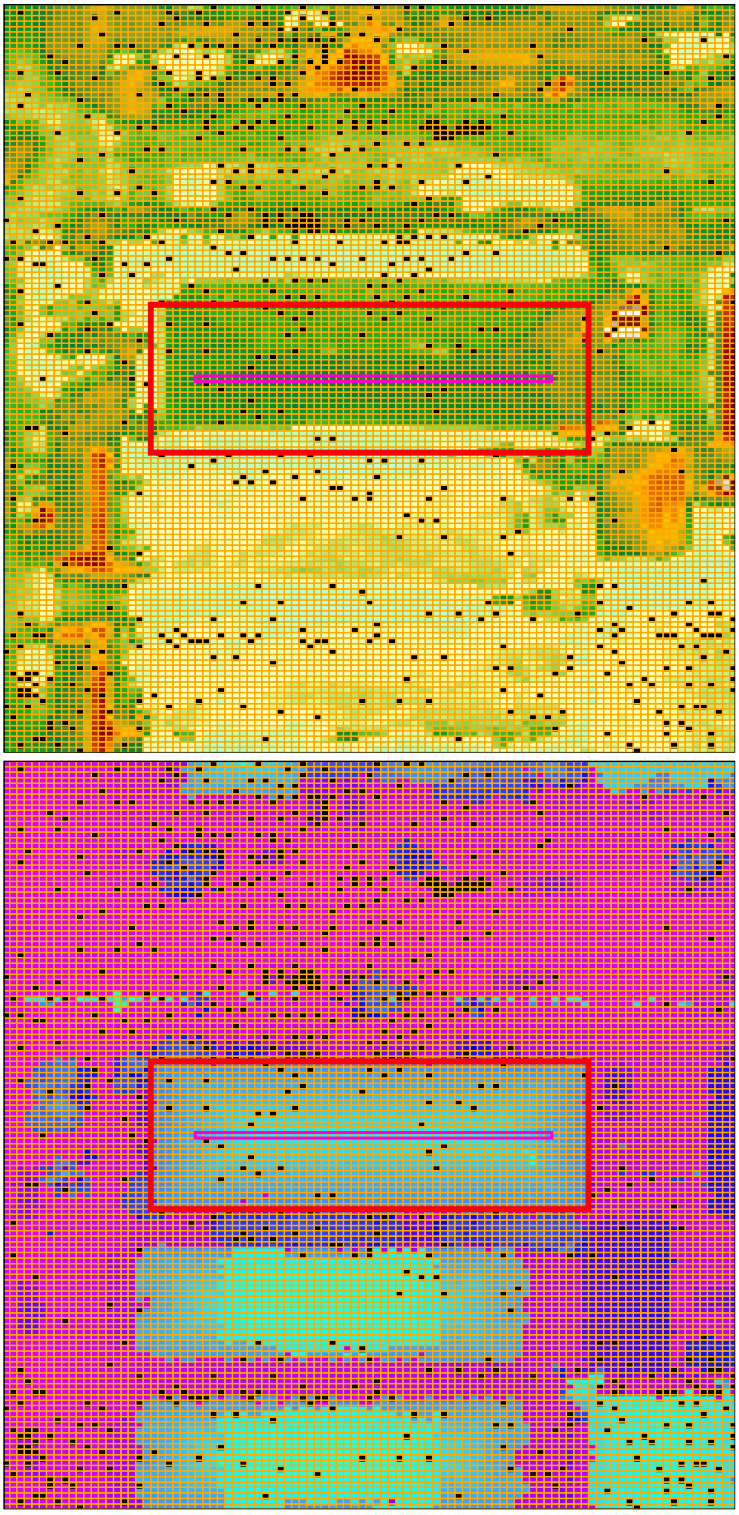

Figure 34: Comparing DEM & Orthoimage (Case F)

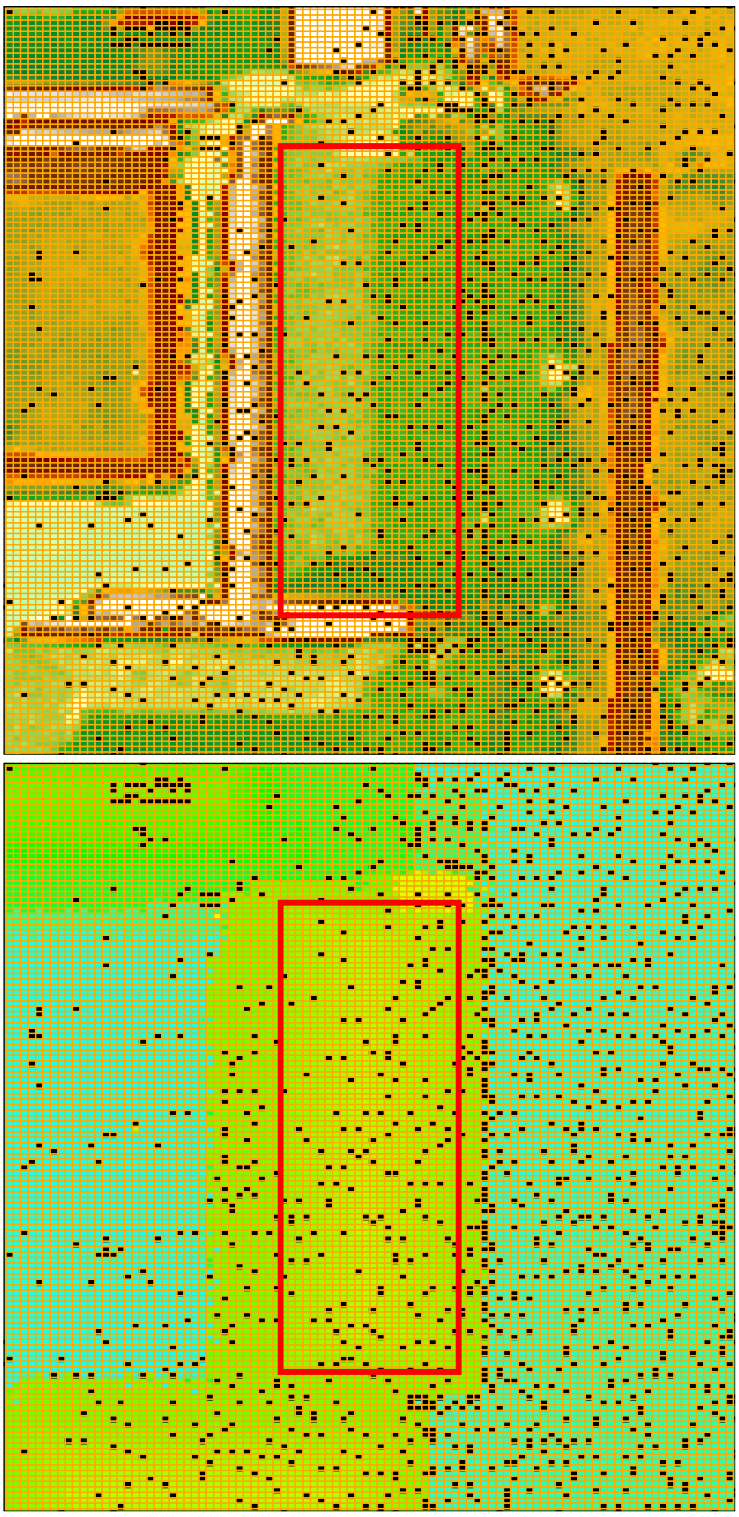

Figure 35: Comparing DEM & Orthoimage (Case G)

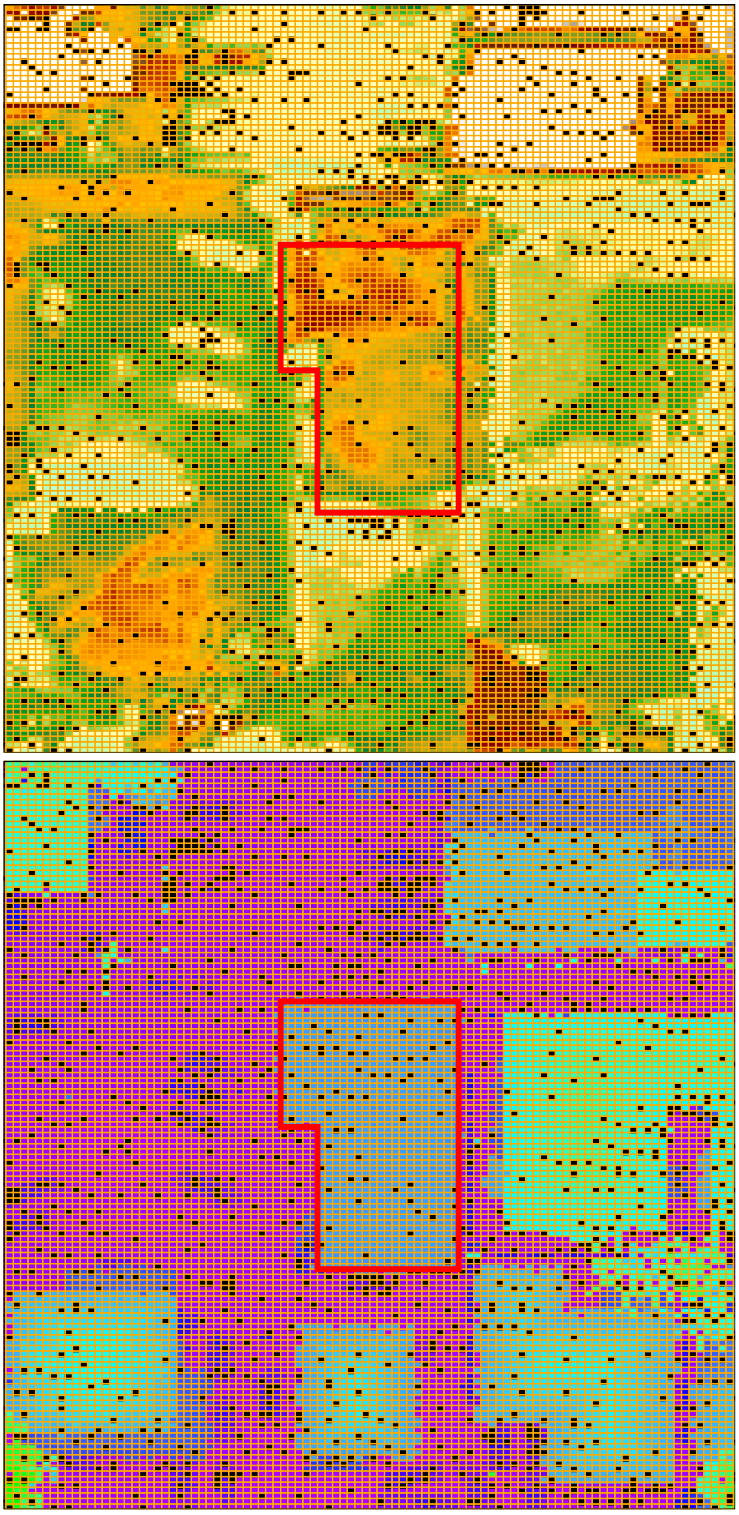

Figure 36: Comparing DEM & Orthoimage (Case H)

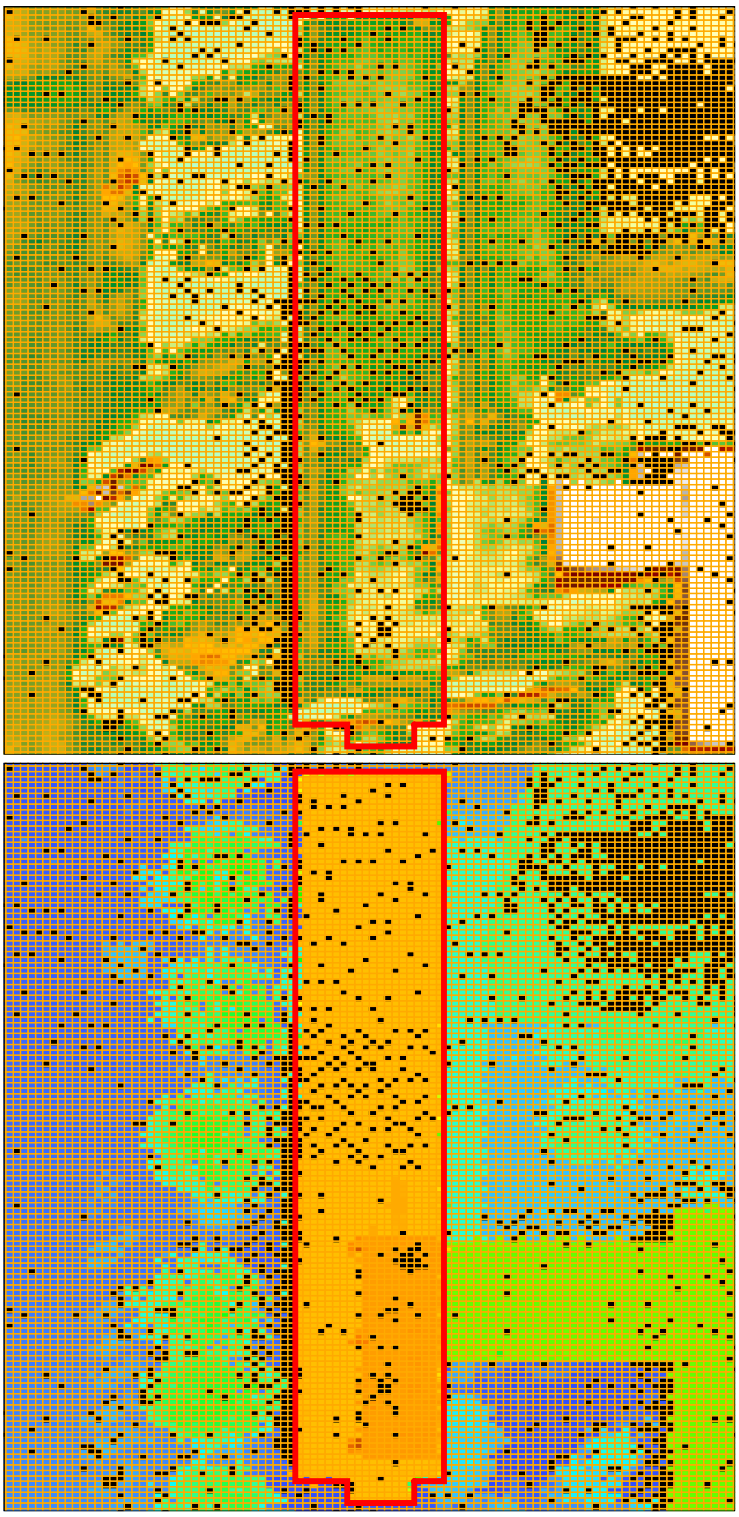

Figure 37: Comparing DEM & Orthoimage (Case I)

Figure 38: Comparing DEM & Orthoimage (Case J)

Figure 39: Comparing DEM & Orthoimage (Case K)

B. Input & Output Parameters

Project the LiDAR data into WGS84 horizontal X-longitude and Y-latitude coordinate system of decimal degrees. Then convert the LiDAR data into a cloud of point shapes, where each point has the attributes allowed by the process to convert the LiDAR into shapes. The following comments give insights into the tools that were used to prepare the LiDAR data for the orthorectification process.

Produce orthoimage from DEM with constant Z value of 103 meters for terrain heights, that is the minimum NAVD88 Z value throughout the study area. This samples the original unrectified (raw) MSI to horizontally shift every pixel in it by a constant amount. But it also forms a DEM raster (grid lattice) with the X-longitude and Y-latitude dimensions that match the input dimensions in units of feet that are converted to decimal degrees by the ERDAS Imagine image processing system. The X & Y spacing of 1.7 feet matches 20.4 inches GSD of the nominal pixel footprint for the original unrectified MSI.

Form a fishnet for the DEM raster that will contain a grid lattice with maximum values of Z for terrain heights after the point cloud is spatially joined to it. This grid lattice is filled the XY points each with a Z value of terrain heights that become the input DEM raster for the orthorectification process.

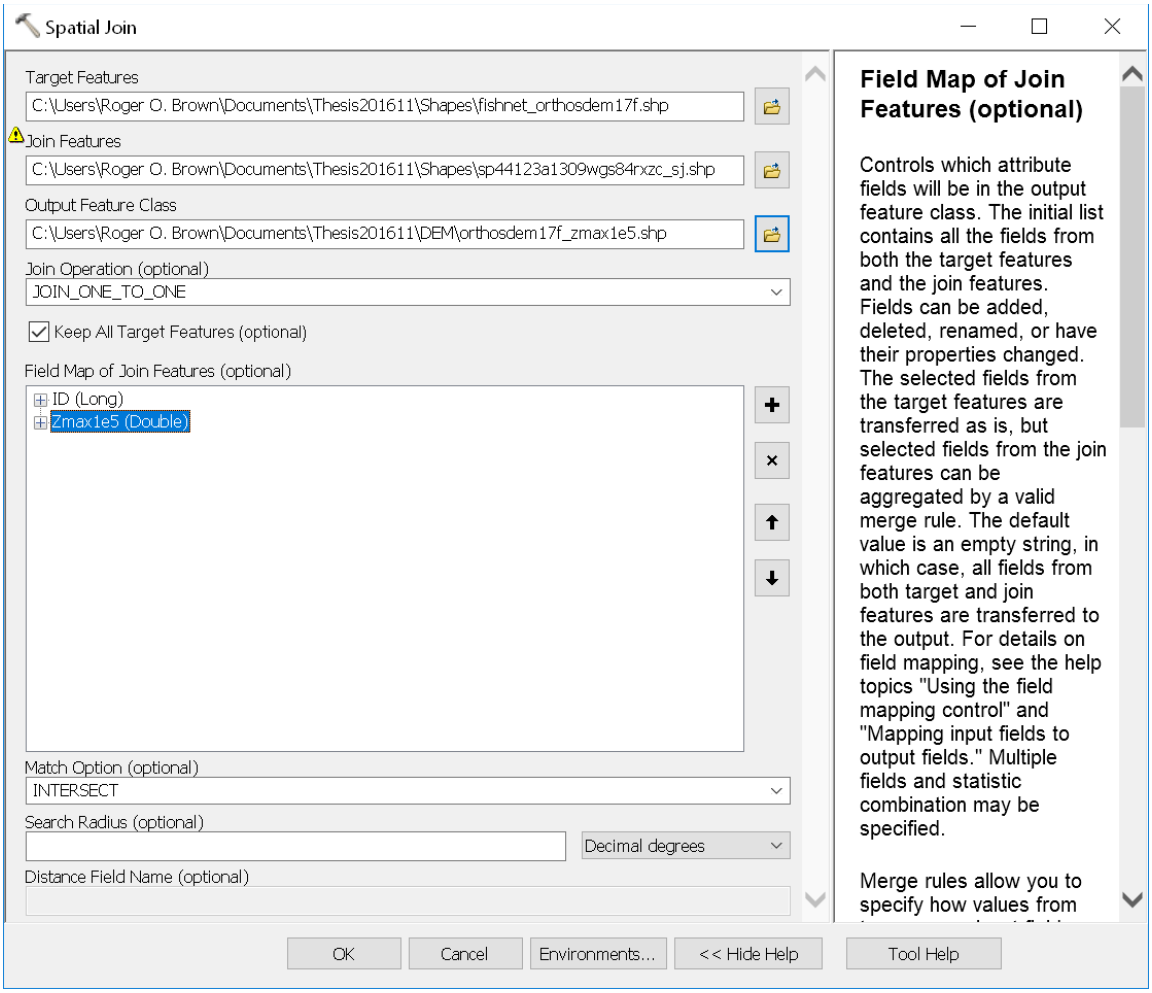

Figure 40: LiDAR Point Cloud Joined With DEM Lattice

Further reduce the grid lattice to points that are the centroids of each produced DEM raster cell.

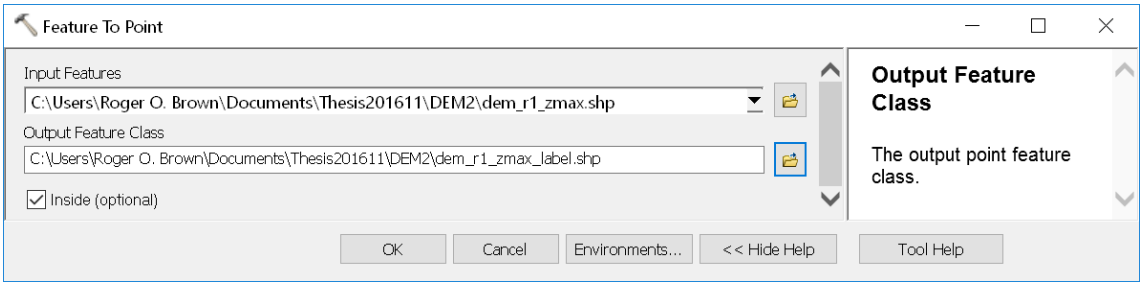

Figure 41:Convert DEM Grid Lattice To Rectangle Centroids

Convert the points from the grid lattice into a DEM raster of terrain height for making the orthoimage. The DEM raster will have the following dimensions, and these will be the same dimensions for the output orthoimage, so there will one elevation value for each for each orthoimage pixel.

ULX: -123.087492999999990

LRX: -123.0749940543250

ULY: 44.0499960

LRY: 44.0374980507163160

Cell Size (X, Y): 6.4828556e-006, 4.6599363e-006

Height: 2683 [Rows]

Width: 1929 [Columns]

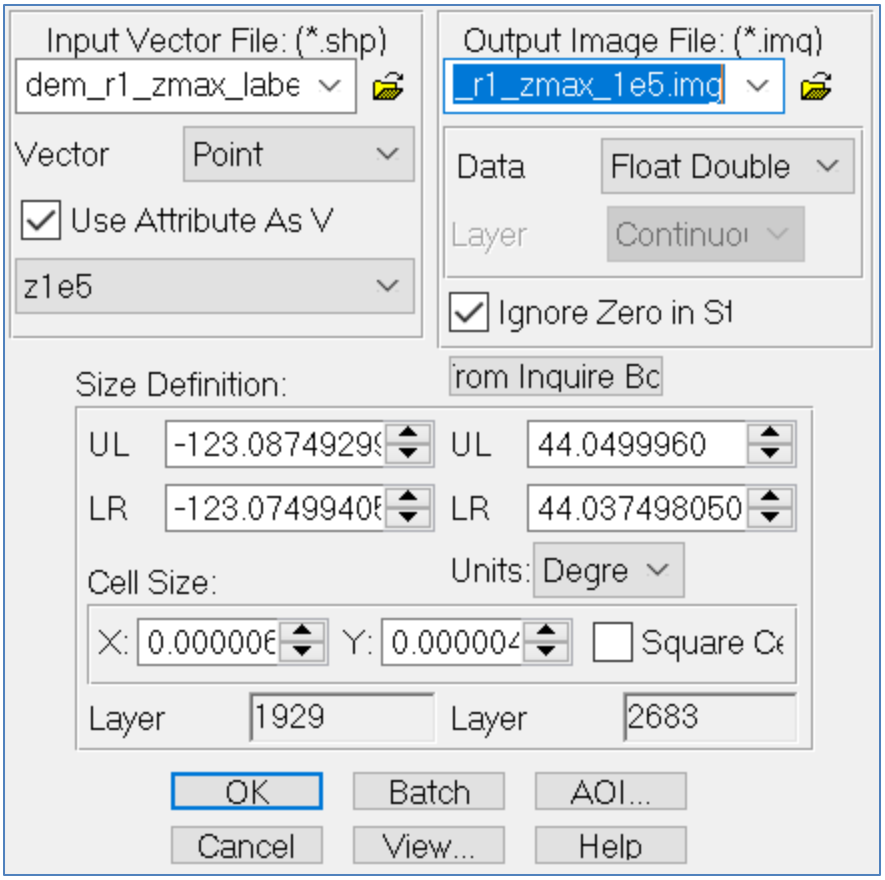

Figure 42: DEM Horizontal Dimensions

Rescale the elevation values to terrain height in meters, because the points-to-raster tool within the image processing system only allowed integer values for both vector and raster data. Do this by dividing the DEM raster of integer Z values by a raster with constant values of 100,000 to get terrain heights in meters.

Recalculate the NAVD88-GRS80 terrain heights within the DEM raster, so that they become WGS84 Z values before the orthorectification process begins. This will change Z value range from 126.41-195.51 meters to 103.09-172.19 meters that entails a reduction of 23.32 meters for every Z value.

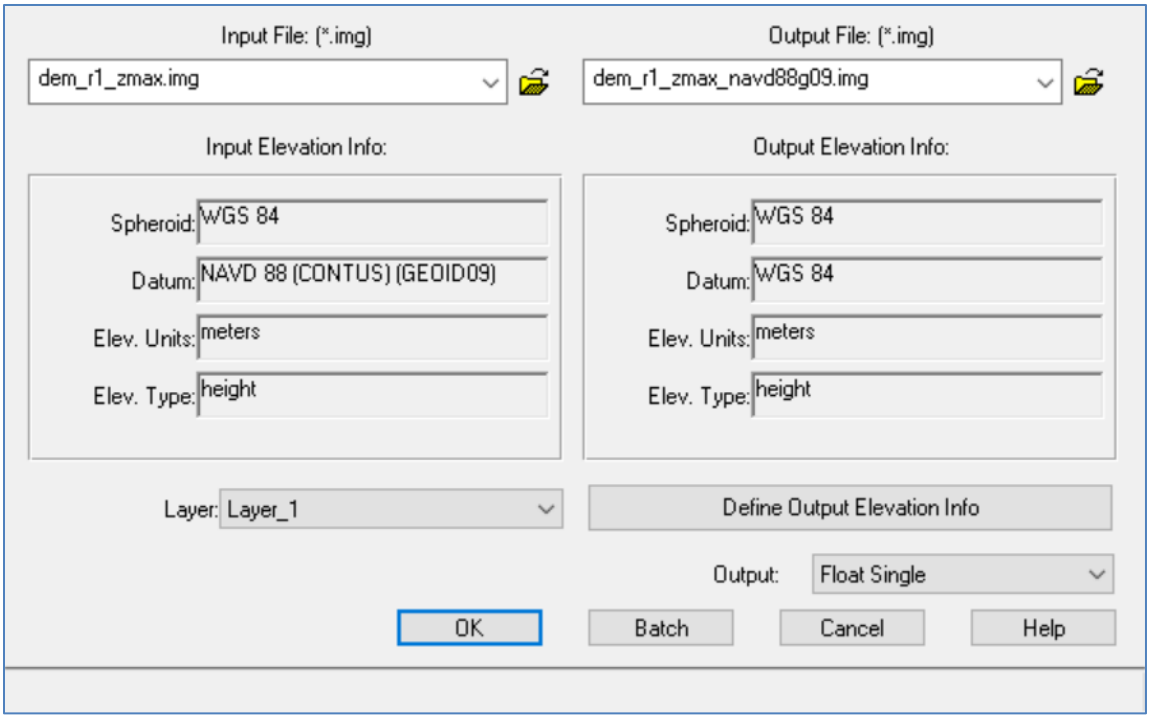

Figure 43: Convert DEM Raster Z Values

Produce the orthophoto using the converted DEM raster with the WGS84 Spheroid (ellipsoid of revolution) and Datum.

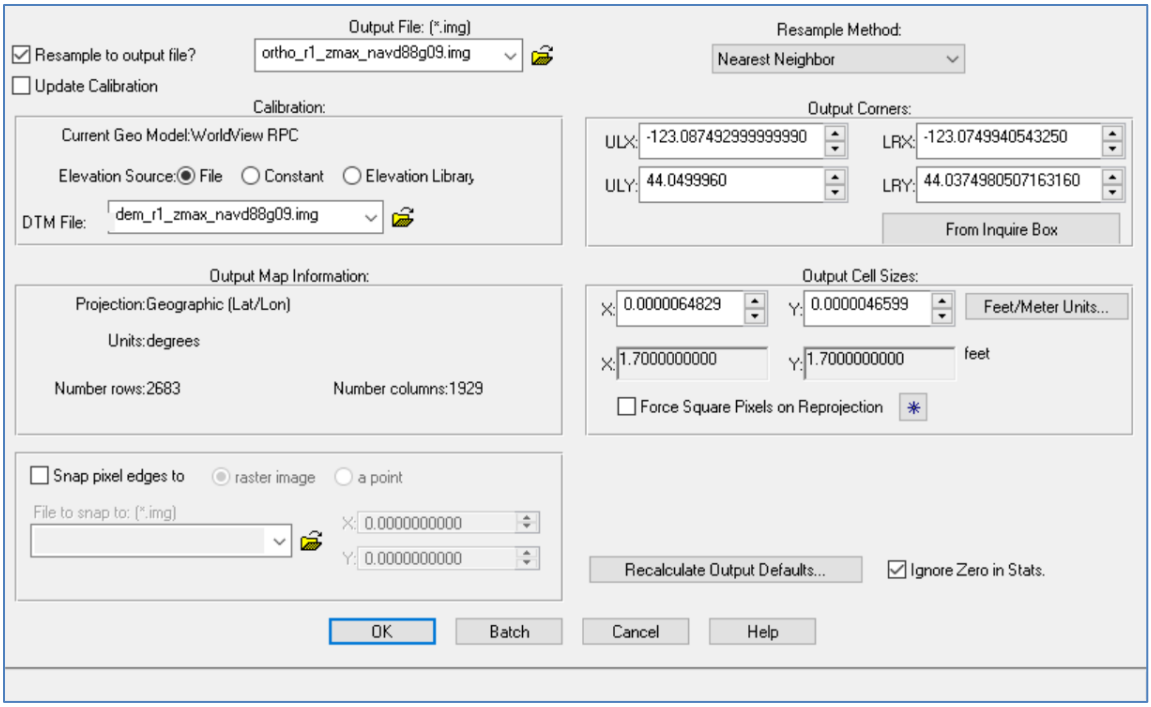

Figure 44: Produce Orthoimage From WGS84 DEM Raster

These previously described steps prepare the gathered OLC LiDAR and WorldView2 MSI for the accuracy assessment of the registration between the DEM and orthoimage respectively.

References

aerometrex, 2011. *Digital Elevaton, Digital Terrain or Digital Surface Model?.* [Online] Available at: <http://www.aerometrex.com.au/blog/?p=89>

Ager, T. P., n.d.. *Geomatics: An Integrated View.* s.l.:National Geospatial-Intelligence Agency (NGA) Innovision.

Agouris, P., Doucette, P. & Stefanidis, A., 2004. Automation and Digital Photogrammetric Workstations. In: J. C. McGlone, E. M. Mikhail, J. Bethel & R. Mullen, eds. *Manual of Photogrammetry.* 5th ed. Bethesda(MD): American Society for Photogrammetry and Remote Sensing (ASPRS), pp. 949-982.

Army Geospatial Center, n.d.. *AGC Imagery Office.* [Online] Available at: <http://www.agc.army.mil/Media/FactSheets/FactSheetArticleView/tabid/11913/Article/480893/agc-imagery-office.aspx>

ASCE, ACSM, ASPRS, 2011. *Glossary of the Mapping Sciences.* Bethesda MD & New York NY: ASCE & ACSM & ASPRS.

Beer, F. P. & Johnston, E. R., 1984. Kinetics of Particles: Newton's Second Law. In: *Vector Mechanics for Engineers: Statics and Dynamics.* s.l.:McGraw Hill Book Comany, pp. 477-520.

Briney, A., 2016. *Geodetic Datums: GPS Utilizes NAD 83 and WGS 84.* [Online] Available at: <http://geography.about.com/od/geographyintern/a/datums.htm>

Brown, R. O., 1995. *Rigorous Imagery Reshaping with Digital Photogrammetric Workstation.* Bethesda MD, ACSM & ASPRS, pp. 465-471.

Brown, R. O., 1998. *Combined Terrain and Spectral Reasoning Methods.* s.l., Environmental Sciences Research Institute (ESRI).

Brown, R. O., 2000. *Method for Rigorous Reshaping of Stereo Imagery with Digital Photogrammetric Workstation.* s.l. Patent No. 6,064,760.

Brown, R. O., 2000. *Spatial Thematic Observation Modeling Process.* s.l., Environmental Sciences Research Institute (ESRI).

Brown, R. O., 2013. *Fusing Terrain Elevations into Sensor Imagery.* Baltimore, American Society for Photogrammetry and Remote Sensing (ASPRS).

Brown, R. O., 2014. *Creating Orthographically Rectified Satellite Multi-Spectral Imagery with High Resolution Digital Elevation Model from LiDAR: A Tutorial,* Washington DC: Department of the Army.

Burtch, R., n.d.. *Lecture Notes for SURE 440 - Advance Photogrammetry.* [Online] Available at: <http://www.koofers.com/files/notes-dbbn9xi0os/> [Accessed December 2013].

Campbell, J. B. & Wynne, R. H., 2011. *Introduction to Remote Sensing.* 5 ed. New York, London: The Guilford Press.

Chen, C.-C., Knoblock, C. A., Shahabi, C. & Thakkar, S., 2003. *Automatically and accurately conflating satellite imagery and maps.* s.l.:s.n.

Cleveland, G. S., 2015. *A Comparative Analysis of Shallow Water Mapping Tools.* Thesis ed. Fairfax VA: George Mason University Library.

Croitoru, A. et al., 2004. Single and stereo based 3d metrology from high-resolution imagery: methodologies and accuracies. *International Archives of Photogrammetry and Remote Sensing,* Volume 20, pp. 1022-1027.

Dale, P., 2005. Plane and Spherical Trigometry. In: *Introduction to Mathematical Techniques Used In GIS.* Boca Raton, London, New York, Washington DC: CRC Press, pp. 43-58.

DigitalGlobe - GeoFUSE Search & Discovery Platform, 2013. [Online] Available at: http://geofuse.geoeye.com/landing/Default.aspx [Accessed December 2013].

DigitalGlobe - ImageFinder, 2013. [Online] Available at: <https://browse.digitalglobe.com/imagefinder/> [Accessed December 2013].

DigitalGlobe, 2013. *DigitalGlobe Launches the DigitalGlobe Foundation to Support Educational Uses of Geospatial Technology.* [Online] Available at: <http://media.digitalglobe.com/press-releases/digitalglobe-launches-the-digitalglobe-foundation-to-support-educational-uses-of-nyse-dgi-1058796>

DigitalGlobe, 2013. *Software Partners.* [Online] Available at: <http://www.digitalglobe.com/partners/software-partners> [Accessed December 2013].

DigitalGlobe, n.d.. *WorldView-2 Imagery Basics and ERDAS Imagine,* s.l.: Intergraph Corporation.

Doyle, D. R., n.d.. *Development of the National Spatial Reference System,* s.l.: National Oceanic and Atmospheric Administration.

Earth Resources Data Analysis System, 2013. *ERDAS Field Guide,* s.l.: Intergraph Corporation.

Ehlers, M., Jacobsen, K. & Schiewe, J., 2009. High Resolution Image Data and GIS. In: M. Madden, ed. *Manual of Geographic Information Systems*.. Bethesda(Maryland): American Society for Photogrammetry and Remote Sensing, pp. 721-778.

Elaksher, A. F., 2009. Using LiDAR-based DEM to orthorectify Ikonos panchromatic images. *Optics and Lasers in Engineering,* Volume 47, pp. 629-635.

English, J., 2010. *Oregon Airborne LiDAR Data Standard,* Portland OR: Oregon Department of Geology and Mineral Industries.

English, J., 2010. *Oregon LiDAR Consortium Specifications & Applications of High Resolution Elevation data in the Pacific Northwest.* [Online] Available at: http://www.oregon.gov/DAS/CIO/GEO/fit/elevation/docs/2010-08-04_dogami_elevation_fit.pdf [Accessed 5 January 2015].

ESRI, 2012. *ArcGIS LiDAR 10.1 Workshop,* Sacramento CA: Environmental Sciences Research Insitute (ESRI).

Forstner, W. & Wrobel, B. P., 2004. Mathematical Concepts in Photogrammetry. In: J. C. McGlone, E. M. Mikhail, J. Bethel & T. Mullen, eds. *Manual of Photogrammetry.* 5th ed. Bethesda(MD): American Society for Photogrammetry and Remote Sensing (ASPRS), pp. 63-234.

Gonzalez, R. C. & Woods, R. E., 2008. Image Segmentation. In: M. McDonald, ed. *Digital Image Processing.* 3 ed. Upper Saddle River NJ: Pearson Preentice Hall.

Graham, L., 2012. The LAS 1.4 Specification. *Photogrammetric Engineering & Remote Sensing (PE&RS),* February, 78(2), pp. 93-102.

Gunay, A., Arefi, H. & Hahn, M., 2007. True Orthophoto Production Using LiDAR Data. *International Archives of Photogrammetry, Remote Sensing and Sptial Information Sciences,* Volume 36.

Heidemann, H. K. et al., 2012. Applications. In: M. S. Renslow, ed. *Manual of Airborne Topographic LiDAR.* Bethesda MD: American Society for Photogrammetry and Remote Sensing, pp. 283-427.

Hobi, M. L. & Ginzler, C., 2012. Accuracy Assessment of Digital Surface Models Based on WorldView-2 and ADS80 Stereo Remote Se. *Sensors,* May, 12(5), pp. 6347-6368.

Homer, C. et al., 2004. Development of a 2001 National Land-Cover Database for the United States. *Photogrammetric Engineering & Remote Sensing (PE&RS),* July, 70(1), pp. 829-840.

Hoshikawa, K. & Umezaki, M., 2014. Effects of terrain-induced shade removal using global DEM data sets on land-cover classification. *International Journal of Remote Sensing,* 35(4), pp. 1331-1355.

Hu, Y., Tao, V. & Croitoru, A., 2004. Understanding the Rational Function Model. *International Archives of Photogrammetry and Remote Sensing,* 20(6), pp. 829-870.

Jacobson, K., 2008. Geometric Modelling of Linear CCDs and Panoramic Imagers. In: *Advances in Photogrammetry, Remote Sensing and Spatial Information Science.* London: Taylor and Francis Group Press, pp. 145-155.

Jensen, J. R., 1995. Issues Involving the Creation of Digital Elevation Models and Terrain Corrected Orthoimagery Using Soft-Copy Photogrammetry. *Geocarto International,* 10(1), pp. 5-21.

LANDinfo Worldwide Mapping LLC, n.d.. *WorldView-2 High-Resolution Satellite Imagery.* [Online]
Available at: <http://www.landinfo.com/WorldView2.htm>
[Accessed December 2013].

Lemoine, E. G. et al., 1998. *EGM96: The NASA GSFC and NIMA Joint Geopotential Model,* Hanover MD: NASA Center for Aerospace Information.

Lewis, D., Edwards, D., Hufnagel, J. & Kim, M., 2010. *Vision inspired spatial engine (VISE): automated object registration for multisource fusion.* s.l., International Society for Optics and Photonics.

Lillesand, T. M., Keifer, R. W. & Chipman, J. W., 2008. *Remote Sensing and Image Inerpretation.* 6 ed. s.l.:John Wiley & Sons, Inc.

Liu, X., Zhang, Z., Peterson, J. & Chandra, S., 2007. LiDAR-derived high quality ground control information and DEM for image orthorectification. *GeoInformatica,* 11(1), pp. 37-53.

Longbotham, N. et al., 2012. Very High Resolution Multiangle Urban Classification Analysis. *IEEE Transactions,* April, 50(4), pp. 1155-1170.

Lu, D. & Weng, Q., 2007. A survey of image classification methods and techniques for improving classification performance. *International Journal of Remote Sensing,* 28(5), pp. 823-870.

Madden, I. & English, J., 2009. *OLC Willamette Valley Delivery 8 Acceptance Report,* s.l.: Oregon Department of Geology and Mineral Industries.

Madin, I. P., 2009. *Oregon: A Geologic History.* [Online] Available at: <http://www.oregongeology.org/pubs/ims/p-ims-028.htm>

Mahalingam, R., Olsen, M. J. & O'Banion, M. S., 2016. Evaluation of landslide susceptibility mapping techniques using lidar-derived conditioning factors (Oregoncase study). *Geomatics, Natural Hazards and Risk,* May.pp. 1-24.

Miller, S., 2013. Photogrammetric Products. In: C. McGlone & G. Y. G. Lee, eds. *Manual of Photogrammetry.* 6th ed. Bethesda(MD): American Society for Photogrammetry and Remote Sensing (ASPRS), pp. 1009-1044.

Moffitt, F. H. & Mikhail, E. M., 1980. Basic Geometry of the Photograph. In: *Photogrammetry.* New York(NY): Harper & Row Publishers Incorporated, pp. 133-148.

Muehrcke, P. C., 1978. Map Use: Reading, Analysis, and Interpretation. In: Madison WI: JP Publications.

Mueller, I. I., 1969. *Spherical and Practical Astronomy: as Applied to Geodesy.* New York: Frederick Ungar Publishing Company.

Mugnier, C. J. et al., 2013. The Mathematics of Photogrammetry. In: C. McGlone & G. Y. G. Lee, eds. *Manual of Photogrammetry.* 6th ed. Bethesda(MD): American Society for Photogrammetry and Remote Sensing (ASPRS), pp. 235-358.

National Geodetic Survey, n.d. *Frequently Asked Questions.* [Online] Available at: <http://www.ngs.noaa.gov/faq.shtml#WhatHARN>

National Imagery and Mapping Agency, November 2011. *The Compendium of Controlled Extensions (CE) for the National Imagery Transmission Format (NITF).* Reston VA: Defense Information Systems Agency.

National Imagery Transmission Format Standard Technical Board, n.d.. *Table of Contents.* [Online]
Available at: <http://www.gwg.nga.mil/ntb/baseline/toc.html>
[Accessed December 2013].

National Oceanic and Atmospheric Administration - NOAA, 2016. *Integrating America's Elevation Data: Vertical Datum Transformation.* [Online]
Available at: <http://www.vdatum.noaa.gov/docs/datums.html>

Nowak Da Costa, J. K. & Walczynska, A., 2011. *Geometric Quality Testing of the WorldView-2 Image Data Acquired over the JRC Maussane Test Site using ERDAS LPS, PCI Geomatics and Keystone digital photogrammetry software packages – Initial Findings,* Luxemborg: Publications Office of the European Union.

Open Source Geospatial Foundation (OSGeo), n.d. *RPCs in GeoTIFF.* [Online]
Available at: <http://geotiff.maptools.org/rpc_prop.html>
[Accessed November 2016].

Oregon Department of Geodesy and Mineral Industries - DOGAMI, n.d.. *LiDAR Collection and Mapping.* [Online]
Available at: <http://www.oregongeology.org/sub/projects/olc/default.htm>
[Accessed December 2015].

Oregon State University Spatial Data Management Group, 2013. [Online]
Available at: <http://sdmg.forestry.oregonstate.edu/lidar-0>
[Accessed December 2013].

Pack, R. T. et al., 2012. An Overview of ALS Technology. In: M. S. Renslaw, ed. *Manual of Airborne Topographic LiDAR.* Bethesda(MD): American Society for Photogrammetry and Remote Sensing, pp. 7-97.

Pearson, F. I., 1984. Conformal Projections. In: *Map Projection Methods.* Blacksburg VA: Sigma Scientific Incorporated, pp. 155-206.

Rice, M. T., 1998. *A Visualization-Based Method for Correcting Relative Positional Error Between Topographic Bases.* Thesis ed. Provo UT: Brigham Young University Library.

Rice, M. T. et al., 2013. *Crowdsourcing to Support Navigation for the Disabled: A report on the motivations, design, creation, and assessment of a testbed environment for accessiblity,* Fairfax VA: George Mason University.

Rice, R. M., Aburizaiza, A. O., Rice, M. T. & Qin, H., 2016. Position Validation in Crowdsourced Accessibility Mapping. *Cartographica: The International Journal for Geographic Information and Geovisualization,* 51(2), pp. 55-66.

Rodgers, R. E., 2015. *A Statistical Comparison of Sidewalk Slopes Derived From Multi-Resolution Digital Elevation Models in Support of Accessibility.* Thesis ed. Fairfax VA: George Mason University Library.

Satellite Imaging Corporation, 2013. *WorldView-2 Satellite Sensor.* [Online] Available at: <http://www.satimagingcorp.com/satellite-sensors/worldview-2.html> [Accessed December 2013].

Scarpace, F., 2013. *Elements in Orthophoto Production.* [Online] Available at: <http://www.asprs.org/Webinar-Series/Webinars-Offered.html>

Stefanidis, A., Georgiadis, C. & Agouris, P., 2006. Orientation of ground-level motion imagery using building facades. *Photogrammetric Engineering & Remote Sensing,* 72(9), pp. 1061-1072.

Tao, C. V. & Hu, Y., 2001. A Comprehensive Study on the Rational Function Model for Photogrammetric Processing. *Photogrammetric Engineering and Remote Sensing,* December, 67(12), pp. 1347-1357.

The University of Texas At San Antonio - UTSA, 2006. *Ellipsoid and Datum, Projection, Coordinate System, and Map Scale.* [Online] Available at: <http://www.utsa.edu/lrsg/Teaching/ES2113/L4_projection.pdf?>

Thorpe, A., 2001. *Digital Orthophotography in New York City.* [Online] Available at: <http://citeseerx.ist.psu.edu/viewdoc/download?doi=10.1.1.119.3235&rep=rep1&type=pdf>

Toth, C. & May, N. C., 2013. *LiDAR Waveform: The Potential and Benefits for Topographic Mapping.* Baltimore, American Society for Photogrammetry and Remote Sensing.

Toutin, T., 2003. Error Tracking in Ikonos Geometric Processing Using a 3D Parametric Model. *Photogrammetric Engineering & Remote Sensing,* 69(1), pp. 43-51.

United States Army Corps of Engineers, July 2002. Photogrammetric Mapping: Engineering and Design. In: *USACE Engineer Manual 1110-1-1000.* Washington DC: Department of the Army.

US Army Infantry School, 2001. *Map Reading and Land Navigation.* Washington DC: Department of the Army.

US Census Bureau - Geography, 2014. *Cartographic Boundary Shapefiles - Urban Areas.* [Online]
Available at: <https://www.census.gov/geo/maps-data/data/cbf/cbf_ua.html>

US Census Bureau - Population Estimates, 2014. *Cities and Towns Totals: Vintage 2013.* [Online]
Available at: <https://www.census.gov/popest/data/cities/totals/2013/index.html>

USGS Land Cover Institute, 2012. *North American Land Cover Data Links.* [Online]
Available at: <http://landcover.usgs.gov/landcoverdata.php>
[Accessed September 2014].

Wang, C., Stefanidis, A. & Agouris, P., 2007. *Relaxation matching for georegistration of aerial and satellite imagery.* s.l., IEEE, pp. 449-451.

Watershed Sciences, 2009. *LiDAR Remote Sensing Data Collection, Willamette Valley Phase I, Oregon,* s.l.: Department of Geology and Mineral Industries.

Worboys, M. & Duckham, M., 2004. *GIS: A Computing Perspective.* 2 ed. Boca Raton, London, New York, Washington DC: CRC Press.

Young, J., 2016. How Is That Done Again? Changing Specifications. *LiDAR Magazine: Evolving Operations*, 27 August, 6(6), pp. 28-32.

Zhou, G., Chen, W., Kelmelis, J. A. & Zhang, D., 2005. A Comprehensive Study on Urban True Orthorectification. September, 43(9), pp. 2138-2147.

Biography

Roger O. Brown was employed by the then called Defense Mapping Agency and now called National Geospatial-Intelligence Agency (NGA) for February 1980 through September 1989 as a Mathematician-Programmer and Cartographer. Where that included research and development plus production experiences with geographic information science, topographic databases, mapping products, remote sensing, digital image processing, and terrain models. These experiences continued during employment by the US Army Corps of Engineers (USACE) Engineer Research and Development Center (ERDC) Geospatial Research Laboratory as a Physical Scientist for September 1980 until retirement in August 2015.

Roger O. Brown continued education as a graduate student throughout a 1980-2015 career, after attaining a 1978 Bachelor of Science degree with a double major in both Mathematics and Economics from the University of Oregon, by attaining a 1989 Master of Science degree with a major in Civil Engineering from Virginia Tech, and then by attaining a 2017 Master of Science degree with a major in Geospatial Intelligence from the George Mason University (GMU). Others should continue efforts to develop better combined spectral and terrain reasoning methods.